SANDIA REPORT
SAND2019-12553; UUR

Printed September 19, 2019

Sandia National Laboratories

Towards Multifluid Multiphysics Continuum Plasma Simulation for Modeling Magnetically-driven Experiments on Z

LDRD Team: J. N. Shadid , M. M. Crockatt, T. M. Smith, S. Conde, R. P. Pawlowski, A. Rappaport, T. A. Gardiner;

Important Collaborators: S. Mabuza, E. G. Phillips, E. Cyr, S. Miller, P. T. Lin, I. Tomas

Prepared by
Sandia National Laboratories
Albuquerque, New Mexico 87185
Livermore, California 94550

Issued by Sandia National Laboratories, operated for the United States Department of Energy by National Technology & Engineering Solutions of Sandia, LLC.

Available to DOE and DOE contractors from

U.S. Department of Energy
Office of Scientific and Technical Information
P.O. Box 62
Oak Ridge, TN 37831

Telephone: (865) 576-8401
Facsimile: (865) 576-5728
E-Mail: reports@osti.gov
Online ordering: http://www.osti.gov/scitech

Available to the public from

U.S. Department of Commerce
National Technical Information Service
5301 Shawnee Road
Alexandria, VA 22312

Telephone: (800) 553-6847
Facsimile: (703) 605-6900
E-Mail: orders@ntis.gov
Online order: https://classic.ntis.gov/help/order-methods

ABSTRACT

Magnetically driven experiments supporting pulsed-power utilize a wide range of configurations, including wire-arrays, gas-puffs, flyer plates, and cylindrical liners. This experimental flexibility is critical to supporting radiation effects, dynamic materials, magneto-inertial-fusion (MIF), and basic high energy density laboratory physics (HEDP) efforts. Ultimately, the rate at which these efforts progress is limited by our understanding of the complex plasma physics of these systems.

Our effort has been to begin to develop an advanced algorithmic structure and a R&D code implementation for a plasma physics simulation capability based on the five-moment multi-fluid / full-Maxwell plasma model. This model can be used for inclusion of multiple fluid species (e.g., electrons, multiple charge state ions, and neutrals) and allows for generalized collisional interactions between species, models for ionization/recombination, magnetized Braginskii collisional transport, dissipative effects, and can be readily extended to incorporate radiation transport physics. In the context of pulsed-power simulations this advanced model will help to allow SNL to computationally simulate the dense continuum regions of the physical load (e.g. liner implosions, flyer plates) as well as partial power-flow losses in the final gap region of the inner MITL. In this report we briefly summarize results of applying a preliminary version of this model in the context of verification type problems, and some initial magnetic implosion relevant prototype problems. The MIF relevant prototype problems include results from fully-implicit / implicit-explicit (IMEX) resistive MHD as well as full multifluid EM plasma formulations.

Acknowledgements

The authors would like to acknowledge the help of Wyatt Hagen, Jesus Bonilla, Richard Kramer, Duncan McGregor, Allen Robinson, Greg Radtke, Matt Bettencourt, Kieth Cartwright, Kris Beckwith, Chris Jennings, Russel Hooper, and Jose Pacheco for helpful discussions on the form of the multifluid plasma model, verification problems, and application prototypes. John Carpenter for help with integrating the UTRI EoS capability and for delivering specific EoS models for our use.

CONTENTS

LIST OF FIGURES

LIST OF TABLES

1. INTRODUCTION

To more accurately model complex plasma dynamics in Z experimental load configurations, advanced multi-fluid multi-physics plasma and electromagnetic simulation capabilities with robust, modern, scalable, and strongly coupled solvers will be required. In general, the dominant solution strategy over the past 20 years has been the use of simple resistive magnetohydrodynamics (MHD) multi-physics models that rely on operator-splitting methods expressed as a sequential evaluation of physics operators in a time-loop.

In the context of plasma models, resistive MHD necessitates significant simplifying assumptions with profound consequences. These include quasi-neutrality, high plasma frequencies, large length-scales compared to the ion inertial length, a collision mediated Ohm's law describing electron dynamics, and the restriction to low-frequency Maxwell equations [see e.g. [23]]. These approximations are invalid over wide regions of the required simulation domain for a typical Z experiment where the plasma flow and EM responses are dynamically altered as the experiment evolves. For this reason user-controlled "knobs" modifying basic physical parameters have been introduced to "patch up" the model response to attempt to overcome fundamental defects in the resistive MHD model. While these "knobs" can be made to recover the approximate limiting physical behavior, they do so in an unphysical manner, and therefore severely impact predictive simulation beyond the parameter space on which the "knobs" have been "tuned". Additionally, current solution strategies often use ad-hoc combinations of operator-splitting, semi-implicit, and explicit time integration to evolve complex multiple-time-scale dynamic solutions. These approaches can often compound the degradation of robustness and predictability of current plasma simulations with numerical stability limits, errors, and time-step controls that are only empirically understood and lead to unstable results when physical mechanisms are strongly-coupled, highly-nonlinear and have overlapping time-scales. For these reasons the approaches described above have not provided the stability, accuracy, scalability, and efficiency required to accurately model plasma physics over the relevant length-scales and dynamic range of time-scales for the physical mechanisms active in Z experiments. In contrast, our overarching, long term, goal is the development of a unique, robust, and accurate implicit/explicit (IMEX) computational physics/mathematical approach for multi-fluid multi-physics shock-hydro plasma research that will help to uniquely position SNL R&D at the forefront of continuum computational analysis of magnetic implosion fusion (MIF).

Our proposed plasma physics model is based on the five-moment multi-fluid / full-Maxwell system outlined in Figure 2-1 [24, 59, 79, 120, 124, 89]. This description can be used for inclusion of multiple fluid species (e.g., electrons, multiple charge state ions, and neutrals) and allows for generalized collisional interactions between species, models for ionization/recombination, magnetized Braginskii collisional transport, dissipative effects, and can be readily extended to incorporate radiation transport physics. In the context of pulsed-power simulations this advanced model will help to allow SNL to computationally simulate the dense continuum regions of the physical load (e.g. liner implosions, flyer plates) as well as partial power-flow losses in the final gap region of the inner MITL. Critical mechanisms that can be studied and characterized include (1) electro-thermal instabilities, (2) incompressible and compressible Hall-modified MRT [see e.g. [121]], (3) current distribution in, and power flow through, low density plasmas outside of the load, and (4) ablation driven plasma formation, evolution, and dynamics of plasma/neutral bridging in the final A-K gap along with electromagnetic wave and force interactions as the load implosion progresses [53]. Understanding these phenomena will allow SNL to study design modifications that help mitigate mechanisms that generate instabilities in load implosions to produce higher implosion compression ratios, more significant magnetic field compressions for MIF, and suggest experimental modifications of loads and the final-gap regions to deliver more power to future Z experiments. In addition, the successful verification, validation and demonstration of predictive modeling of experiments will allow for the proposed multi-fluid plasma model to be used as part of an effective broad-based SNL computational capability for pulsed-power applications.

Finally, with further application of this model the multi-fluid / full-Maxwell formulation could also be used as a reference solution to directly evaluate the validity of a number of assumptions that are used to develop

reduced two-fluid (Hall-physics), generalized Ohm's law (GOL) approximations for inclusion of electron dynamics in MIF. Using high-fidelity multi-fluid reference solutions, would allow us to evaluate individual model assumptions for the GOL approach in detail.

To make this ambitious, robust, and scalable mathematical approach tractable, we have constructed the software implementation on recent unique algorithmic, and plasma-model formulation developments by our team in the Drekar R&D MHD and multi-fluid/EM [116, 105, 89] code as a software-base / algorithmic testbed. This work has been developed with past partial support from the Office of Science (Advanced Scientific Computing Research and Office of Fusion Energy), Sandia LDRD, and ATDM R&D for EMPIRE. The Drekar software base provides an extensible multiphysics capability that can accommodate the description of mass, momentum and energy conservation/balance laws for an arbitrary number of species (charged/neutral) and various forms of approximation for electromagnetic interactions (electro-static, full Maxwell electromagnetic system). This capability has been used to demonstrate the solution to resistive MHD (steady and transient) and multifluid EM plasmas with up to 10 species. At this level the 10 species full multiflluid EM plasma model requires the solution of 56 PDEs at each node in the FE mesh. For these extreme levels of multiphysics computations the ability to robustly and efficiently scale in parallel is required. In this context the Drekar code has been demonstrated to scale to 1M+ cores for MHD, and has run on up to 1.6M cores for elliptic solves that are kernels for the advanced physics-based preconditioners that are critical for the solution of these types of complex systems [116, 115, 73].

The multi-fluid equations are a set of coupled hyperbolic subsystems of equations for modeling the dynamics of partially ionized plasma systems (neutrals, charged ions, and electrons) in the presence of electromagnetic fields. In the brief discussion in this report that describes the stabilization of this system we present a robust and flexible stabilized scheme for the multifluid plasma system. The approach we consider is an algebraic flux corrected (AFC) continuous Galerkin (CG) finite element method [82]. The AFC stabilization, we consider is an iterative local bounds preserving element based formulation [82, 81]. The AFC design, at this time, is based on a blocked stabilization of the hyperbolic system. That is each subsystem (Euler for ions, neutrals, electrons and Maxwell equations) is stabilized separately. Additionally Maxwell equations, employ a divergence cleaning strategy based on an eliminated parabolic divergence cleaning method extended to the maxwell system [35, 78, 122, 81]. The final stabilized semi-discrete method is integrated in time using various time integrators such as IMEX-RK strong stability preserving (SSP) or backward differentiation (BDF) type methods that allow for the stable integration of complex multiple-time-scale systems.

An additional critical and unique aspect of our mathematical approach our continued development, demonstration and evaluation of robust and efficient IMEX temporal discretizations for asymptotic preserving (AP) multi-fluid formulations. Important advantages of IMEX methods include: (1) stability - IMEX methods can be designed with various nonlinear stability properties when coupled with appropriate spatial discretizations (e.g. SSP see e.g., [51, 97, 108]), (2) accuracy - e.g., multistep and multistage type higher-order methods (1st - 5th) are available [51], (3) efficiency - IMEX allows a partition of multi-physics systems into fast/stiff operators, and slower time-scale operators for mixed implicit and explicit evaluation; IMEX also encompasses fully-explicit and fully-implicit methods [51], (4) IMEX has a consistent residual definition that enables higher-level general mathematical approaches for use in sensitivity analysis, UQ, and optimization (e.g., adjoints as in Drekar) [27]. To develop AP IMEX multi-fluid models, we have extended existing multi-fluid capabilities in Drekar to enable transition from highly-resolved spatial/temporal discretizations capturing stiff physical processes to robust under-resolved computations intended to robustly and accurately capture the required asymptotic limits. Specifically to robustly and accurately approximate the strongly hyperbolic character of the multi-fluid equations and to deal with the strong EM source-term coupling we have developed IMEX time-integration approximations that explicitly represent slower fluid phenomena time-scales such as material advection, acoustic waves and shocks, and implicitly represent EM source-terms and couple implicitly to the Maxwell system that generate the fast plasma and cyclotron frequencies. Further, to control time-step limitations for electrons, we have explored fully-implicit models, and IMEX models where the electrons use an implicit representation for advection operators as appropriate.

In the context of MIF, strong magnetic fields are generated and also applied externally to inhibit transport across magnetic field lines. To accurately model strongly anisotropic phenomena, we have developed and begun to evaluate Braginskii transport models [24]. This model is difficult to solve numerically due to extreme levels of differential transport in directions parallel and perpendicular to the B-field, which can differ by 10^4 - 10^5 [24, 121]. Approaches based on high-order DG have shown promise in this context [85]. In our case we have developed an extension of the AFC stabilization for anisotropic transport [64, 63] that allows us to stabilize these operators and eliminate unphysical oscillations.

In the draft report that follows we first consider a brief abstract presentation of multifluid EM plasma model in the context of moments of the underlying Boltzmann system and present the conservation/balance law systems in Section 2. In Section 3 we present a discussion of the general multifluid EM plasma model and describe aspects of the collisional, ionization/recombination interaction models that are employed. In Section 4 we present a description of the general computational formulation that we employ for the multifluid EM plasma model. This includes spatial discretizations, time integration, nonlienar/linear iterative methods, and some representative parallel scaling results for methods on problems of relevance to this effort. Then preliminary verification results are presented for our current effort to develop an implicit/IMEX MHD and multifluid EM plasma capability for exploring computational simulations in support of MIF and pulsed-power applications in Section 5. Results are then presented in Section 6 for the application of these models In the context of MIF relevant systems. Finally we end with conclusions in Section 8.

2. SUMMARY OF THE MULTIFLUID PLASMA MODEL

in this brief summary section we provide a very brief high level view of the multfluid EM plasma model that we are developing, attempt to provide some context for the fluid system as moments of the kinetic model, and then introduce a bit of notation. In Section 3 we provide a more detailed description of the multifluid model, provide reasonable detail on the structure of the model, and provide references.

2.1. Kinetic Model

We consider models for a partially-ionized plasma composed of an arbitrary number of atomic species indexed by $\alpha \in \{1,\ldots,N_A\}$, each of which may be present in one of several charge states $k \in \{0,1,\ldots,z_\alpha\}$. The fluid descriptions that are the focus of this document can be derived by taking various moments (with respect to the velocity variables) of a coupled set of kinetic equations [58, 59, 88, 89]. Each such kinetic equation has the form

$$\partial_t f_s + \mathbf{v}\cdot\nabla_{\mathbf{x}} f_s + \frac{q_s}{m_s}\left(\mathbf{E}+\mathbf{v}\times\mathbf{B}\right)\cdot\nabla_{\mathbf{v}} f_s = \mathcal{C}_s\left[f_s\right] + \mathcal{S}_s, \tag{1}$$

where $f_s = f_s(\mathbf{x},\mathbf{v},t)$ is the one-particle distribution function for species s, $\mathcal{S}_s$ is a source of particles of type s, and s represents one of:

1. e (for the electron species),
2. $(\alpha,0)$ with $\alpha \in \{1,\ldots,N_A\}$ (for neutral species), or
3. (α,k) with $\alpha \in \{1,\ldots,N_A\}$ and $k \in \{1,\ldots,z_\alpha\}$ (for ion species with charge k);

or more simply $s \in \Lambda_{\mathrm{G}}$, where the index set Λ_{G} is defined in Table 2-1. The kinetic equations (1) are coupled through the collision operators $\mathcal{C}_s$, which describe interactions between particles and also through the effect of the electromagnetic fields that are influenced by the flow of charge particles (the current) in Ampere's law of Maxwell's equations. The collisional interactions may occur between particles of the same type or between particles of different types. Collisions of both scattering and reacting types are considered, with reacting interactions covering electron-collision/impact ionization, radiative and dielectronic recombination, and resonant charge exchange events. in our current model the following general assumptions are made:

Model	Reduction	Index Set
General		$\Lambda_{\mathrm{G}} = \{(\alpha,k) : \alpha = 1,\ldots,N_A; k = 0,\ldots,z_\alpha\} \cup \{e\}$
Neutral, Averaged Ion	$\sum_{k=1}^{z_\alpha}$	$\Lambda_{\mathrm{NAI}} = \{(\alpha,0) : \alpha = 1,\ldots,N_A\} \cup \{(\alpha,i) : \alpha = 1,\ldots,N_A\} \cup \{e\}$
Fully Averaged	$\sum_{k=0}^{z_\alpha}$	$\Lambda_{\mathrm{FA}} = \{\alpha : \alpha = 1,\ldots,N_A\} \cup \{e\}$

Table 2-1. Index set of fluid species for each model.

1. It is assumed that resonant charge-exchange interactions occur only between ion and neutral species of the same type; that is, we neglect effects due to charge exchange between two ions and charge exchange between different atomic species.

2. The plasma is assumed to be optically thin, so that modeling the dynamics of the radiation field and and its effects on the plasma (eg., photoionization) may be neglected. That is we will account (eventually) for only radiative emisson.

3. We assume that atoms of different species $\alpha \neq \beta$ engage in only scattering interactions; that is, reacting interactions are restricted to particles of the same atomic species.

For purposes of notation, the collision operators $\mathcal{C}_s$ may be decomposed into a sum of contributions from various interaction types:

$$\mathcal{C}_s = \mathcal{C}_s^{\mathrm{sc}} + \mathcal{C}_s^{\mathrm{ion}} + \mathcal{C}_s^{\mathrm{rec}} + \mathcal{C}_s^{\mathrm{cx}} + \mathcal{C}_s^{\mathrm{rad}}, \tag{2}$$

where each term denotes interactions as follows:

$$\mathcal{C}_s^{\mathrm{sc}} : \text{Elastic scattering interactions,} \tag{3a}$$
$$\mathcal{C}_s^{\mathrm{ion}} : \text{Ionization reactions,} \tag{3b}$$
$$\mathcal{C}_s^{\mathrm{rec}} : \text{Recombination reactions,} \tag{3c}$$
$$\mathcal{C}_s^{\mathrm{cx}} : \text{Charge-exchange reactions,} \tag{3d}$$
$$\mathcal{C}_s^{\mathrm{rad}} : \text{Radiative emission.} \tag{3e}$$

For more thorough discussions concerning the form of the collision operators $\mathcal{C}_s$ see, for example, [86, 87].

2.2. Summary of Fluid Models

Each model is composed of a coupled set of fluid equations of the form

$$\partial_t \rho_s + \nabla \cdot (\rho_s \mathbf{u}_s) = \mathcal{C}_s^{[0]} + \mathcal{S}_s^{[0]}, \tag{4a}$$
$$\partial_t (\rho_s \mathbf{u}_s) + \nabla \cdot (\rho_s \mathbf{u}_s \otimes \mathbf{u}_s + p_s \underline{\mathbf{I}} + \underline{\boldsymbol{\Pi}}_s) = q_s n_s (\mathbf{E} + \mathbf{u}_s \times \mathbf{B}) + \boldsymbol{\mathcal{C}}_s^{[1]} + \boldsymbol{\mathcal{S}}_s^{[1]}, \tag{4b}$$
$$\partial_t \mathcal{E}_s + \nabla \cdot \left[(\mathcal{E}_s + p_s) \mathbf{u}_s + \mathbf{u}_s \cdot \underline{\boldsymbol{\Pi}}_s + \mathbf{h}_s \right] = q_s n_s \mathbf{u}_s \cdot \mathbf{E} + \mathcal{C}_s^{[2]} + \mathcal{S}_s^{[2]}. \tag{4c}$$

Here the governing balance equations for each fluid species s include:

- The mass balance equation for the mass density ρ_s with inclusion of source terms that include ionization/recombination reaction terms ($\mathcal{C}_s^{[0]}$), and a general source ($\mathcal{S}_s^{[0]}$).

- A momentum balance system for the momentum vector $\rho_s \mathbf{u}_s$ with acceleration due to electromagnetic interactions, and source terms that include the rate of momentum production/destruction due to ionization/recombination and interspecies transfer ($\mathcal{C}_s^{[1]}$) effects, along with a general source ($\mathcal{S}_s^{[1]}$),

- n energy balance equation for the total energy (internal + kinetic) $\mathcal{E}_s = \rho_s e_s + \frac{1}{2\rho_s}\|\rho_s \mathbf{u}_s\|^2$ with the work done by the electric field, $\mathbf{E}$, and energy production/destruction due to ionization/recombination and interspecies transfer ($\mathcal{C}_s^{[2]}$) effects, along with a general source ($\mathcal{S}_s^{[2]}$).

This system, in the absence of dissipative/diffusion operators (i.e. the viscous forces, $\underline{\boldsymbol{\Pi}}_s$, and heat conduction, $\mathbf{h}_s$), is an Euler subsystem for each species s with electromagnetic source terms associated with the charged plasma fluid interacting with electric $\mathbf{E}$, and the magnetic $\mathbf{B}$ fields. Here $\rho_s e_s$ is the internal energy which can be related to pressure and temperature by the equation of state (EoS). More detail on the definition of the nomenclature used in these balance equations can be found in Appendix A

The differences between each model that we have developed are enumerated by: (i) differences in the set over which the fluid species index s ranges, and (ii) the forms of the collision terms $\mathcal{C}_s^{[0]}$, $\boldsymbol{\mathcal{C}}_s^{[1]}$, and $\mathcal{C}_s^{[2]}$. An overview of the various models considered is given in Table 2-1. The collision terms for the general multifluid model are obtained by taking moments of the kinetic collision operators $\mathcal{C}_s$. The collision terms for the average ionization and average ion-neutral models are obtained by summing the corresponding collision terms from the general multifluid mode (see Appendix B.2).

2.3. Maxwell's Equations

The electromagnetic fields $\mathbf{E}$ and $\mathbf{B}$ are evolved consistently with the evolution of the species fluid density, ρ_s, and momentum, $\rho_s \mathbf{u}_s$, using Maxwell's equations

$$\frac{1}{c^2}\partial_t \mathbf{E} - \nabla \times \mathbf{B} + \mu_0 \mathbf{J} = \mathbf{0}, \tag{5a}$$

$$\partial_t \mathbf{B} + \nabla \times \mathbf{E} = \mathbf{0}, \tag{5b}$$

$$\nabla \cdot \mathbf{E} = \frac{q}{\epsilon_0}, \tag{5c}$$

$$\nabla \cdot \mathbf{B} = 0, \tag{5d}$$

where the charge and current densities q and $\mathbf{J}$ are defined by

$$q = \sum_s q_s n_s, \tag{6a}$$

$$\mathbf{J} = \sum_s q_s n_s \mathbf{u}_s, \tag{6b}$$

respectively, and the species number densities n_s are computed as $n_s = \rho_s / m_s$.

2.4. Summary of General Multifluid Plasma Model

The most general multifluid electromagnetic plasma model considered in this LDRD project is presented in Table 2-1. This system has a hyperbolic transport/wave physics system sub-structure (Euler-Maxwell) with strong EM, collisional, and ionization/recombination source term coupling, along with the inclusion of 2nd order diffusion type operators (most notably heat transfer).

3. MULTIFLUID EM PLASMA MODEL DESCRIPTION

3.1. General Model Description

We now consider a general multifluid model based on the kinetic equations (1). This model is composed of three groups of equations: the continuity, momentum, and energy equations for each species. The source

Density	$\partial_t \rho_s + \nabla \cdot \left(\rho_s \mathbf{u}_s\right) = -\rho_s n_e \left(I_s + R_s\right) + m_s n_e \left(n_{s-1} I_{s-1} + n_{s+1} R_{s+1}\right)$
Momentum	$\partial_t \left(\rho_s \mathbf{u}_s\right) + \nabla \cdot \left(\rho_s \mathbf{u}_s \otimes \mathbf{u}_s + p_s \underline{\mathbf{I}} + \underline{\mathbf{\Pi}}_s\right) = q_s n_s \left(\mathbf{E} + \mathbf{u}_s \times \mathbf{B}\right) + \sum_{t \neq s} \alpha_{s;t} \rho_s \rho_t \left(\mathbf{u}_t - \mathbf{u}_s\right)$ $-\rho_s \mathbf{u}_s n_e \left(I_s + R_s\right) + \dfrac{m_s}{m_{s-1}} n_e \rho_{s-1} \mathbf{u}_{s-1} I_{s-1} + \left(n_e \rho_{s+1} \mathbf{u}_{s+1} + n_{s+1} \rho_e \mathbf{u}_e\right) R_{s+1}$
Energy	$\partial_t \mathcal{E}_s + \nabla \cdot \left[\left(\mathcal{E}_s + p_s\right) \mathbf{u}_s + \mathbf{u}_s \cdot \underline{\mathbf{\Pi}}_s + \mathbf{h}_s\right] = q_s n_s \mathbf{u}_s \cdot \mathbf{E} + \sum_{t \neq s} \dfrac{\alpha_{s;t} \rho_s \rho_t}{m_s + m_t} \left[A_{s;t} k_\mathrm{B} \left(T_t - T_s\right) + m_t \left(\mathbf{u}_t - \mathbf{u}_s\right)^2\right]$ $-\mathcal{E}_s n_e \left(I_s + R_s\right) + \dfrac{m_s}{m_{s-1}} n_e \mathcal{E}_{s-1} I_{s-1} + \left(n_e \mathcal{E}_{s+1} + n_{s+1} \mathcal{E}_e\right) R_{s+1}$
Charge and Current	$q = \sum_s q_s n_s$ $\qquad$ $\mathbf{J} = \sum_s q_s n_s \mathbf{u}_s$
Maxwell's Equations	$\dfrac{1}{c^2} \partial_t \mathbf{E} - \nabla \times \mathbf{B} + \mu_0 \mathbf{J} = \mathbf{0}$ $\qquad$ $\nabla \cdot \mathbf{E} = \dfrac{q}{\epsilon_0}$ $\partial_t \mathbf{B} + \nabla \times \mathbf{E} = \mathbf{0}$ $\qquad$ $\nabla \cdot \mathbf{B} = 0$

Figure 2-1. General multifluid model for atomic species s with collisional, ionization and recombination terms included.

terms for each equation are written in a general form for either an electron species or an arbitrary atomic species [88, 59, 58, 89]. In order to avoid repetition, only the most general form of each source term is provided for the atomic species. This is done with the understanding that not all ionization and recombination terms will be present for each species; ie., neutral atoms do not recombine and ions of the maximum charge state for a species do not further ionize, though the corresponding source terms are included in the description of the general source terms.

The continuity, momentum, and total energy equations for each species are given by (4), where

$$\mathcal{C}_s^{[0]} \approx m_s \int \mathcal{C}_s \left[f_s\right] d\mathbf{v}, \qquad \boldsymbol{\mathcal{C}}_s^{[1]} \approx m_s \int \mathbf{v} \mathcal{C}_s \left[f_s\right] d\mathbf{v}, \qquad \text{and} \qquad \mathcal{C}_s^{[2]} \approx m_s \int \mathbf{v}^2 \mathcal{C}_s \left[f_s\right] d\mathbf{v} \tag{7a}$$

describe exchange of mass, momentum, and energy due to collisional interactions between species, and

$$\mathcal{S}_s^{[0]} \approx m_s \int \mathcal{S}_s \, d\mathbf{v}, \qquad \boldsymbol{\mathcal{S}}_s^{[1]} \approx m_s \int \mathbf{v} \mathcal{S}_s \, d\mathbf{v}, \qquad \text{and} \qquad \mathcal{S}_s^{[2]} \approx m_s \int \mathbf{v}^2 \mathcal{S}_s \, d\mathbf{v}, \tag{7b}$$

represent external sources.

Exchange of mass. The collision sources $\mathcal{C}_s^{[0]}$ have the form

$$\mathcal{C}_e^{[0]} = m_e \sum_{\substack{(\alpha,k) \in \mathcal{N}_S \\ k \neq z_\alpha}} \Gamma_{(\alpha,k)}^{\mathrm{ion}} - m_e \sum_{\substack{(\alpha,k) \in \mathcal{N}_S \\ k \neq 0}} \Gamma_{(\alpha,k)}^{\mathrm{rec}}, \tag{8a}$$

$$\mathcal{C}_{(\alpha,k)}^{[0]} = m_{(\alpha,k)} \left(\Gamma_{(\alpha,k-1)}^{\mathrm{ion}} - \Gamma_{(\alpha,k)}^{\mathrm{ion}} - \Gamma_{(\alpha,k)}^{\mathrm{rec}} + \Gamma_{(\alpha,k+1)}^{\mathrm{rec}}\right), \qquad (\alpha,k) \in \Lambda_\mathrm{G}, \tag{8b}$$

where

$$\Gamma_s^{\mathrm{ion}} = n_e n_s I_s \qquad \text{and} \qquad \Gamma_s^{\mathrm{rec}} = n_e n_s R_s, \tag{9}$$

and

$$I_s = \langle \sigma_s^{\mathrm{ion}} v_e \rangle \qquad \text{and} \qquad R_s = \langle \sigma_s^{\mathrm{rec}} v_e \rangle \tag{10}$$

are the ionization and recombination rate parameters, respectively.

Exchange of momentum. The collision sources $\mathcal{C}_s^{[1]}$ have the form

$$\mathcal{C}_e^{[1]} = m_e \sum_{\substack{(\alpha,k)\in\mathcal{N}_S \\ k\neq z_\alpha}} \mathbf{u}_{(\alpha,k)}\Gamma^{\text{ion}}_{(\alpha,k)} - m_e\mathbf{u}_e \sum_{\substack{(\alpha,k)\in\mathcal{N}_S \\ k\neq 0}} \Gamma^{\text{rec}}_{(\alpha,k)} + \sum_{(\alpha,k)\in\mathcal{N}_S} \mathbf{R}_{e;(\alpha,k)} \tag{11a}$$

for the electron species, and

$$\begin{aligned}\mathcal{C}^{[1]}_{(\alpha,k)} = {} & m_{(\alpha,k)}\mathbf{u}_{(\alpha,k-1)}\Gamma^{\text{ion}}_{(\alpha,k-1)} - m_{(\alpha,k)}\mathbf{u}_{(\alpha,k)}\left(\Gamma^{\text{ion}}_{(\alpha,k)} + \Gamma^{\text{rec}}_{(\alpha,k)}\right) \\ & + \left(m_{(\alpha,k+1)}\mathbf{u}_{(\alpha,k+1)} + m_e\mathbf{u}_e\right)\Gamma^{\text{rec}}_{(\alpha,k+1)} + \sum_{s\in\Lambda_{\text{G}}^{\smile}(\alpha,k)} \mathbf{R}_{(\alpha,k);s} + \mathcal{C}^{\text{cx},[1]}_{(\alpha,k)}\end{aligned} \tag{11b}$$

for the atomic species, where

$$\mathcal{C}^{\text{cx},[1]}_{(\alpha,k)} = \begin{cases} -\sum_{\ell=1}^{z_\alpha} \mathcal{C}^{\text{cx},[1]}_{(\alpha,\ell)}, & k=0, \\ m_{(\alpha,k)}\left(\mathbf{u}_{(\alpha,0)} - \mathbf{u}_{(\alpha,k)}\right)\Gamma^{\text{cx}}_{(\alpha,k)} + \mathbf{R}^{\text{cx}}_{(\alpha,k);(\alpha,0)} - \mathbf{R}^{\text{cx}}_{(\alpha,0);(\alpha,k)}, & k>0, \end{cases} \tag{11c}$$

and $\Gamma^{\text{cx}}_{(\alpha,k)}$ is the charge exchange rate parameter.

Exchange of energy. Written out term-by-term, the collision sources $\mathcal{C}_s^{[2]}$ have the form[1]

$$\begin{aligned}\mathcal{C}_e^{[2]} = {} & \sum_{\substack{(\alpha,k)\in\mathcal{N}_S \\ k\neq z_\alpha}} \left(\tfrac{1}{2}m_e\mathbf{u}^2_{(\alpha,k)} + m_e e_{(\alpha,k)} - \phi^{\text{ion}}_{(\alpha,k)}\right)\Gamma^{\text{ion}}_{(\alpha,k)} - \left(\tfrac{1}{2}m_e\mathbf{u}_e^2 + m_e e_e\right)\sum_{\substack{(\alpha,k)\in\mathcal{N}_s \\ k\neq 0}} \Gamma^{\text{rec}}_{(\alpha,k)} \\ & + \sum_{(\alpha,k)\in\mathcal{N}_S}\left(\mathbf{u}_e\cdot\mathbf{R}_{e;(\alpha,k)} + Q_{e;(\alpha,k)}\right) + Q_e^{\text{rad}}\end{aligned} \tag{12a}$$

for the electron species, and

$$\begin{aligned}\mathcal{C}^{[2]}_{(\alpha,k)} = {} & \left(\tfrac{1}{2}m_{(\alpha,k)}\mathbf{u}^2_{(\alpha,k-1)} + m_{(\alpha,k)}e_{(\alpha,k-1)}\right)\Gamma^{\text{ion}}_{(\alpha,k-1)} \\ & - \left(\tfrac{1}{2}m_{(\alpha,k)}\mathbf{u}^2_{(\alpha,k)} + m_{(\alpha,k)}e_{(\alpha,k)}\right)\left(\Gamma^{\text{ion}}_{(\alpha,k)} + \Gamma^{\text{rec}}_{(\alpha,k)}\right) \\ & + \left(\tfrac{1}{2}m_{(\alpha,k+1)}\mathbf{u}^2_{(\alpha,k+1)} + m_{(\alpha,k+1)}e_{(\alpha,k+1)} + \tfrac{1}{2}m_e\mathbf{u}_e^2 + m_e e_e + \phi^{\text{ion}}_{(\alpha,k)}\right)\Gamma^{\text{rec}}_{(\alpha,k+1)} \\ & + \sum_{s\in\Lambda_{\text{G}}^{\smile}(\alpha,k)}\left(\mathbf{u}_{(\alpha,k)}\cdot\mathbf{R}_{(\alpha,k);s} + Q_{(\alpha,k);s}\right) + \mathcal{C}^{\text{cx},[2]}_{(\alpha,k)} + Q^{\text{rad}}_{(\alpha,k)}\end{aligned} \tag{12b}$$

for the atomic species, where

$$\mathcal{C}^{\text{cx},[2]}_{(\alpha,k)} = \begin{cases} -\sum_{\ell=1}^{z_\alpha} \mathcal{C}^{\text{cx},[2]}_{(\alpha,k)}, & k=0, \\ \tfrac{1}{2}m_{(\alpha,k)}\left(\mathbf{u}^2_{(\alpha,0)} - \mathbf{u}^2_{(\alpha,k)}\right)\Gamma^{\text{cx}}_{(\alpha,k)} + \mathbf{u}_{(\alpha,0)}\cdot\mathbf{R}^{\text{cx}}_{(\alpha,k);(\alpha,0)} - \mathbf{u}_{(\alpha,k)}\cdot\mathbf{R}^{\text{cx}}_{(\alpha,0);(\alpha,k)} & \\ \quad + Q^{\text{cx}}_{(\alpha,k);(\alpha,0)} - Q^{\text{cx}}_{(\alpha,0);(\alpha,k)}, & k>0. \end{cases} \tag{12c}$$

Here $Q_e^{\text{rad}}, Q^{\text{rad}}_{(\alpha,k)}$ represent sources or losses of energy through radiative processes (eg., bremsstrahlung, line radiation, etc.) and $\phi^{\text{ion}}_{(\alpha,k)}$ denotes the ionization potential[2] for species (α,k).

[1] The forms of the ionization, recombination, and charge exchange sources largely follows that of [86, 87], with the exception of the treatment of the internal energy components. Whereas [86, 87] assumes only an idea gas, our formulation permits a more general form of the expression for internal energy.

[2] Instead of the ground-state ionization potential $\phi^{\text{ion}}_{(\alpha,k)}$, the authors of [87] use an effective ionization potential $\phi^{\text{eff}}_{(\alpha,k)}$ that "approximately includes the electron binding energy plus the excitation energy that is expended (on average) for each ionization

3.1.1. Ionization rate.

The ionization rate parameter $I_{(\alpha,k)}$ specifies the ionization rate of atomic species α from charge state k to $k+1$ by electron-impact ionization. We consider two models for the ionization rate parameters:

(i) Voronov [128] provides coefficients for functional fits of the form

$$I_{(\alpha,k)} = A_{(\alpha,k)} \frac{1 + P_{(\alpha,k)} \sqrt{U_{(\alpha,k)}}}{X_{(\alpha,k)} + U_{(\alpha,k)}} \left(U_{(\alpha,k)}\right)^{K_{(\alpha,k)}} \exp\left(-U_{(\alpha,k)}\right). \tag{13}$$

Here $U_{(\alpha,k)} = \phi^{\text{ion}}_{(\alpha,k)} / T_e$ is the (dimensionless) relative temperature, $\phi^{\text{ion}}_{(\alpha,k)}$ is the ionization energy for species α and charge state k, and $A_{(\alpha,k)}$, $K_{(\alpha,k)}$, $P_{(\alpha,k)}$, and $X_{(\alpha,k)}$ are tabulated fit parameters. The expression (13) is given in units of cm^3s^{-1}. Fit parameters are given in [128] for over 400 cases from H to Ni^{27+} that are (in most cases) accurate to within 10% for temperatures between 1 eV and 20 KeV. For some ions of higher charge states, the fit parameters are computed for temperature ranges up to 100 KeV.

(ii) The following functional approximation from Lotz [76, 77] may also be used:

$$I_{(\alpha,k)} = (2.97\text{E}{-6}) \frac{\xi_{(\alpha,k)}}{\phi^{\text{ion}}_{(\alpha,k)} \sqrt{T_e}} E_1\left(U_{(\alpha,k)}\right), \tag{14}$$

where $\xi_{(\alpha,k)}$ is the number of electrons in the outer shell of the atom being ionized, $U_{(\alpha,k)} = \phi^{\text{ion}}_{(\alpha,k)} / T_e$, and E_1 is the exponential integral of the first kind. The expression (14) is given in units of cm^3s^{-1}, and the leading constant is chosen for $\phi^{\text{ion}}_{(\alpha,k)}$ and T_e both in units of eV. One important advantage of this formula is that as the ionization energy $\phi^{\text{ion}}_{(\alpha,k)}$ approaches zero, the ionization rate $I_{(\alpha,k)}$ monotonically approaches infinity. This ionization model may therefore be combined with models for ionization potential depression to capture effects of pressure ionization phenomena in high-density plasmas. Other ionization models, such as the fits of Voronov, are not well-behaved in this limit.

3.1.2. Recombination rate.

The total recombination rate parameter $R_{(\alpha,k)}$ specifies the recombination rate of atomic species α from charge state k to $k-1$, and is composed of a sum of contributions from radiative recombination (RR) and dielectronic recombination (DR):

$$R_{(\alpha,k)} = R^{\text{rad}}_{(\alpha,k)} + R^{\text{die}}_{(\alpha,k)}. \tag{15}$$

We consider multiple sources of functional fits for each recombination rate parameter. Where data from preferred sources is unavailable, alternative sources are used. It should be noted that dielectronic recombination rates can be suppressed by sufficiently high electron densities [93, 94], though we have not included such effects here.

We leverage the following sources of data for radiative recombination, in order of preference:

event," and additionally includes contributions from the dissociation of diatomic gases. We have excluded these additional contributions since (i) they are highly uncertain and serve as only very rough approximations of reality, and (ii) these contributions would not apply in many of our applications of interest. Additionally, we note that in [87] the corresponding energy gain in the recombination term was excluded, since this energy is typically radiated away as part of the radiative recombination process. Here the terms Q^{rad}_e and $Q^{\text{rad}}_{(\alpha,k)}$ are used to account for all radiative losses (including those due to radiative recombination) and therefore the ionization energy is included in the recombination energy balance (though it should be removed in the radiative loss terms).

(i) Badnell [11] provides coefficients for fits based on the functional form of Verner and Ferland [127], which can be written as

$$R^{\text{rad}}_{(\alpha,k)} = A_{(\alpha,k)} \left[\sqrt{T_e / T_0^{(\alpha,k)}} \left(1 + \sqrt{T_e / T_0^{(\alpha,k)}} \right)^{1-D_{(\alpha,k)}} \left(1 + \sqrt{T_e / T_1^{(\alpha,k)}} \right)^{1+D_{(\alpha,k)}} \right]^{-1}, \tag{16a}$$

where

$$D_{(\alpha,k)} = B_{(\alpha,k)} + C_{(\alpha,k)} \exp\left(-T_2^{(\alpha,k)} / T_e \right) \tag{16b}$$

is the modified exponential coefficient introduced by Gu [45], and $A_{(\alpha,k)}$, $B_{(\alpha,k)}$, $C_{(\alpha,k)}$, and $T_i^{(\alpha,k)}$ for $i = 0, 1, 2$ are tabulated fit parameters. Except for some low-charge ions, it is usually the case that $C_{(\alpha,k)} = T_2^{(\alpha,k)} = 0$, in which case $D_{(\alpha,k)} = B_{(\alpha,k)}$. The expression (16) is given in units of cm^3s^{-1}, and coefficients are provided for electron temperatures in units of eV or K. Fits are provided for all elements up to Zn (inclusive), plus Kr, Mo, and Xe, for all isoelectronic sequences up to Na-like forming Mg-like. The fits are claimed to be accurate for electron temperatures between (1.0E+1) k^2 and (1.0E+7) k^2 degrees Kelvin to within 1% for multiply charged ions and 5% for singly and doubly ionized states. Further, the fit formula is designed to produce the correct asymptotic forms outside of these temperature ranges in both the low- and high-temperature limits.

(ii) Kotelnikov, et al. [56] supplies the following approximate analytic formula based on a hydrogenic approximation:

$$R^{\text{rad}}_{(\alpha,k)} = \frac{8.414 k \alpha^4 c a_0^2 \left[\ln(1+\lambda) + 3.499 \right]}{(1/\lambda)^{1/2} + 0.6517 (1/\lambda) + 0.2138 (1/\lambda)^{3/2}}, \tag{17a}$$

where α is the fine-structure constant, a_0 is the Bohr radius, c is the speed of light in vacuum, and

$$\lambda = \frac{h R_\infty c k^2}{k_\text{B} T_e}, \tag{17b}$$

with h, k_B, and R_∞ representing the Planck, Boltzmann, and Rydberg constants, respectively. When using standard SI units for all supplementary constants, the expression (17a) yields rates in units of m^3s^{-1}. The accuracy of this formula is expected to be within 3% for $1.0\text{E}{-4} < \lambda < 1.0\text{E}{+4}$. In the low- and high-temperature limits, this formula yields rates $R^{\text{rad}}_{(\alpha,k)} \propto T_e^{-1/2}$ and $R^{\text{rad}}_{(\alpha,k)} \propto T_e^{-3/2}$, respectively, so that reasonable (if not necessarily accurate) rates are obtained outside of the targeted temperature range.

We leverage the following sources of data for dielectronic recombination, in order of preference:

(i) In a sequence of papers, [1, 2, 3, 4, 5, 10, 12, 16, 29, 30, 31, 55, 90, 130, 131, 132, 133] Badnell, et al. provide coefficients for fits of the form

$$R^{\text{die}}_{(\alpha,k)} = T_e^{-3/2} \sum_{i=1}^{N_{(\alpha,k)}} c_i^{(\alpha,k)} \exp\left(-E_i^{(\alpha,k)} / T_e \right), \tag{18}$$

where $c_i^{(\alpha,k)}$, $E_i^{(\alpha,k)}$, and $N_{(\alpha,k)}$ are tabulated fit parameters. The expression (18) is given in units of cm^3s^{-1}, and the electron temperature is expected in units of degrees Kelvin. These fits are claimed to reproduce the computed data on which they are based to within 5% in general, and in most cases to within 1%.

(ii) Landini, et al. [66, 67] provide coefficients for fits of the form

$$R^{\text{die}}_{(\alpha,k)} = A_{(\alpha,k)} T_e^{-3/2} \exp\left(-T_0^{(\alpha,k)} / T_e \right) \left(1 + B_{(\alpha,k)} \exp\left(-T_1^{(\alpha,k)} / T_e \right) \right), \tag{19}$$

where $A_{(\alpha,k)}$, $B_{(\alpha,k)}$, $T_0^{(\alpha,k)}$, and $T_1^{(\alpha,k)}$ are tabulated fit parameters. The expression (19) is given in units of cm^3s^{-1}, and the electron temperature is expected in units of degrees Kelvin. While believed to be generally less accurate than the formula (18), the fits of Landini, et al. can be used as a substitute for data not provided by Badnell, et al. for lower ionization states of some heavier atomic species – in particular, S, Cl, Ar, K, Ca, Ti, Cr, Mn, Fe, Co, and Ni.

3.1.3. Momentum transfer due to elastic collisions.

The momentum transfer from species s to species t due to elastic, non-reacting collisions is specified by $\mathbf{R}_{s;t}$, defined as [83, 84]

$$\mathbf{R}_{s;t} = \alpha_{s;t}\rho_s\rho_t\left(\mathbf{u}_t - \mathbf{u}_s\right)\Phi_{s;t}, \tag{20}$$

where $\alpha_{s;t}$ is the friction coefficient, and $\Phi_{s;t}$ is a correction factor that depends on the drift speed $|\mathbf{u}_s - \mathbf{u}_t|$ and the reduced thermal speed

$$V_{\text{therm}} = \sqrt{\frac{2k_{\text{B}}\left(m_t T_s + m_s T_t\right)}{m_s m_t}}. \tag{21}$$

It is found that $\Phi_{s;t} = 1$ in the limit of vanishing drift speed, and this value is generally sufficient when the drift speed is much smaller than the thermal speed. Expressions for more general scenarios can be found in [114].

The friction coefficient is composed of different expressions depending on whether the interaction involves one or more neutral species [84]. For two interacting charged species, the friction coefficient is given by

$$\alpha_{s;t} \overset{\text{def}}{=} \frac{Z_s^2 Z_t^2 |q_e|^4 \ln\Lambda_{s;t}}{6\pi\sqrt{2\pi}\epsilon_0^2 m_s m_t m_{s;t}\left(k_{\text{B}}T_s/m_s + k_{\text{B}}T_t/m_t\right)^{3/2}}, \tag{22}$$

where

$$m_{s;t} \overset{\text{def}}{=} \frac{m_s m_t}{m_s + m_t} \tag{23}$$

is the reduced mass and

$$\ln\Lambda_{s;t} \overset{\text{def}}{=} \ln\left[\frac{12\pi\left(\epsilon_0 k_{\text{B}}\right)^{3/2}\left(T_s + T_t\right)}{|Z_s Z_t||q_e|^3}\left(\frac{T_s T_t}{Z_s^2 n_s T_t + Z_t^2 n_t T_s}\right)^{1/2}\right] \tag{24}$$

is Coulomb's logarithm. For interactions that involve one or more neutral species, the friction coefficient is given by

$$\alpha_{s;t} \overset{\text{def}}{=} \frac{1}{m_s + m_t}\frac{4}{3}\left[\frac{8}{\pi}\left(\frac{k_{\text{B}}T_s}{m_s} + \frac{k_{\text{B}}T_t}{m_t}\right)\right]^{1/2}\sigma_{s;t}, \tag{25}$$

where $\sigma_{s;t}$ is the collisional cross section.

Values for some collisional cross sections $\sigma_{s;t}$ between species up to He are included in [84]. These values are summarized in Table 3-1. For heavier species, we compute cross section values using a simple hard-sphere approximation, where

$$\sigma_{s;t} = \pi\left(r_s + r_t\right)^2 \tag{26}$$

with r_s and r_t the radii of species s and t, respectively. Cross section values computed using atomic radii from [28] are summarized in Table 3-2.

3.1.4. Momentum transfer due to charge exchange.

The following approximation for $\Gamma^{\text{cx}}_{(\alpha,k)}$ is given in [100]:

$$\Gamma^{\text{cx}}_{(\alpha,k)} = \sigma^{\text{cx}}_{(\alpha,k)}\left(U^{\text{cx}}_{(\alpha,k)}\right) n_{(\alpha,k)} n_{(\alpha,0)} U^{\text{cx}}_{(\alpha,k)}, \tag{27}$$

where

$$U^{\text{cx}}_{(\alpha,k)} = \left(\frac{4}{\pi}u^2_{T_{(\alpha,k)}} + \frac{4}{\pi}u^2_{T_{(\alpha,0)}} + u^2_{(\alpha,k);(\alpha,0)}\right)^{1/2}, \tag{28}$$

Species	Value (m^2)	Model
H^+–H	1.0E−18	Quant. mech. calc. [129]
H^+–He	1.0E−19	Quant. mech. calc. [129]
H–e	1.5E−19	Quant. mech. calc. [129]
He–e	5.0E−20	Quant. mech. calc. [129]
H–He	1.5E−19	[69]
H–He^+	2.0E−20	Hard sphere [84]
H–He^{2+}	1.0E−20	Hard sphere [84]
He–He^+	5.0E−19	Quant. mech. calc. [39]
He–He^{2+}	3.0E−21	Hard sphere [84]

Table 3-1. Elastic scattering cross sections for some interactions involving neutral species.

with

$$u_{s;t}^2 = \left\|\mathbf{u}_{s;t}\right\|^2, \qquad \mathbf{u}_{s;t} = \mathbf{u}_s - \mathbf{u}_t, \qquad u_{T_s}^2 = \frac{2k_\mathrm{B}T_s}{m_s}, \tag{29}$$

and σ_s^{cx} denotes the charge exchange cross section for species s. The author of [87] has observed this approximation to be accurate to within a few percent.

The momentum transfer between an ion species $i = (\alpha, k)$ and a neutral species $n = (\alpha, 0)$ due to charge exchange interactions is specified by $\mathbf{R}_{i;n}^{\mathrm{cx}}$ and $\mathbf{R}_{n;i}^{\mathrm{cx}}$, which are defined as [100]

$$\mathbf{R}_{i;n}^{\mathrm{cx}} = \sigma_i^{\mathrm{cx}}\left(U_i^{\mathrm{cx}}\right) n_n \rho_i \left(\mathbf{u}_n - \mathbf{u}_i\right) u_{T_n}^2 \left[4\left(\frac{4}{\pi}u_{T_i}^2 + u_{i;n}^2\right) + \frac{9\pi}{4}u_{T_n}^2\right]^{-1/2}, \tag{30a}$$

$$\mathbf{R}_{n;i}^{\mathrm{cx}} = \sigma_i^{\mathrm{cx}}\left(U_i^{\mathrm{cx}}\right) n_n \rho_i \left(\mathbf{u}_i - \mathbf{u}_n\right) u_{T_i}^2 \left[4\left(\frac{4}{\pi}u_{T_n}^2 + u_{i;n}^2\right) + \frac{9\pi}{4}u_{T_i}^2\right]^{-1/2}. \tag{30b}$$

A common approach to constructing approximate values for the charge exchange cross sections σ_i^{cx} is a fit of the form

$$\sigma_i^{\mathrm{cx}}(v) = \left(A + C\log_b v\right)^2, \tag{31}$$

where A, C, and b are constants. In [100] a fit formula from [42] for charge exchange between H and H^+ is used that is characterized by

$$A = 2.1\mathrm{E}{-7}, \qquad C = -9.2\mathrm{E}{-9}, \qquad \text{and} \qquad b = e, \tag{32}$$

with units of cm^2. Based on data from [15], the author of [87] proposes the following fits:

$$\mathrm{H}{-}\mathrm{H}^+: \qquad A = 1.12\mathrm{E}{-18}, \qquad C = -7.15\mathrm{E}{-20}, \qquad b = e, \tag{33a}$$

$$\mathrm{D}{-}\mathrm{D}^+: \qquad A = 1.09\mathrm{E}{-18}, \qquad C = -7.15\mathrm{E}{-20}, \qquad b = e, \tag{33b}$$

	Radius (m)	Elastic scattering cross section (m^2)						
		H	He	Be	Ne	Al	Ar	e^-
H	5.30E−11	3.53E−20	2.22E−20	8.55E−20	2.60E−20	9.19E−20	4.83E−20	8.82E−21
He	3.10E−11	2.22E−20	1.21E−20	6.42E−20	1.50E−20	6.97E−20	3.27E−20	3.02E−21
Be	1.12E−10	8.55E−20	6.42E−20	1.58E−19	7.07E−20	1.66E−19	1.05E−19	3.94E−20
Ne	3.80E−11	2.60E−20	1.50E−20	7.07E−20	1.81E−20	7.65E−20	3.73E−20	4.54E−21
Al	1.18E−10	9.19E−20	6.97E−20	1.66E−19	7.65E−20	1.75E−19	1.12E−19	4.37E−20
Ar	7.10E−11	4.83E−20	3.27E−20	1.05E−19	3.73E−20	1.12E−19	6.33E−20	1.58E−20

Table 3-2. Atomic radii and elastic scattering cross sections computed using a hard-sphere approximation.

with units of m^2.

3.1.5. Heat transfer due to elastic collisions.

The heat transfer from species s to species t due to elastic, non-reacting collisions is specified by $Q_{s;t}$, defined as [84]

$$Q_{s;t} = \frac{\alpha_{s;t}\rho_s\rho_t}{m_s+m_t}\Big[A_{s;t}k_{\mathrm{B}}(T_t-T_s)\Psi_{s;t} + m_t(\mathbf{u}_t-\mathbf{u}_s)^2\Phi_{s;t}\Big], \tag{34}$$

where $\alpha_{s;t}$ is the friction coefficient given by either (22) or (25), and $\Psi_{s;t}$ and $\Phi_{s;t}$ are correction factors that depend on the drift and reduced thermal speeds. The parameter $A_{s;t}$ takes the value 4 for electron-neutral interactions, and 3 for all other types of interactions. The correction factors $\Psi_{s;t}$ and $\Phi_{s;t}$ take the value 1 in the limit of vanishing drift speed, and this value is generally sufficient when the drift speed is much smaller than the thermal speed. Expressions for more general scenarios can be found in [114].

3.1.6. Thermal energy transfer due to charge exchange.

The transfer of thermal energy between an ion species $i=(\alpha,k)$ and a neutral species $n=(\alpha,0)$ due to charge exchange interactions is specified by $Q^{\mathrm{cx}}_{i;n}$ and $Q^{\mathrm{cx}}_{n;i}$. The following approximations from [100] are used:

$$Q^{\mathrm{cx}}_{i;n} = \sigma^{\mathrm{cx}}_i\left(U^{\mathrm{cx}}_i\right)n_n\rho_i\frac{3}{4}u^2_{T_n}\left(\frac{4}{\pi}u^2_{T_i}+u^2_{i;n}+\frac{64}{9\pi}u^2_{T_n}\right)^{1/2}, \tag{35a}$$

$$Q^{\mathrm{cx}}_{n;i} = \sigma^{\mathrm{cx}}_i\left(U^{\mathrm{cx}}_i\right)n_n\rho_i\frac{3}{4}u^2_{T_i}\left(\frac{4}{\pi}u^2_{T_n}+u^2_{i;n}+\frac{64}{9\pi}u^2_{T_i}\right)^{1/2}. \tag{35b}$$

3.1.7. Radiative losses.

We use the following approximation for radiative losses due to recombination reactions:

$$Q^{\mathrm{rad,rec}}_{(\alpha,k)} = -\left(\phi^{\mathrm{ion}}_{(\alpha,k)}+\tfrac{1}{2}m_e\mathbf{u}_e^2\right)\Gamma^{\mathrm{rec}}_{(\alpha,k+1)}. \tag{36}$$

Currently other forms of energy loss through radiative processes (eg., bremsstrahlung, line radiation, etc.) are yet to be fully implemented.

4. BRIEF OVERVIEW OF NUMERICAL SOLUTION METHODS

4.1. Continuous Galerkin Spaital Discretization of Multifluid EM Model

The multi-fluid equations Figure 2-1 are a set of coupled hyperbolic subsystems of equations for modeling the dynamics of partially ionized plasma systems (neutrals, charged ions, and electrons) in the presence of electromagnetic fields. In the brief discussion that follows we present a robust and flexible stabilized scheme for the multifluid plasma system. The approach we consider is an algebraic flux corrected continuous Galerkin (CG) method. The AFC stabilization, we consider is an iterative local bounds preserving element based formulation [65, 62, 82, 81]. The AFC design in this work is a blocked stabilization of the hyperbolic system. This means that each subsystem (Euler for ions/neutrals, Euler for electrons and Maxwell equations) cab be stabilized separately. Alternate forms of stabilization that use the largest wave-speed bound for the coupled hyperbolic system are also of interest and the subject of our continuing development. The current block stabilized method is at least partially inspired by the blended scheme considered in [123]. We use CG for all

the Euler species subsystems and in the Maxwell equations when an all H(grad) basis is used, we include a divergence cleaning strategy based on a parabolic divergence cleaning method [35, 78, 122, 81]. The final stabilized semi-discrete scheme is integrated in time using various time integrators such as IMEX-RK strong stability preserving or BDF2 type methods.

4.1.1. Exact sequence discretizations {H(grad), H(curl), H(div)}

This section develops a Galerkin finite element discretization for the multi-fluid plasma model described in Section 2.4 and follows [89] and reuses text from this paper. To begin, the spatial domain is tiled by a set of hexahedral or tetrahedral (3D) elements. The finite element discretization uses basis functions that mimic the structure of the continuous representations (see [21, 19]). In particular, the goal is to develop a discretization for the multifluid EM plasma system (Figure 2-1) that satisfy the involutions satisfied by the continuous mathematical system by construction.

The discretization defines discrete basis functions to approximate the continuous function spaces

$$H_\nabla(\Omega) := \{v \in L^2(\Omega) : \nabla v \in \mathbf{L}^2(\Omega)\} \tag{37}$$

$$\mathbf{H}_{\nabla\times}(\Omega) := \{v \in \mathbf{L}^2(\Omega) : \nabla \times v \in \mathbf{L}^2(\Omega)\} \tag{38}$$

$$\mathbf{H}_{\nabla\cdot}(\Omega) := \{v \in \mathbf{L}^2(\Omega) : \nabla \cdot v \in L^2(\Omega)\} \tag{39}$$

defined on the domain Ω. The $L^2(\Omega)/\mathbf{L}^2(\Omega)$ space is defined as the set of square integrable scalar/vector functions. Figure 4-1 depicts that the derivative defined on one space maps this space into a subset of the next space. For example, if $v \in H_\nabla(\Omega)$ then $\nabla v \in \mathbf{H}_{\nabla\times}(\Omega)$. Define the discrete spaces as:

$$V_\nabla^h \subset H_\nabla(\Omega),\ \mathbf{V}_{\nabla\times}^h \subset \mathbf{H}_{\nabla\times}(\Omega),\ \mathbf{V}_{\nabla\cdot}^h \subset \mathbf{H}_{\nabla\cdot}(\Omega), \tag{40}$$

where the mesh refinement is indicated by the superscript h. Colloquially these spaces are referred to as the nodal, edge, and face spaces respectively. This relation reflects the continuity enforcement of the lowest order space: nodal spaces have point-wise continuity between elements (enforced by shared nodes), edge bases have tangential continuity (enforced by shared edges), and face bases have normal continuity (enforced by shared faces). These compatible spaces inherit the same derivative mapping properties of the continuous spaces; in particular

$$\nabla v \in \mathbf{V}_{\nabla\times}^h,\ \forall v \in V_\nabla^h, \tag{41}$$

$$\nabla \times v \in \mathbf{V}_{\nabla\cdot}^h,\ \forall v \in \mathbf{V}_{\nabla\times}^h. \tag{42}$$

These spatial derivatives are well defined because of the global continuity of the discrete spaces. In addition, not every set of discrete nodal, edge, and faces spaces satisfy this nesting property. These sequences must be carefully constructed to ensure the mapping property [21, 20, 6, 19].

To show that this discretization will satisfy the divergence involutions it is important to note that

$$\nabla \times \nabla v_\nabla = 0,\ \nabla \cdot \nabla \times v_{\nabla\times} = 0 \tag{43}$$

where v_∇ is in $H_\nabla(\Omega)$ or V_∇^h, and $v_{\nabla\times}$ is in $\mathbf{H}_{\nabla\times}(\Omega)$ or $\mathbf{V}_{\nabla\times}^h$. These are the commonly known vector calculus identities, which are preserved by the discretization to machine precision [89].

Discrete Variational Form. The governing conservation/balance laws (see Figure 2-1), describing the evolution of a fluid species in the presence of an electromagnetic field, can be written in the form

$$\partial_t U_\alpha + \nabla \cdot \mathbf{F}_\alpha(\mathbf{U}_\alpha) = S_\alpha(\mathbf{U}_\alpha, \mathbf{E}, \mathbf{B}) \tag{44}$$

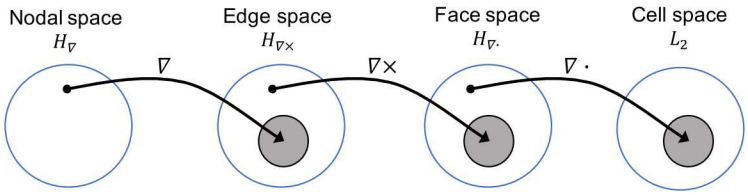

Figure 4-1. Representation of the relationships between the spaces associated with the exact sequence discretization. Note how the derivative operators $\nabla, \nabla\times$ and $\nabla\cdot$ map from one space to another, and that the gray area represents the null-space of the associated operator as described in Eq. (43). The discrete version of these spaces maintains this mapping property. The exact sequence property is essential for maintaining the involutions discretely.

with fluid state $U_\alpha \in \mathbf{U}_\alpha = \{\rho_\alpha, \mathbf{p}_\alpha, \epsilon_\alpha\}$, flux $\mathbf{F}$, and source S. The system is discretized using nodal fluid variables (e.g. $U_\alpha \in V_\nabla^h$) for all species, edge electric fields (e.g. $\mathbf{E} \in \mathbf{V}_{\nabla\times}^h$), and face magnetic fields (e.g. $\mathbf{B} \in \mathbf{V}_{\nabla\cdot}^h$). By multiplying the Euler subsystems for each species, α, Ampere's and Faraday's law (the Maxwell subsystem) by test functions in their respective spaces and integrating by parts, the discretized unknowns are found to satisfy

$$\int_\Omega \left(\partial_t U_\alpha - S_\alpha(\mathbf{U}_\alpha, \mathbf{E}, \mathbf{B})\right) v_U - \mathbf{F}(\mathbf{U}_\alpha) \cdot \nabla v_U \, dx + \oint_{\partial\Omega} \mathbf{F}(\mathbf{U}_\alpha) \cdot \mathbf{n} v_U \, ds = 0 \quad \forall U_\alpha \in \mathbf{U}_\alpha, \forall v_U \in V_\nabla^h, \forall \alpha \tag{45}$$

$$\int_\Omega \left(\partial_t \mathbf{E} + \frac{1}{\epsilon_0}\mathbf{j}\right) \cdot \mathbf{v}_E - c^2 \mathbf{B} \cdot \nabla \times \mathbf{v}_E \, dx + \oint_{\partial\Omega} c^2 \mathbf{n} \cdot (\mathbf{v}_E \times \mathbf{B}) \, ds = 0 \quad \forall \mathbf{v}_E \in \mathbf{V}_{\nabla\times}^h \tag{46}$$

$$\int_\Omega (\partial_t \mathbf{B} + \nabla \times \mathbf{E}) \cdot \mathbf{v}_B \, dx = 0 \quad \forall \mathbf{v}_B \in \mathbf{V}_{\nabla\cdot}^h. \tag{47}$$

As a result of the exact sequence property, satisfaction of Eq. (47) also implies that the strong form of Faraday's law is satisfied (because the strong curl of $\mathbf{E}$ is exactly representable by $\mathbf{B} \in \mathbf{V}_{\nabla\cdot}^h$) [89].

4.1.2. Continuous Galerkin H(grad) AFC spaital discretization

The multi-fluid equations Figure 2-1 are a set of coupled hyperbolic subsystems of equations for modeling the dynamics of partially ionized plasma systems (neutrals, charged ions, and electrons) in the presence of electromagnetic fields. In the brief discussion that follows we present a robust and flexible stabilized scheme for the multifluid plasma system. The approach we consider is an algebraic flux corrected continuous Galerkin (CG) method. The AFC stabilization, we consider is an iterative local bounds preserving element based formulation [65, 62, 82, 81]. The AFC design in this work is a blocked stabilization of the hyperbolic system. This means that each subsystem (Euler for ions/neutrals, Euler for electrons and Maxwell equations) is stabilized separately. This is partially inspired by the blended scheme considered in [123]. We use CG for all the subsystems and in the Maxwell equations, we include a divergence cleaning strategy based on a parabolic divergence cleaning method. The final stabilized semi-discrete scheme is integrated in time using various time integrators such as IMEX-RK strong stability preserving or BDF2 type methods.

Let $\Omega \subset \mathbb{R}^d$, $d = 1,2,3$ be a bounded domain with a Lipschitz boundary $\Gamma = \partial\Omega$. Let $T > 0$ be a given finite real number. For $(\mathbf{x}, t) \in \Omega \times [0, T]$, we consider the multifluid model for a partially ionized system as given in Figure 2-1, and consider a general development of the AFC CG method in the context of a conservation law system with source terms defined as

$$\frac{\partial \mathbf{U}}{\partial t} + \nabla \cdot \mathbf{F}(\mathbf{U}) = \mathbf{S}(\mathbf{U}). \tag{48}$$

The conserved quantity is $\mathbf{U} = [\{(\mathbf{U}_s),\ \forall s \in \Lambda\}, \mathbf{U}_{EM}]^T$. $\mathbf{U}_s = [\rho_s, \rho_s \mathbf{u}_s, \rho_s \mathcal{E}_s]^T$, and $\mathbf{U}_{EM} = [\mathbf{B}, \mathbf{E}]^T$. The physical flux $\mathbf{F}$ is given by

$$\mathbf{F} = \begin{bmatrix} \mathbf{F}_1(\mathbf{U}_1) \\ ..... \\ \mathbf{F}_{N_s}(\mathbf{U}_{N_s}) \\ \mathbf{F}_{EM}(\mathbf{U}_{EM}) \end{bmatrix}. \tag{49}$$

The physical flux for the fluid equations can then be written as

$$\mathbf{F}_s(\mathbf{U}_s) = \begin{bmatrix} \rho_s \mathbf{u}_s \\ \rho_s \mathbf{u}_s \otimes \mathbf{u}_s + p_s I \\ (\rho \mathcal{E}_s + p_s)\mathbf{u}_s \end{bmatrix}, \tag{50}$$

The physical flux for the electromagnetics can be written as

$$\mathbf{F}_{EM}(\mathbf{U}_{EM}) = \begin{bmatrix} \mathcal{T}(\mathbf{E}) \\ -c^2 \mathcal{T}(\mathbf{B}) \end{bmatrix}, \tag{51}$$

where for any vector $\mathbf{w} = [w_x, w_y, w_z] \in \mathbb{R}^3$,

$$\mathcal{T}(\mathbf{w}) = \begin{bmatrix} 0 & w_z & -w_y \\ -w_z & 0 & w_x \\ w_y & -w_x & 0 \end{bmatrix}.$$

The source term coupling the fluid equations to the Maxwell equations can be written as $\mathbf{S}(\mathbf{U}) = [\{(\mathbf{S}_s + \boldsymbol{\mathcal{C}}_s + \boldsymbol{\mathcal{S}}_s),\ \forall s \in \Lambda\}, \mathbf{S}_{EM}(\mathbf{U})]^T$, where

$$\mathbf{S}_s(\mathbf{U}) = \begin{bmatrix} 0 \\ \frac{q_s \rho_s}{m_s}(\mathbf{E} + \mathbf{u}_s \times \mathbf{B}) \\ \frac{q_s \rho_s}{m_s} \mathbf{u}_s \cdot \mathbf{E} \end{bmatrix}, \quad \mathbf{S}_{EM}(\mathbf{U}) = \begin{bmatrix} \mathbf{0} \\ -\mu_0 c^2 \sum_s \frac{q_s \rho_s}{m_s} \mathbf{u}_s \end{bmatrix}.$$

In the balance law (48), we do not take into full account, the constraints given by the involutions to the Maxwell system. These can be addressed by making use of divergence cleaning strategies [123]. Below, we will consider parabolic divergence cleaning.

Parabolic divergence cleaning. The parabolic divergence cleaning introduced here is similar to the MHD parabolic divergence cleaning in [35, 81]. Let $c_{h,B}$ and $c_{h,E}$ be the finite real numbers defined by the hyperbolic cleaning speed in [35] for the induction equation and the electric field equation respectively. Let $c_{p,B} = \sqrt{c_{h,B} c_r}$, and $c_{p,E} = \sqrt{c_{h,E} c_r}$, where $c_r = 0.18$. Then, the Maxwell equations will be modified in the following way

$$\frac{\partial \mathbf{B}}{\partial t} + \nabla \times \mathbf{E} - \nabla \cdot \left[c_{p,B}^2 (\nabla \cdot \mathbf{B}) I \right] = \mathbf{0}, \tag{52a}$$

$$\frac{\partial \mathbf{E}}{\partial t} - c^2 \nabla \times \mathbf{B} - \nabla \cdot \left[c_{p,E}^2 \left(\varepsilon_0 \nabla \cdot \mathbf{E} - \sum_s \frac{q_s \rho_s}{m_s} \right) I \right] = -c^2 \mu_0 \sum_s \frac{q_s \rho_s}{m_s} \mathbf{u}_s, \tag{52b}$$

The physical flux is then given by

$$\mathbf{F}^H_{EM}(\mathbf{U}) = \mathbf{F}_{EM}(\mathbf{U}_{EM}) + \mathbf{h}_{EM}(\mathbf{U}) = \begin{bmatrix} \mathcal{T}(\mathbf{E}) \\ -c^2\mathcal{T}(\mathbf{B}) \end{bmatrix} + \begin{bmatrix} -c^2_{p,B}(\nabla\cdot\mathbf{B})I \\ -c^2_{p,E}\left(\varepsilon_0\nabla\cdot\mathbf{E} - \sum_s \frac{q_s\rho_s}{m_s}\right)I \end{bmatrix}. \tag{53}$$

We will, therefore have an extra term in the fully coupled system, given by $\mathbf{h}(\mathbf{U}) = [\mathbf{0}, \mathbf{0}, \mathbf{h}_{EM}(\mathbf{U})]^T$. The result is the following modified balance law

$$\frac{\partial \mathbf{U}}{\partial t} + \nabla\cdot[\mathbf{F}(\mathbf{U}) + \mathbf{h}(\mathbf{U})] = \mathbf{S}(\mathbf{U}). \tag{54}$$

It should be noted that we can choose $c_{h,B} = c_{h,E} = c_h$ which depends on the maximum propagation speed for the Maxwell system. We will show below, in the finite element discretization, how the value for c_h is computed on the computational domain of the problem.

Finite element discretization. Consider the continuous formulation given by (54). Let S_h be a collection of elements K, that partition the domain Ω, such that $\Omega = \cup_{e=1}^{N_e} K_e$, where N_e is the total number of elements. These elements are assumed to be conforming and admissible. Let $V^h = \{v : \Omega \to \mathbb{R} \,:\, v|_K \in P^1(K), K \in S_h\}$ be the finite element space of element-wise linear/bilinear bases. Let $\{\phi_k\}_{k=1}^{N_h}$ be the basis that spans V_h. Denote by $\mathbf{U}_h$ the finite element approximation of $\mathbf{U}$. That is, $\mathbf{U}_h = \sum_k \hat{\mathbf{U}}_k\phi_k$, where $\hat{\mathbf{U}}_k = [\{(\rho_{s,k}, \rho_s\mathbf{u}_{s,k}, \rho_s\mathcal{E}_{s,k}), \forall s \in \Lambda\}, \mathbf{B}_k, \mathbf{E}_k]^T$ are the nodal values of the conserved variables. We will also denote by $\hat{\mathbf{U}}_{s,k} = [\rho_{s,k}, \rho\mathbf{u}_{s,k}, \rho\mathcal{E}_{s,k}]^T$, and $\hat{\mathbf{U}}_{EM,k} = [\mathbf{B}_k, \mathbf{E}_k]^T$. Note that, we can also write $\mathbf{U}_{s,h} = \sum_{k=1}^{N_h} \mathbf{U}_{s,k}\phi_k$, and $\mathbf{U}_{EM,h} = \sum_{k=1}^{N_h} \mathbf{U}_{EM,k}\phi_k$. The semi-discrete Galerkin scheme is given by the following.

Given $\mathbf{U}_h(\cdot, 0) = \mathbf{U}_0(\cdot) \in L^2(\Omega)$, find $\mathbf{U}_h(\cdot, t) \in (V^h)^{N_{eq}}$ a.e $(0, T)$ such that

$$\frac{d}{dt}\int_\Omega \phi\mathbf{U}_h d\mathbf{x} + \int_\Gamma \phi[\mathbf{F}(\mathbf{U}_h) + \mathbf{h}(\mathbf{U}_h)]\cdot\mathbf{n}d\sigma - \int_\Omega \nabla\phi\cdot[\mathbf{F}(\mathbf{U}_h) + \mathbf{h}(\mathbf{U}_h)]d\mathbf{x} = \int_\Omega \phi\mathbf{S}(\mathbf{U}_h)d\mathbf{x}, \tag{55}$$

for all $\phi \in V^h$, where N_{eq} is the number of conserved variables in (54).

The semi-discrete scheme in matrix form is given by

$$\mathbf{M}_C\frac{d\hat{\mathbf{U}}}{dt} + \mathbf{K}(\hat{\mathbf{U}}) + \mathbf{H}(\hat{\mathbf{U}}) + \mathbf{B}_\Gamma(\hat{\mathbf{U}}) + \mathbf{S}(\hat{\mathbf{U}}) = \mathbf{0}, \tag{56}$$

where

$$\begin{aligned}
\mathbf{M}_C &= \{M_{kl}\}_{k,l=1}^{N_h},\ M_{kl} = m_{kl}I_{N_{eq}\times N_{eq}},\ m_{kl} = \int_\Omega \phi_k\phi_l d\mathbf{x}, && (57)\\
\mathbf{K}(\hat{\mathbf{U}}) &= \{\mathbf{k}_k\}_{k=1}^{N_h},\ \mathbf{k}_k = -\int_\Omega \nabla\phi_k\cdot\mathbf{F}(\mathbf{U}_h)d, && (58)\\
\mathbf{H}(\hat{\mathbf{U}}) &= \{\mathbf{h}_k\}_{k=1}^{N_h},\ \mathbf{h}_k = -\int_\Omega \nabla\phi_k\cdot\mathbf{h}(\mathbf{U}_h)d\mathbf{x}, && (59)\\
\mathbf{B}_\Gamma(\hat{\mathbf{U}}) &= \{\mathbf{b}_k\}_{k=1}^{N_h},\ \mathbf{b}_k = \int_\Gamma \phi_k[\mathbf{F}(\mathbf{U}_h) + \mathbf{h}(\mathbf{U}_h)]\cdot\mathbf{n}d\sigma, && (60)\\
\mathbf{S}(\hat{\mathbf{U}}) &= \{\mathbf{S}_k\}_{k=1}^{N_h},\ \mathbf{S}_k = -\int_\Omega \phi_k\mathbf{S}(\mathbf{U}_h)d\mathbf{x}. && (61)
\end{aligned}$$

The inclusion of $\mathbf{B}_\Gamma$ depends on the prescribed boundary conditions. This semi-discrete scheme, when solved without any stabilization may result in spurious oscillations developing in the solution profile. The

next step is to introduce suitable stabilization that will eliminate spurious oscillations. This will be achieved by introducing some artificial diffusion to the semi-discrete system whose amount is regulated by a solution dependent limiter [82]. First, we need to consider the eigen-system for the two fluid equations. Details of this can be found also in [60].

Eigen-system for the two-fluid equations. In this section, the eigenvalues and eigenvectors of the Euler subsystem and Maxwell equations will be presented. These will be useful in the following sections where the stabilization will be presented. The stabilization involves introduction of artificial diffusion based on the eigensystem of the Euler and Maxwell equations. First, denote by $\mathbf{u}_s = [u_s, v_s, w_s]^T$ the components of the velocity for each specie in $\mathbb{R}^3$. Note that in $\mathbb{R}^2$, this will be $\mathbf{u}_s = [u_s, v_s]^T$.

The eigenvalues of $\mathbf{n} \cdot \mathbf{F}'_s(\mathbf{U}_s)$, the flux Jacobian, in the direction of a unit vector $\mathbf{n} \in \mathbb{R}^d$, are given by

$$\Lambda_s(\mathbf{U}_s, \mathbf{n}) = \text{diag}\left(\{\mathbf{u}_s \cdot \mathbf{n} - c_s, \mathbf{u}_s \cdot \mathbf{n}, \mathbf{u}_s \cdot \mathbf{n} + c_s, \mathbf{u}_s \cdot \mathbf{n}\}\right), \tag{62}$$

where $c_s = \sqrt{\frac{p_s \gamma_s}{\rho_s}}$ is the sound speed. The eigenvector matrix is given, in $\mathbb{R}^2$, by

$$R_s(\mathbf{U}_s, \mathbf{n}) = \begin{bmatrix} 1 & 1 & 1 & 0 \\ u_s - c_s n_x & u_s & u_s + c_s n_x & n_y \\ v_s - c_s n_y & v_s & v_s + c_s n_y & -n_x \\ H_s - c_s \mathbf{u}_s \cdot \mathbf{n} & \frac{1}{2}\|\mathbf{u}_s\|^2 & u_s n_y - v_s n_x & H_s + c_s \mathbf{u}_s \cdot \mathbf{n} \end{bmatrix}. \tag{63}$$

The eigenvalues and eigenvectors in $\mathbb{R}^3$ can be found in [109]. For the Maxwell systems, we only consider the eigenvalues of $\mathbf{F}'_{EM}(\mathbf{U}_{EM}) \cdot \mathbf{n}$ which are given by $\Lambda_{EM}(\mathbf{U}_{EM}, \mathbf{n}) = \text{diag}\left(\{-c, -c, 0, 0, c, c\}\right)$. In the next section, the stabilization based on artificial diffusion computed using the above quantities will be presented.

Stabilization. The stabilization strategy here will follow the algebraic flux correction strategy as in [82] for Euler equations and reactive flow problems. The subsystems will be stabilized separately. The fluid equations will be stabilized using scalar or tensorial diffusion as in [82]. The Maxwell system will be stabilized using scalar diffusion. The following diffusion operators will be considered:

$$\mathbf{D}_s(\mathbf{U}_s) = \left\{D_{s,kl}(\mathbf{U}_s)\right\}_{k,l=1}^{N_h}, \text{ with } D_{s,kl}(\mathbf{U}_s) = \sum_e D_{s,kl}^{(e)}(\mathbf{U}_s), \tag{64}$$

and

$$\mathbf{D}_{EM}(\mathbf{U}_{EM}) = \left\{D_{EM,kl}(\mathbf{U}_{EM})\right\}_{k,l=1}^{N_h}, \text{ with } D_{EM,kl}(\mathbf{U}_{EM}) = \sum_e D_{EM,kl}^{(e)}(\mathbf{U}_{EM}). \tag{65}$$

Here $\mathbf{D}_s$ are the fluid artificial diffusion operators for species s. They could be either Rusanov (scalar) diffusion operators or Roe diffusion operators. If we have Rusanov diffusion, then $D_{s,kl}^{(e)} = d_{s,kl}^{(e)} I_{(d+2)\times(d+2)}$ for $l \neq k$, and $D_{s,kk}^{(e)} = -\sum_{l \neq k} D_{s,kl}^{(e)}$, where

$$d_{s,kl}^{(e)}(\mathbf{U}) = \max\left(\lambda_{\max}(\mathbf{F}'_s(\mathbf{U}_{s,l}) \cdot \mathbf{c}_{kl}^{(e)}), \lambda_{\max}(\mathbf{F}'_s(\mathbf{U}_{s,k}) \cdot \mathbf{c}_{lk}^{(e)})\right), \; l \neq k, \tag{66}$$

and

$$\mathbf{c}_{kl}^{(e)} = \int_{K_e} \nabla \phi_k \phi_l d\mathbf{x}. \tag{67}$$

If we have Roe diffusion, then we can recall that the eigen-decomposition for the flux Jacobian is given by $\mathbf{n}\cdot\mathbf{F}'_s(\mathbf{U}_s) = R_s(\mathbf{U}_s,\mathbf{n})\Lambda_s(\mathbf{U}_s,\mathbf{n})R_s^{-1}(\mathbf{U}_s,\mathbf{n})$, where $\mathbf{n}$ is a unit vector. In a component-wise formulation, this can be written as

$$\mathbf{F}'_{s,\xi}(\mathbf{U}_s) = \mathbf{e}_\xi\cdot\mathbf{F}'_{s,\xi}(\mathbf{U}_s) = R^\xi(\mathbf{U}_s)\Lambda^\xi(\mathbf{U}_s)[R^\xi(\mathbf{U}_s)]^{-1}, \tag{68}$$

where $\mathbf{e}_\xi = [\delta_{1\xi},\ldots,\delta_{d\xi}]^T$, for $\xi = 1,\ldots,d$ are the canonical basis for $\mathbb{R}^d$, and $\delta_{\eta\xi} = 1$ if $\eta = \xi$ and 0 otherwise. The element-wise Roe dissipation using a split tensorial representation is given by

$$\begin{aligned}
D^{(e)}_{s,kl} &= \sum_{\xi=1}^{d} \tilde{c}^\xi_{kl} R^\xi_s(\mathbf{U}_{s,kl})|\Lambda^\xi_s(\mathbf{U}_{s,kl})|[R^\xi_s(\mathbf{U}_{s,kl})]^{-1}, \text{ for } l\neq k,\\
D^{(e)}_{s,kk} &= -\sum_{l\neq k} D^{(e)}_{s,kl},
\end{aligned}$$

where the direction vector $\mathbf{c}^{(e)}_{kl} = \mathbf{c}^{(e)}_{lk}$. For example, we could have $\tilde{\mathbf{c}}^{(e)}_{kl} = [\tilde{c}^{1,(e)}_{kl},\ldots,\tilde{c}^{d,(e)}_{kl}]^T$, $\tilde{c}^{\xi,(e)}_{kl} = \max\left(|c^{\xi,(e)}_{kl}|,|c^{\xi,(e)}_{lk}|\right)$. $\mathbf{U}_{s,kl}$ is a suitable average of the s^{th} species, such as an arithmetic average $\mathbf{U}_{s,kl} = \frac{1}{2}(\mathbf{U}_{s,k}+\mathbf{U}_{s,l})$, or the Roe average[82].

Now we consider the artificial diffusion for the Maxwell system. The maximum eigenvalue is given by $\lambda_{\max}(\mathbf{n}\cdot\mathbf{F}'_{EM}(\mathbf{U}_{EM})) = c\|\mathbf{n}\|$, where $\mathbf{n}\in\mathbb{R}^d$. The Rusanov artificial diffusion is then obtained from $D^{(e)}_{EM,kl} = d^{(e)}_{EM,kl}I_{6\times6}$ for $l\neq k$, and $D^{(e)}_{EM,kk} = -\sum_{l\neq k} D^{(e)}_{EM,kl}$, where

$$d^{(e)}_{EM,kl}(\mathbf{U}) = \max\left(\lambda_{\max}(\mathbf{F}'_{EM}(\mathbf{U}_{EM,l})\cdot\mathbf{c}^{(e)}_{kl}),\lambda_{\max}(\mathbf{F}'_{EM}(\mathbf{U}_{EM,k})\cdot\mathbf{c}^{(e)}_{lk})\right),\ l\neq k. \tag{69}$$

The element-wise artificial diffusion for the system is given in block diagonal form by

$$\mathbf{D}^{(e)}(\mathbf{U}^{(e)}) = \begin{bmatrix} D^{(e)}_1\left(\mathbf{U}^{(e)}_1\right) & \ldots\ldots & \mathbf{0} & \mathbf{0}\\ \vdots & \ddots & \vdots & \vdots\\ \mathbf{0} & \ldots\ldots & D^{(e)}_{N_s}\left(\mathbf{U}^{(e)}_{N_s}\right) & \mathbf{0}\\ \mathbf{0} & \ldots\ldots & \mathbf{0} & D^{(e)}_{EM}\left(\mathbf{U}^{(e)}_{EM}\right)\end{bmatrix}, \tag{70}$$

where $\mathbf{U}^{(e)}_s$ is the restriction of $\mathbf{U}_s$ to the nodes lying on the element K_e. The same applies to $\mathbf{U}^{(e)}_{EM}$.

It should be noted that the left hand side of (56) can be assembled from the following element-wise contributions

$$\mathcal{R}^{(e)}_H = \mathbf{M}^{(e)}_C\frac{d\mathbf{U}^{(e)}}{dt} + \mathbf{K}^{(e)}(\mathbf{U}) + \mathbf{H}^{(e)}(\mathbf{U}) + \mathbf{B}^{(e)}_\Gamma(\mathbf{U}) + \mathbf{S}^{(e)}(\mathbf{U}). \tag{71}$$

The AFC stabilization procedure involves adding the artificial diffusion with the operator $\mathbf{D}^{(e)}$ to this element-wise assembly and the lumping of the mass matrix associated with the time derivative. The result is the following *low order* semi-discrete contribution

$$\mathcal{R}^{(e)}_L = \mathbf{M}^{(e)}_L\frac{d\mathbf{U}^{(e)}}{dt} + \mathbf{K}^{(e)}(\mathbf{U}) + \mathbf{H}^{(e)}(\mathbf{U}) + \mathbf{D}^{(e)}(\mathbf{U})\mathbf{U}^{(e)} + \mathbf{B}^{(e)}_\Gamma(\mathbf{U}) + \mathbf{S}^{(e)}(\mathbf{U}). \tag{72}$$

The difference between this low order element-wise contributions and the *high order* contributions is the following *anti-diffusive* part

$$\mathcal{F}^{(e)} = -\mathbf{D}^{(e)}(\mathbf{U})\mathbf{U}^{(e)} + (\mathbf{M}_C^{(e)} - \mathbf{M}_L^{(e)})\frac{d\mathbf{U}^{(e)}}{dt}. \tag{73}$$

The low order scheme obtained from (72) is diffusive and is designed to be local extremum diminishing (LED) in the case of the characteristic variables of a linearized hyperbolic first order conservation law system. In general this approximation will result in a diffusive representation. The goal is to have a scheme that is high resolution. In the AFC stabilization algorithm, this is achieved by adding *limited* element-wise counterparts of $\mathcal{F}^{(e)}$ that add back as much of the high-order approximation as possible without violating the LED property. This limited contribution is given by

$$\bar{\mathcal{F}}^{(e)} = \begin{bmatrix} \Phi_1^{(e)}\mathcal{F}_1^{(e)} \\ \vdots \\ \Phi_{N_s}^{(e)}\mathcal{F}_{N_s}^{(e)} \\ \Phi_{EM}^{(e)}\mathcal{F}_{EM}^{(e)} \end{bmatrix}, \tag{74}$$

where $\Phi_s^{(e)}$ and $\Phi_{EM}^{(e)}$ are quantities between 0 and 1. These values are such they vanish in elements that have a steep front or a shock and are close to unit in elements where the solution is smooth or linear. A detailed discussion of the construction of these limiters follows in the next section.

We can now summarize the stabilized semi-discrete up to this point to the quantity assembled from the following element residual contributions

$$\mathcal{R}^{(e)} = \mathbf{M}_L^{(e)}\frac{d\mathbf{U}^{(e)}}{dt} + \mathbf{K}^{(e)}(\mathbf{U}) + \mathbf{H}^{(e)}(\mathbf{U}) + \mathbf{D}^{(e)}(\mathbf{U})\mathbf{U}^{(e)} + \mathbf{B}_\Gamma^{(e)}(\mathbf{U}) + \mathbf{S}^{(e)}(\mathbf{U}) + \bar{\mathcal{F}}^{(e)}. \tag{75}$$

Limiting strategy. In this section, we present the limiting strategy used in the AFC algorithm. This is the method used to compute $\Phi_s^{(e)}$ and $\Phi_{EM}^{(e)}$. For a given variable u, we define $\Phi_u^{(e)} = \min_{k\in N(K_e)}(1 - [\mu_k^u]^q)$, $q \geq 1$. μ_k^u for $k = 1, ..., N_h$ is a linearity preserving limiter given by

$$\mu_k^u = \frac{\left|\sum_{l\neq k}\beta_{kl}(u_l - u_k)\right| + \epsilon}{\sum_{l\neq k}\beta_{kl}|u_l - u_k| + \epsilon},\ \epsilon \approx 10^{-16}, \tag{76}$$

where $\beta_{kl} > 0$ such that $\sum_{l\neq k}\beta_{kl}\mathbf{g}_k \cdot (\mathbf{x}_l - \mathbf{x}_k) = 0$. The scales β_{kl} are assembled using the following Kuzmin linearity preservation strategy:

(i) Compute the nodal gradients are first using a lumped mass L^2 projection of ∇u_h.

$$\mathbf{g}_k = \frac{1}{m_k}\sum_{l\neq k}\mathbf{c}_{lk}(u_l - u_k),\ \mathbf{c}_{kl} = \sum_e \mathbf{c}_{kl}^{(e)}. \tag{77}$$

(ii) Compute $S_k^\pm$ for each k:

$$\begin{aligned} S_k^+ &= \sum_{l\neq k}\max\left\{0, \mathbf{g}_k \cdot (\mathbf{x}_l - \mathbf{x}_k)\right\}, \\ S_k^- &= \sum_{l\neq k}\min\left\{0, \mathbf{g}_k \cdot (\mathbf{x}_l - \mathbf{x}_k)\right\} \end{aligned} \tag{78}$$

(iii) Compute nodal correction factors σ_k^+ and σ_k^-:

$$\begin{aligned}\sigma_k^+ &= \min\left\{1, \frac{|S_k^-| + \varepsilon}{S_k^+ + \varepsilon}\right\},\\ \sigma_k^- &= \min\left\{1, \frac{S_k^+ + \varepsilon}{|S_k^-| + \varepsilon}\right\}.\end{aligned} \tag{79}$$

The fluxes into node k and the nodal correction factors must satisfy for each component, this zero sum condition

$$\sigma_k^+ S_k^+ + \sigma_k^- S_k^- = 0. \tag{80}$$

(iv) Compute the positive scales β_{kl}:

$$\beta_{kl} = \begin{cases}\sigma_k^+, \text{ if } \mathbf{g}_k \cdot (\mathbf{x}_l - \mathbf{x}_k) > 0,\\ \sigma_k^-, \text{ if } \mathbf{g}_k \cdot (\mathbf{x}_l - \mathbf{x}_k) \le 0.\end{cases} \tag{81}$$

In the stabilized scheme, for example we set $\Phi_s^{(e)} = \min\left\{\Phi_{\rho_s}^{(e)}, \Phi_{\rho_s p_s}^{(e)}\right\}$, and $\Phi_{EM}^{(e)} = \min\left\{\Phi_{\frac{1}{2}\|\mathbf{m}B\|^2}^{(e)}, \Phi_{\frac{1}{2}\|\mathbf{m}E\|^2}^{(e)}\right\}$.

4.2. Temporal Discretization

IMEX methods allow implicit evolution of stiff modes in an ODE, while maintaining explicit evolution of slow modes. To achieve this, IMEX methods work with ODEs with an additive separation of scales:

$$\frac{\partial y(t)}{\partial t} + g(y,t) = f(y,t). \tag{82}$$

Here g contains operators generating *fast* time scales, while f contains operators generating *slow* time scales. This qualitative ordering of the time scales is defined relative to a desired time scale that is intended to be resolved by the simulation. This time scale is specified by the user selected time-step Δt. As a guiding principle, the forward-Euler stability limit of the fastest resolved mode is used to determine the time step size.

IMEX methods can be written as both linear multi-step [7, 52], multi-stage Runge–Kutta schemes [9, 22, 47, 48, 49, 61], and multi-step multi-stage Runge–Kutta (general linear multi-step (GLM)) [134, 135, 113]. This work focuses on multi-stage IMEX Runge-Kutta (IMEX-RK) schemes presented in [9, 96, 98], though extensions to multi-step formulations are straightforward. Similar to implicit and explicit Runge-Kutta algorithms, IMEX-RK defines a sequence of solutions at different stages in the time interval. These solutions are combined with appropriate quadrature weights to produce the solution at the end of the time-step. Stated concisely, the stage updates and final summation satisfy:

$$y^{(i)} = y^n + \Delta t \sum_{j=1}^{i-1} \hat{A}_{ij} f(y^{(j)}, t^n + \hat{c}_j \Delta t) - \Delta t \sum_{j=1}^{i} A_{ij} g(y^{(j)}, t^n + c_j \Delta t) \qquad \text{for } i = 1 \dots s, \tag{83}$$

$$y^{n+1} = y^n + \Delta t \sum_{i=1}^{s} \hat{b}_i f(y^{(i)}, t^n + \hat{c}_i \Delta t) - \Delta t \sum_{i=1}^{s} b_i g(y^{(i)}, t^n + c_i \Delta t). \tag{84}$$

Here s is the number of stages, and the coefficients come from implicit and explicit Butcher tableaus:

$$\begin{array}{c|c}\hat{c} & \hat{A}\\ \hline & \hat{b}^T\end{array} \quad \text{is explicit, and} \quad \begin{array}{c|c}c & A\\ \hline & b^T\end{array} \text{ is implicit.} \tag{85}$$

Terms in these tableaus define the computational, accuracy, and stability properties of the method. In this work the implicit A matrix is lower triangular, while the explicit $\hat{A}$ matrix is strictly lower triangular. This ensures that the IMEX scheme is diagonally implicit, and contributions from the slow terms are handled explicitly. More information on these tables, and their derivation, can be found in [9, 96, 98].

A pseudocode description of the IMEX-RK algorithm, including the storage of the stage contributions, is:

for $i = 1 \dots s$ **do**
  $\tilde{y} \leftarrow y^n + \Delta t \sum_{j=1}^{i-1} \hat{A}_{ij} F_j - \Delta t \sum_{j=1}^{i-1} A_{ij} G_j$
  Solve $y^{(i)} - \tilde{y} + \Delta t A_{ii} g(y^{(i)}, t_n + c_i \Delta t) = 0$ for $y^{(i)}$
  $F_i \leftarrow f(y^{(i)}, t_n + \hat{c}_i \Delta t)$
  $G_i \leftarrow (\tilde{y} - y^{(i)}) \frac{1}{A_{ii} \Delta t}$
end for
$y^{n+1} \leftarrow y^n + \Delta t \sum_{i=1}^{s} \hat{b}_i F_i - \Delta t \sum_{i=1}^{s} b_i G_i$

A careful examination of the algorithm demonstrates that there are two physics-dependent computational steps: (i) the explicit evolution and computations of the intermediate value $\tilde{y}$, and (ii) the solution of the nonlinear system

$$\mathcal{R}(y) = y - \tilde{y} + \alpha g(y) = 0 \tag{86}$$

for y, accounting for the implicit time evolution of the stiff physics.

4.2.1. Strong Stability Preserving Methods

The exact solution of a hyperbolic conservation law of the form $U_t = f(U)_x$ frequently develops sharp gradients or discontinuities, which may cause significant difficulties in numerical simulations. High order spatial discretizations that feature nonlinear non-inner-product stability properties that mimic some significant physical properties of the exact solution are desirable. Such properties are designed to ensure that the spatial discretization $F(u)$ (where u is a vector of approximations to U) satisfies the forward Euler condition

$$\|u^{n+1}\| \leq \|u^n\|, \quad 0 \leq \Delta t \leq \Delta t_{FE}, \tag{87}$$

(for u^n is a discrete approximation to U at time t^n) where $\|\cdot\|$ is the desired norm, semi-norm, or convex functional.

Often, higher order Runge–Kutta methods can be decomposed into convex combinations of forward Euler steps [119], so that given an F that satisfies the forward Euler condition, these Runge–Kutta methods will preserve the monotonicity property $\|u^{n+1}\| \leq \|u^n\|$, usually under a modified time-step restriction $\Delta t \leq \mathcal{C}\, \Delta t_{\text{FE}}$. Any method that can be written as such a convex combination so that with $\mathcal{C} > 0$ is called a *strong stability preserving (SSP)* method. These methods ensure that any strong stability property satisfied by the spatial discretization when using the forward Euler condition (87) is preserved by the higher order strong stability preserving Runge–Kutta method.

The time-step restriction $\Delta t \leq \mathcal{C} \Delta t_{\text{FE}}$ is comprised of two factors: the forward Euler time-step Δt_{FE} that comes from the spatial discretization, and the SSP coefficient $\mathcal{C}$ that is a property only of the time-discretization. The research on SSP methods focuses on optimizing the allowable time-step $\Delta t \leq \mathcal{C} \Delta t_{\text{FE}}$ by maximizing the *SSP coefficient* $\mathcal{C}$ of the method.

High order strong stability preserving (SSP) time discretizations have proven beneficial for use with spatial discretizations with nonlinear stability properties for the solution of hyperbolic PDEs. SSP Runge–Kutta methods suffer from barriers on their order: explicit SSP Runge–Kutta methods cannot be more than fourth-order accurate [57, 110] and implicit SSP Runge–Kutta methods cannot be more than sixth-order accurate [44]. However, when we consider the accuracy of the methods when applied to linear problems, these barriers relax: explicit Runge–Kutta methods of any *linear order* can be found in [44].

The search for high order strong stability time-stepping methods with large allowable strong stability time-step has been an active area of research over the last two decades. In the work [33] we found implicit-explicit (IMEX) SSP Runge–Kutta methods with large allowable time-step, that feature high linear order and simultaneously have varying designed orders of accuracy for for linear and non linear components.

In general, most of the time integration for numerical solution of ODEs are computed with a single formula and a fixed step-size. This type of approach can be non-optimal if the solution varies rapidly over small subsets of the integration interval and slowly over larger ones [32]. Using a uniform step-size, such that $\Delta t_n = \Delta t$ is the same at every time step, the local error would vary at each time step since the error depends on the properties of f and its derivatives. A small constant step-size may help resolve regions with large variation in solution, at the expense of unnecessary computation in the region of less variability.

In an attempt to minimize the computational cost and obtain the best possible result, it is necessary to use an adaptive method based on automatic step-size selection (Appendix D). Numerical computation based on adaptive methods varies the step-size Δt_n such that the local error can be uniformly distributed at each time step t_n. Such an approach is akin to using non uniform Chebyshev nodes in polynomial interpolation. Practical error estimates are necessary to choose the step-size Δt_n sufficiently small to obtain the required precision of the numerical solution and ensure Δt_n is large enough to avoid unnecessary computational work. In [32], we construct a family of embedded pairs for optimal strong stability preserving explicit Runge–Kutta methods of order $2 \le p \le 4$ to be used to obtain numerical solution of spatially discretized hyperbolic PDEs. The extension to DIRK and IMEX-RK will be explored in future works.

4.3. Nonlinear/Linear Solvers

The result of a fully-implicit or IMEX time discertizaion is the development of very large-scale, coupled highly nonlinear system(s) that must be solved. Therefore, these techniques place a heavy burden on both the nonlinear and linear solvers and require robust, scalable, and efficient nonlinear solution methods. In this study, Newton-based iterative nonlinear solvers [37] are employed to solve the challenging nonlinear systems that result in this application. These solvers can exhibit quadratic convergence rates independently of the problem size when sufficiently robust linear solvers are available. For the latter, we employ Krylov iterative techniques. A Newton-Krylov (NK) method [25] is an implementation of Newton's method in which a Krylov iterative solution technique is used to approximately solve the linear systems that are generated at each step of Newton's method. Specifically, to solve the nonlinear system $\mathcal{R}(\mathcal{U}) = \mathbf{0}$, we seek a zero of $\mathcal{R} : R^N \to R^N$ where $\mathcal{U} \in R^N$ is a current approximate solution. The Krylov iterative solver is applied to the linearized residual equation

$$\mathcal{J}_k \mathbf{s}_{k+1} = -\mathcal{R}_k, \tag{88}$$

where $\mathcal{J}_k$ is the Jacobian matrix and $\mathcal{R}_k$ is the nonlinear residual, both of which are evaluated at the previous Newton step solution $\mathbf{U}_k$. The solution for the Newton direction vector, $\mathbf{s}_{k+1}$, is used to update the previous solution in the sequence. For efficiency an inexact Newton method [36, 41] is usually employed, whereby one approximately solves (88) by choosing a forcing term η_{k+1}, and stopping the Krylov iteration when the inexact Newton condition

$$\|\mathcal{R}_k + \mathcal{J}_k \mathbf{s}_{k+1}\| \le \eta_{k+1} \|\mathcal{R}_k\| \tag{89}$$

is satisfied. For efficient implementation, an adaptive convergence criteria can be employed [40, 118, 103], and to increase robustness, backtracking of the provisional Newton step can be enforced to ensure a sufficient reduction of the nonlinear residual before the step is accepted [37, 103].

4.4. Automatic Differentiation

For fully-implicit and IMEX schemes, we construct an explicit Jacobian matrix for solving the linear system in the Newton-Krylov scheme. This provides an exact matrix-vector apply multiply and allows for a wide range

Cores	Total Unknowns	Relative Time
256	7.93m	1.000
1024	31.5m	1.002
4096	126m	0.998
8192	253m	1.012
16384	504m	1.011
32768	1.01b	1.015
65536	2.01b	1.014

Table 4-1. Weak scaling study of Jacobian evalaution time using automatic differentiation on IBM Blue Gene for semiconductor device problem.

of preconditioning strategies when approximating the Jacobian inverse. To generate this matrix, we have developed a set of finite element assembly tools built upon a template-based implementation of automatic differentiation.

The automatic differentiation library, Sacado, and the finite element assembly tools, Phalanx and Panzer, are packages available in Trilinos [46]. Sacado implements automatic differentiation by providing new scalar types with overloads of the math operators to evaluate the derivatives [101]. Users write their nonlinear residual equations templated on the scalar type. For a nonlinear residual, one would compile and call the function with a scalar type of double. To get Jacobian sensitivities, one would compile and call the same code with a Sacado scalar type. This significantly speeds up development as the application developer only need write a single residual evaluation. This results in a smaller code base, allows us to get sensitivities wrt any parameter in the code, and eliminates the time consuming effort of deriving, implementing and debugging Jacobians. We get tremendous flexibility for, e.g. adjoints and parametric sensitivity analysis, without placing the burden of hand coding derivatives on the application developers.

The equation evaluation routines are broken into individual functors with explicit direct dependencies. In this way we can build up multiphysics applications by analyzing the functors and building a directed acyclic graph (DAG) of functor dependencies. When more equations are added or the models are changed, we can easily accomplish these changes at runtime by adding or swapping functors (nodes in the DAG) and rebuilding the DAG connectivity. This gives flexibility in comparing discretizations and material models. The DAG management and evaluation is handled by the Phalanx package [95, 101]. The parallel distributed finite element assembly is handled by the Panzer package. The automatic differentiation is applied at the local element level for efficiency [102]. Table 4-1 shows an example of weak scaling of the evaluation of the Jacobian for a semiconductor device simulation on an IBM Blue Gene.

4.5. Parallel Scalability of Solvers

4.5.1. Weak scalability of coupled AMG for MHD system

A critical component of solving large-scale MHD applications is our fully-coupled AMG (FC-AMG) preconditioner [126, 111, 70, 71, 112, 74, 43, 75, 117, 72]. This capability is also a fundamental aspect of our physics-based (PB) / approximate block preconditioning (ABF) preconditioning approaches for complex multiphysics, as well as mixed spatial discertizations (e.g. node, edge, face, volume). To demonstrate this critical capability we present results of a weak scaling study for our resistive MHD formulation for an MHD duct flow problem with FC-AMG-preconditioned Newton-Krylov solvers on a BlueGene Q platform on up to 1M+ cores [72] and compared these with the Titan Cray XK7 results. Representative results are presented in Figure 4-2. These results demonstrate excellent weak scalability on large-scale problems. The largest steady-state fully-coupled solves to date have 1.625B unstructured finite-elements and 13B unknowns on 128K cores. For transients we have performed CFD solves for 10B elements with 40B unknowns on 128K cores. We have also demonstrated

the solution to Poisson-type sub-problems, which are important kernels for our block preconditioners, on up to 1.6M cores of BG/Q [72]. These results, while important on their own, also serve as a valuable baseline for

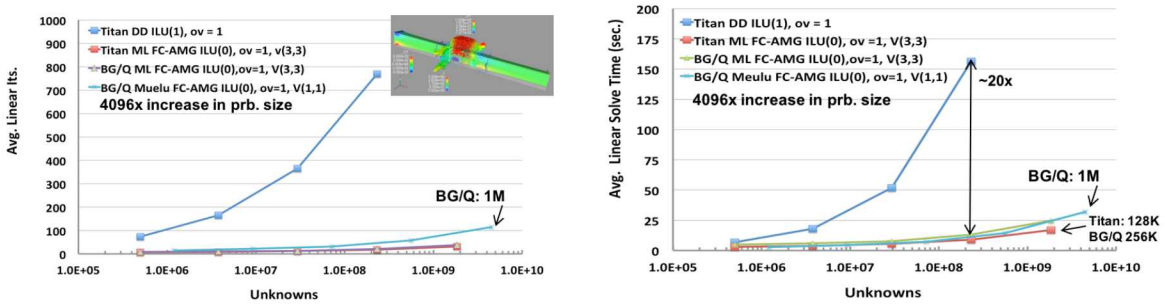

(a) Average iteration count

(b) CPU time

Figure 4-2. Illustration of parallel weak scaling of fully-coupled AMG for MHD.

comparison and provide confidence as we develop and analyze ABF preconditioners for MHD and multifluid plasma formulations based on structure-preserving discretizations, for which no FC-AMG system multilevel solver exists.

4.5.2. PB and ABF preconditioners for implicit full two-fluid formulations.

Full two-fluid models allow for charge separation effects beyond the resistive / extended MHD model and bring in additional, very stiff hyperbolic wave phenomena (light waves and plasma waves [125]). To deal with these time-scales we have developed a PB/ABF preconditioning strategy for this complex system. Our development of a multifluid plasma preconditioner has treated all plasma species together. The Jacobian for the two-fluid (ion/electron) / full-Maxwell plasma model (see Figure 2-1), neglecting some property variations, is represented in fully-discrete form as:

$$\begin{bmatrix}
\mathbf{D}_{\rho_i} & \mathcal{K}^{\rho_i}_{(\rho u)_i} & 0 & \mathbf{Q}^{\rho_i}_{\rho_e} & 0 & 0 & 0 & 0 \\
\mathcal{K}^{(\rho u)_i}_{\rho_i} & \mathbf{D}_{(\rho u)_i} & 0 & \mathbf{Q}^{(\rho u)_i}_{\rho_e} & \mathbf{Q}^{(\rho u)_i}_{(\rho u)_e} & 0 & \mathbf{Q}^{(\rho u)_i}_{E} & \mathbf{Q}^{(\rho u)_i}_{B} \\
\mathbf{D}^{\mathcal{E}_i}_{\rho_i} & \mathbf{D}^{\mathcal{E}_i}_{(\rho u)_i} & \mathbf{D}_{\mathcal{E}_i} & \mathbf{Q}^{\mathcal{E}_i}_{\rho_e} & \mathbf{Q}^{\mathcal{E}_i}_{(\rho u)_e} & \mathbf{Q}^{\mathcal{E}_i}_{\mathcal{E}_e} & \mathbf{Q}^{\mathcal{E}_i}_{E} & 0 \\
\mathbf{Q}^{\rho_e}_{\rho_i} & 0 & 0 & \mathbf{D}_{\rho_e} & \mathcal{K}^{\rho_e}_{(\rho u)_e} & 0 & 0 & 0 \\
\mathbf{Q}^{(\rho u)_e}_{\rho_i} & \mathbf{Q}^{(\rho u)_e}_{(\rho u)_i} & 0 & \mathbf{D}^{(\rho u)_e}_{\rho_e} & \mathbf{D}_{(\rho u)_e} & 0 & \mathbf{Q}^{(\rho u)_e}_{E} & \mathbf{Q}^{(\rho u)_e}_{B} \\
\mathbf{Q}^{\mathcal{E}_e}_{\rho_i} & \mathbf{Q}^{\mathcal{E}_e}_{(\rho u)_i} & \mathbf{Q}^{\mathcal{E}_e}_{\mathcal{E}_i} & \mathbf{D}^{\mathcal{E}_e}_{\rho_e} & \mathbf{D}^{\mathcal{E}_e}_{(\rho u)_e} & \mathbf{D}_{\mathcal{E}_e} & \mathbf{Q}^{\mathcal{E}_e}_{E} & 0 \\
0 & \mathbf{Q}^{E}_{(\rho u)_i} & 0 & 0 & \mathbf{Q}^{E}_{(\rho u)_e} & 0 & \mathbf{Q}_{E} & \mathbf{K}^{E}_{B} \\
0 & 0 & 0 & 0 & 0 & 0 & \mathbf{K}^{B}_{E} & \mathbf{Q}_{B}
\end{bmatrix}
\begin{bmatrix}
\rho_i \\ (\rho \mathbf{u})_i \\ \mathcal{E}_i \\ \rho_e \\ (\rho \mathbf{u})_e \\ \mathcal{E}_e \\ \mathbf{E} \\ \mathbf{B}
\end{bmatrix}$$

Here, the notation for the matrices is as follows: $\mathbf{D}$ corresponds to generalized transient and advection operators, possibly including diffusion; $\mathcal{K}$ corresponds to first-order derivative operators for divergence and gradient; $\mathbf{K}$ corresponds to first-order curl operators; and finally $\mathbf{Q}$ corresponds to mass matrices or source terms (i.e. not containing any derivatives). To enable a wide range of spatial discretizations and efficient preconditioners for the implicit time integration of this system, we have developed preconditioners based on the following algorithmic design criteria:

1. Fluid variables partitioned separate from the EM variables to allow disparate discretizations (e.g. nodal FE or FV methods for the compressible conservation variables and structure-preserving discretizations for EM).
2. The electric field $\mathbf{E}$, and the magnetic induction $\mathbf{B}$, will be partitioned to allow disparate discrete approximations to be employed (e.g. edge elements for the electric field and face elements for the the magnetic field.)

3. The variable partitioning, and the ABF preconditioners, should be efficient in the large time-step limit of Maxwell (i.e. not resolving speed of light), and should also enable use of this formulation and ABF preconditioner in a single fluid MHD formulation solving for $\mathbf{E}, \mathbf{B}$.
4. All ABF and Schur-complement approximations should be compatible with scalar/system nodal AMG (H(grad), FC-AMG), and curl-curl AMG (H(curl)) methods in the multilevel **Trilinos** packages **ML/Muelu**.

An ABF preconditioner that satisfies criteria (1) - (4) has been developed based on the following 3×3 block partition with $\mathbf{F} = (\rho_i, (\rho\mathbf{u})_i, \mathcal{E}_i, \rho_e, (\rho\mathbf{u})_e, \mathcal{E}_e)$ [106]. The combined block system is shown below, along with the upper-triangular preconditioner (for which the lower triangular factor is omitted [92, 34]):

$$\begin{bmatrix} \mathbf{D}_F & \mathbf{Q}_E^F & \mathbf{Q}_B^F \\ \mathbf{Q}_F^E & \mathbf{Q}_E & \mathbf{K}_B^E \\ 0 & \mathbf{K}_E^B & \mathbf{Q}_B \end{bmatrix} \begin{bmatrix} \mathbf{F} \\ \mathbf{E} \\ \mathbf{B} \end{bmatrix}, \qquad \begin{bmatrix} \hat{\mathbf{S}}_F & 0 & 0 \\ \mathbf{Q}_F^E & \hat{\mathbf{S}}_E & 0 \\ 0 & \mathbf{K}_E^B & \mathbf{Q}_B \end{bmatrix} \begin{bmatrix} \mathbf{F} \\ \mathbf{E} \\ \mathbf{B} \end{bmatrix}. \tag{90}$$

The fluid flow Schur-complement is defined as $\hat{\mathbf{S}}_F = \hat{\mathbf{D}}_F - \mathbf{Q}_F^E \bar{\mathbf{S}}_E^{-1} (\mathbf{Q}_E^F - \mathbf{Q}_E^F \bar{\mathbf{Q}}_B^{-1} \mathbf{K}_E^B)$. Additionally the electric-field Schur-complement is defined as $\hat{\mathbf{S}}_E = \mathbf{Q}_E - \mathbf{K}_B^E \bar{\mathbf{Q}}_B^{-1} \mathbf{K}_E^B$. The terms in $\hat{\mathbf{S}}_E$ can intuitively be seen to correspond to the transient operator and the Schur-complement for Maxwell's equations that would have a curl curl type operator, just as the continuous development of the 2nd order form of Maxwell would exhibit. The terms are, from left to right, the displacement current, the curl-curl operator, and a perturbation due to the electromagnetic force acceleration of the fluid momentum that reflects currents that are coupled into Ampere's law. To allow this system to be solved for large light-wave CFL, we use the grad-div stabilization of the Schur-complement [104] as outlined in [106]. This preconditioner admits multilevel solves of the

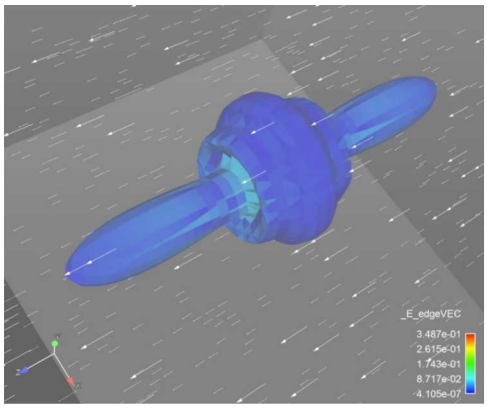

(a) Constant Ion Density Surface

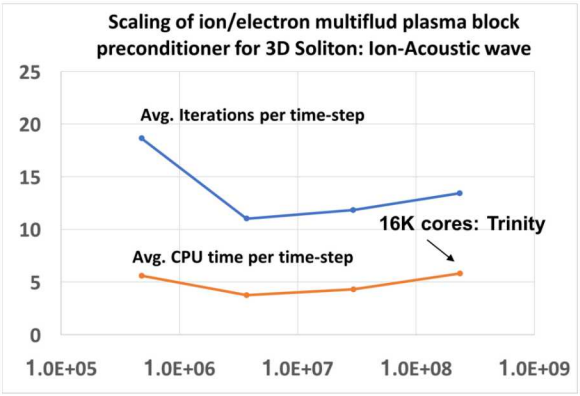

(b) ABF scaling fully ionized magnetized plasma expansion

Figure 4-3. Illustration scaling of fully ionized multifluid plasma model with structure-preserving discretizations

Schur-complement for the edge-based electric field with optimal H(curl) AMG, then followed by a solve of the fluid system with optimal system projection H(grad) FC-AMG, and then a simple mass matrix inversion to compute the magnetic field. In Figure 4-3, we present a weak scaling study as a proof of principle for an electron/ion plasma with an under-resolved transverse electromagnetic (TEM) wave. In the case of the multifluid plasma, we have demonstrated the capability to step over very restrictive fast time-scale physics as we describe below in Section 5.4. These methods have demonstrated significant promise for an entire set of scalable efficient preconditioners for this important class of advanced plasma physics models.

5. VERIFICATION RESULTS WITH RELEVANCE TO MIF

This section presents a sequence of brief results that are intended to provide an initial demonstration of the accuracy and robustness of the multifluid EM plasma model. These results cover a hierarchy of basic

results range from collisionless one-dimensional multifluid wave solutions, verification of the ionization, recombination, and elastic scattering source terms, and the solution of the full multifluid EM plasma model in the visco-resistive MHD limit. These verification problems include:

- Warm longitudinal electron/ion plasma oscillation with both an electrostatic and full Maxwell EM representation [Section 5.1.1].
- Cold Langmuir (a.k.a. longitudinal electron plasma) oscillation (LEP) [Section 5.1.1].
- Left- and right-hand circularly polarized (LCP, RCP) waves in a magnetized electron plasma [Section 5.1.2].
- Collisional relaxation and damped plasma oscillations [Section 5.2.1].
- Equilibrium ionization fractions for a coronal model with constant electron temperature [Section 5.3].
- Solution of the full multifluid EM plasma model in the asymptotic limit of visco-resistive MHD [Section 5.4].

5.1. Verification and Evaluation on Collisionless Plasmas

The linear waves are derived from a static two-fluid plasma where the background flow velocity and electric field are assumed zero with a constant background density, pressure, and magnetic field, as discussed in [18]. The main waves of interest are ordinary waves, electrostatic waves, and polarization waves. These waves are generally derived in terms of bulk plasma quantities such as the bulk plasma frequency

$$\omega_p = \sqrt{\sum_\alpha \omega_{p\alpha}^2}, \tag{91}$$

cyclotron frequency,

$$\omega_c = \sqrt{\sum_\alpha \omega_{c\alpha}^2}, \tag{92}$$

sound speed,

$$v_s = \sqrt{\sum_\alpha v_{s\alpha}^2}, \tag{93}$$

and skin depth

$$d = \sqrt{\sum_\alpha d_\alpha^2}. \tag{94}$$

Ordinary waves are light waves which have a polarization (oscillation direction of electric field perturbations) along the background magnetic field, leading to coupling to the plasma consistent with an unmagnetized plasma. Electrostatic waves describe the wave like behavior due to charge separation. Polarization waves, where the background magnetic field points along the wave's propagation direction, include the left hand circularly polarized wave (LCP) and right-handed circularly polarized wave (RCP). Both electrostatic and polarization waves have multiple branches depending on the number of particle species.

5.1.1. Linear waves in unmagnetized plasma

The linear waves are presented in a normalized form, where the oscillation frequency of the linear wave ω is normalized by the bulk plasma frequency: ω/ω_p. The wave number k_x is similarly normalized by the bulk skin depth: $k_x d$. The simulations are setup to resolve a single wavelength such that the domain width is $L_x = 2\pi/k_x$.

Figure 5-5 compares the branches of electrostatic and polarization waves with the ordinary wave. Resolving time and length scales associated with these waves becomes more difficult with decreasing frequency and increasing wavenumber.

A simple analysis was done for each wave by seeding the simulation with the waveform, evolving over three periods, and measuring the frequency by looking at the time of the zero crossings for the species momenta.

A subset of the frequency test points shown in Fig. 5-5 where chosen for further study by convergence analysis. The points, represented by the circles in [89, Fig. 3], were chosen to stress the consistent integration of stiff implicit terms with resolved explicit dynamics.

Two-fluid electrostatic waves are broken into fast and slow branches. The fast electrostatic wave, commonly known as Langmuir oscillations, is tied to electron dynamics, while the slower wave is associating with the heavier ion species. The dispersion relation for two-fluid electrostatic waves,

$$A_e + A_i = A_e A_i, \tag{95}$$

is written in terms of the non-dimensional parameters

$$A_\alpha = \frac{\omega_p^2}{\omega_{p\alpha}^2}\left(\frac{\omega^2}{\omega_p^2} - \frac{v_{s\alpha}^2}{c^2}k_x^2 d^2\right). \tag{96}$$

The solution to the dispersion relation is written in terms of two non-dimensional parameters C_0 and C_1

$$\frac{\omega^2}{\omega_p^2} = \frac{1}{2}(C_0 \pm C_1). \tag{97}$$

Here '+' refers the the fast electrostatic wave, and '−' the slow wave. The parameters are given by

$$C_0 = 1 + x^2 \tag{98}$$

$$C_1 = \sqrt{C_0^2 - 4x^2(\alpha_i^2\beta_e^2 + \alpha_e^2\beta_i^2 + \alpha_e^2\alpha_i^2 x^2)} \tag{99}$$

with

$$x = \frac{v_s}{c}k_x d \tag{100}$$

and

$$\alpha_i^2 = \frac{1}{1. + \frac{m_i}{m_e}\frac{T_e}{T_i}} \qquad \alpha_e^2 = \frac{1}{1. + \frac{m_e}{m_i}\frac{T_i}{T_e}}$$

$$\beta_i^2 = \frac{1}{1. - \frac{q_e}{q_i}\frac{m_i}{m_e}} \qquad \beta_e^2 = \frac{1}{1. - \frac{q_i}{q_e}\frac{m_e}{m_i}}.$$

Solutions to this dispersion relation, see [89, Fig. 3], show the asymptotic short-wavelength behavior tend toward the acoustic speeds of the individual species.

The analytic solution for the plasma variables are given by

$$\rho_\alpha = m_\alpha n_0 \left(1 + \delta_\alpha \sin(k_x x - \omega t)\right), \tag{101}$$

$$u_x^\alpha = \delta_\alpha \frac{\omega}{k_x} \sin(k_x x - \omega t), \tag{102}$$

$$P_\alpha = k_B n_0 T_0 \left(1 + \gamma \delta_\alpha \sin(k_x x - \omega t)\right), \tag{103}$$

and

$$E_x = \frac{\delta_e - \delta_i}{k_x} \frac{e n_0}{\epsilon_0} \cos(k_x x - \omega t). \tag{104}$$

The system is closed with a relation between the perturbation amplitudes

$$\frac{\delta_i}{\delta_e} = -\frac{A_e}{A_i} \tag{105}$$

where $\delta_\alpha \ll 1$.

The test space is defined by a mass ratio $m_i = 100 m_e$, and a temperature ratio $T_e = 10 T_i$ chosen to increase the inflection magnitude for the electrostatic dispersion relation. The base temperature was chosen such that $c = 10 v_s$. The background density is set to $n_0 = 10^{18}\,[m^{-3}]$, and the speed of light and elementary charge are realistic. The electron perturbation is set at $\delta_e = 10^{-7}$.

The error convergence for this wave are shown in Fig. 5-2 (IMEX-RK) for tree test points and Fig. 5-1 (DIRK). Table 5-1 shows the time scales for the most stiff result $k_x d = 250$, where 2^{nd} order convergence is shown for IMEX-RK while stepping over the speed of light by two orders of magnitude, and the electron sound speed by one order of magnitude.

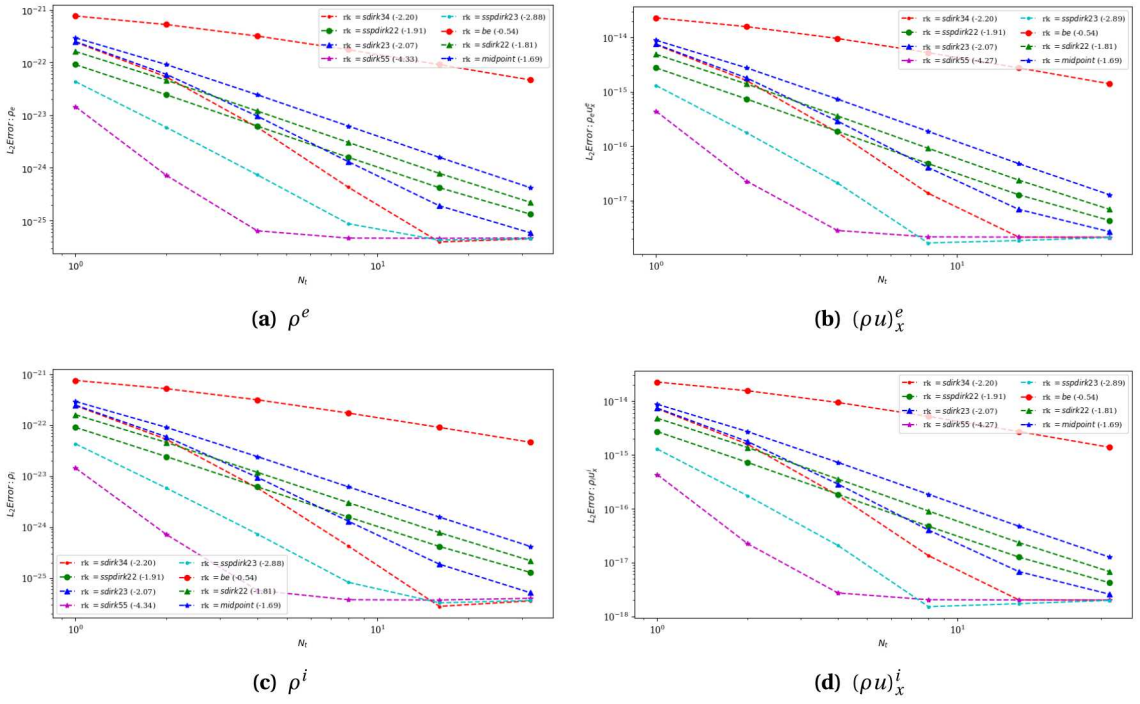

(a) ρ^e **(b)** $(\rho u)_x^e$

(c) ρ^i **(d)** $(\rho u)_x^i$

Figure 5-1. Slow electrostatic wave L_2 convergence at a constant CFL at a tenth of a transit time $t = \pi/(5\omega)$ using the ES formulation. Results show the expected order accuracy of the respective DIRK methods. Mesh resolution ranges from 10 to 320 cells per wavelength.

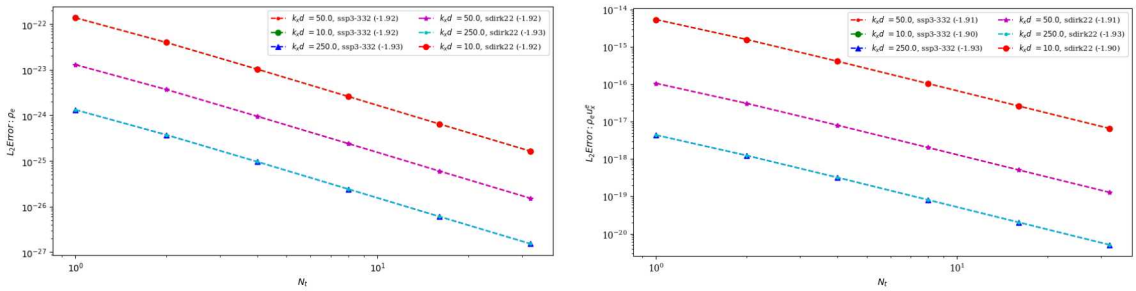

(a) ρ^e **(b)** $(\rho u)_x^e$

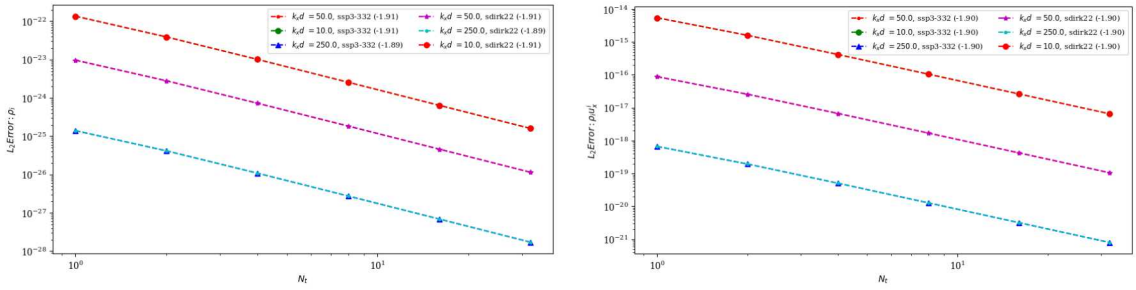

(c) ρ^i **(d)** $(\rho u)_x^i$

Figure 5-2. Slow electrostatic wave L_2 convergence at a constant CFL at a tenth of a transit time $t = \pi/(5\omega)$ using EB formualtion. Results show the expected 2^{nd} order accuracy of the IMEX-RK method. Mesh resolution ranges from 10 to 320 cells per wavelength.

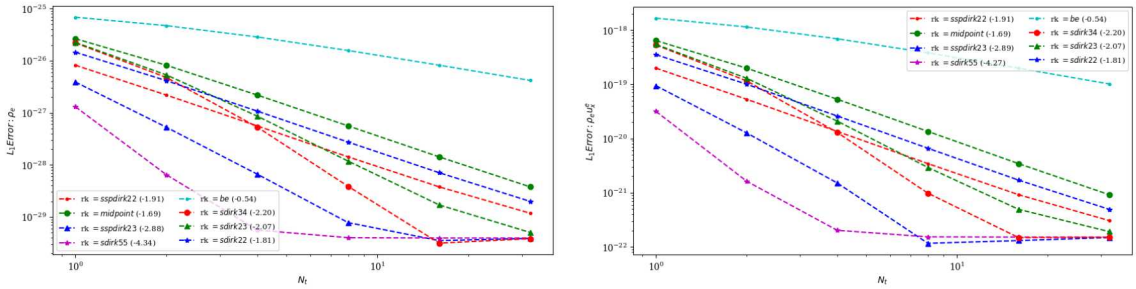

(a) ρ^e **(b)** $(\rho u)_x^e$

Figure 5-3. Slow warm electron electrostatic wave L_2 convergence at a constant CFL using the ES formulation. Results show the expected order accuracy of the respective DIRK methods. Mesh resolution ranges from 10 to 320 cells per wavelength.

The error convergence for an unmagnetized warm electron plasma is shown in Fig. 5-3 for various implicit methods. Here, the ion species are assumed to be immobile, and represented exclusively as a constant charge density $n_i = n_0$.

The cold unmagnetized electron plasma waves, absence of thermal pressure and no energy equation in the system, are the simplest version of the general formulation above. The collionseless cold LEP wave mode solution is simplified:

Table 5-1. Time scales slow electrostatic wave with $k_x d = 250$. Frequency time scales are expressed as a range since convergence is tested over a constant CFL such that $\Delta t = \frac{1}{2}\frac{k_x}{\omega}\Delta x$. Operators associated with bold terms were treated implicitly.

	Electrons	Ions
$\omega_p \Delta t$	**0.11 - 3.4**	$2.5 \cdot 10^{-3}$ - $7.9 \cdot 10^{-2}$
$\omega_c \Delta t$	**0.053 - 1.7**	$2.9 \cdot 10^{-5}$ - $9.2 \cdot 10^{-4}$
$v_s \frac{\Delta t}{\Delta x}$	**67**	0.5
$c \frac{\Delta t}{\Delta x}$		**672**

$$\rho_e(x,t) = m_e n_0 \left[1 + \delta \sin(k x_1 - \omega t)\right] \tag{106}$$
$$\mathbf{u}_e(x,t) = \frac{|\omega|}{k}\delta \left[\sin(k x_1 - \omega_R t), 0, 0\right] \tag{107}$$
$$\mathbf{E}(x,t) = \frac{e}{n_0}\epsilon_0 k \delta \left[\cos(k x_1 - \omega_R t), 0, 0\right] \tag{108}$$
$$\mathbf{B}(x,t) = 0 \tag{109}$$

The error convergence for an unmagnetized cold electron plasma is shown in Fig. 5-4 for various implicit methods.

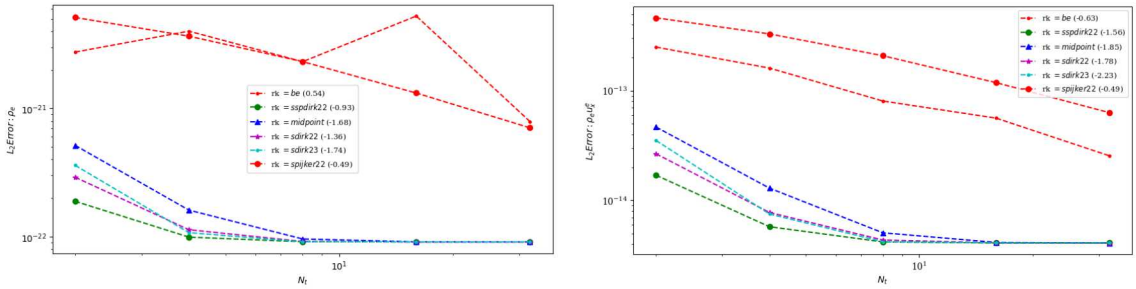

(a) ρ^e **(b)** $(\rho u)^e_x$

Figure 5-4. Slow cold electron electrostatic wave L_2 convergence at a constant CFL using the ES formulation. Results show the expected order accuracy of the respective DIRK methods. Mesh resolution ranges from 10 to 320 cells per wavelength.

The convergence results for the total energy in the warm electron-ion and warm electron plasma oscillation was unsatisfactory for higher order methods. We are currently investigating these observed order reduction.

5.1.2. Linear waves in a magnetized cold plasma: LCP, RCP

In this section a straightforward dispersion verification study is presented for linear waves in a magnetized cold plasma. Specifically the left/right hand circularly polarized waves (LCP,RCP). In Figure 5-5 the analytic dispersion relation is presented and a selected number of computations down with the Drekar multifluid plasma model.

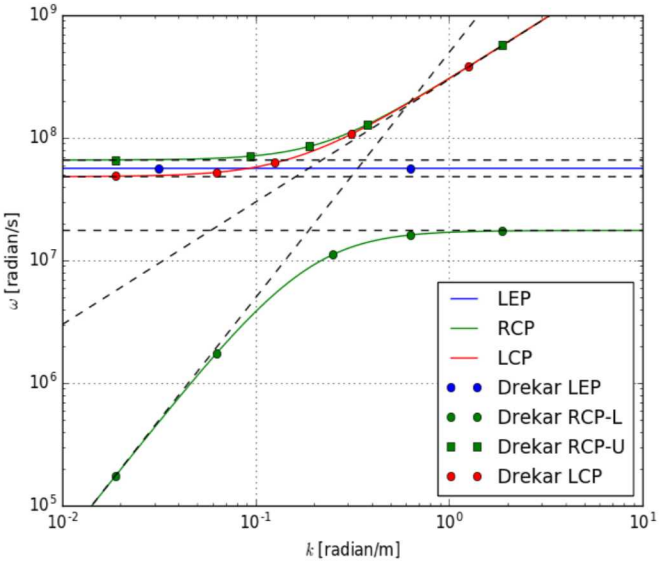

Figure 5-5. Dispersion diagram for linear waves in a magnetized cold plasma (LCP,RCP)

5.2. Verification and Evaluation on Collisional Plasmas

A collection of tests are considered here with the aim of verifying that the various source terms required for the general multifluid model described in Section 3.1 are correctly implemented in the Drekar code. In each test, it is assumed that:

(i) all quantities lack spatial gradients; and

(ii) all external source terms ($\mathcal{S}_s^{[0]}$, $\boldsymbol{\mathcal{S}}_s^{[1]}$, $\mathcal{S}_s^{[2]}$) are zero.

In this case, the fluid equations (4) reduce to

$$\partial_t \rho_s = \mathcal{C}^{[0]}, \tag{110a}$$

$$\partial_t \left(\rho_s \mathbf{u}_s\right) = \frac{q_s}{m_s} \rho_s \left(\mathbf{E} + \mathbf{u}_s \times \mathbf{B}\right) + \boldsymbol{\mathcal{C}}_s^{[1]}, \tag{110b}$$

$$\partial_t \mathcal{E}_s = \frac{q_s}{m_s} \rho_s \mathbf{u}_s \cdot \mathbf{E} + \mathcal{C}_s^{[2]}. \tag{110c}$$

5.2.1. Collisional relaxation

First, we consider the transfer of momentum and energy between a collection of two or more species through elastic collisions. Including only interactions due to elastic scattering collisions, the momentum and energy sources for each species, using (20) and (34), are given by

$$\boldsymbol{\mathcal{C}}_s^{[1]} = \sum_{t \neq s} \alpha_{s;t} \rho_s \rho_t \left(\mathbf{u}_t - \mathbf{u}_s\right), \tag{111a}$$

$$\mathcal{C}_s^{[2]} = \sum_{t \neq s} \left[\alpha_{s;t} \rho_s \rho_t \mathbf{u}_s \cdot \left(\mathbf{u}_t - \mathbf{u}_s\right) + \frac{\alpha_{s;t} \rho_s \rho_t}{m_s + m_t} \left[3 k_\mathrm{B} \left(T_t - T_s\right) + m_t \left(\mathbf{u}_t - \mathbf{u}_s\right)^2 \right] \right]. \tag{111b}$$

	Neutral (n)	Ion (i)	Electron (e)
m_s	3.0E-27	2.0E-27	1.0E-27
T_s	1.0E+3	1.0E+4	2.0E+4
$\mathbf{u}_s$	$\begin{bmatrix}0.0\\0.0\\0.0\end{bmatrix}$	$\begin{bmatrix}1.0\text{E}{+4}\\0.0\\0.0\end{bmatrix}$	$\begin{bmatrix}-1.4\text{E}{+4}\\0.0\\0.0\end{bmatrix}$
n_s	4.0E+16	2.0E+16	2.0E+16

	Neutral (n)	Ion (i)	Electron (e)
ρ_s	1.2E-10	4.0E-11	2.0E-11
$\rho_s\mathbf{u}_s$	$\begin{bmatrix}0.0\\0.0\\0.0\end{bmatrix}$	$\begin{bmatrix}4.0\text{E}{-7}\\0.0\\0.0\end{bmatrix}$	$\begin{bmatrix}-2.8\text{E}{-7}\\0.0\\0.0\end{bmatrix}$
$\rho_s e_s$	8.2860E-4	4.1430E-3	8.2860E-3
$\mathcal{E}_s$	8.2860E-4	6.1430E-3	1.0246E-2

Table 5-2. Initial conditions for collisional verification problems.

An equation of state for an ideal monatomic gas is assumed for each species, so that the internal energy densities satisfy

$$\rho_s e_s = \frac{1}{\gamma-1} n_s k_\text{B} T_s, \tag{112}$$

with $\gamma = 5/3$. The electric field $\mathbf{E}$ and magnetic field $\mathbf{B}$ are both assumed to be zero (ie., external fields are assumed to be absent and the contributions from any fields induced by the motion of charged particles are neglected).

In these tests, the species simply relax to common velocity and temperature values $\mathbf{u}_*$ and T_* as $t \to \infty$. By conservation of momentum, it must hold that

$$\sum_s \rho_s \mathbf{u}_s = \mathbf{u}_* \sum_s \rho_s \tag{113}$$

for all times, which implies that

$$\mathbf{u}_* = \frac{\sum_s \rho_s \mathbf{u}_s}{\sum_s \rho_s}. \tag{114}$$

Similarly, conservation of energy requires that

$$\sum_s \mathcal{E}_s = \sum_s \left(\frac{1}{2}\rho_s \mathbf{u}_s^2 + \frac{1}{\gamma-1} n_s k_\text{B} T_s \right) = \frac{1}{2}\mathbf{u}_*^2 \sum_s \rho_s + \frac{1}{\gamma-1} k_\text{B} T_* \sum_s n_s, \tag{115}$$

for all times, which implies that

$$T_* = \frac{\sum_s \mathcal{E}_s - \frac{1}{2}\mathbf{u}_*^2 \sum_s \rho_s}{\frac{1}{\gamma-1} k_\text{B} \sum_s n_s}. \tag{116}$$

We consider three scenarios:

(i) A two-fluid system with constant friction coefficients,

(ii) A three-fluid system with constant friction coefficients, and

(iii) A three-fluid system with friction coefficients computed using (22) and (25).

All scenarios use the initial conditions shown in Table 5-2, with only ions and electrons included in the two-fluid case. Solutions computed using the Drekar code were compared to: (i) the time evolution of an explicit ODE solver applied to a reduced system for the velocities and temperatures of the species, and (ii) the analytic equilibrium values given by (114) and (116). Deviations of all values from the equilibrium quantities are computed in a relative sense; eg.,

$$\left| \frac{T_s - T_*}{T_*} \right|. \tag{117}$$

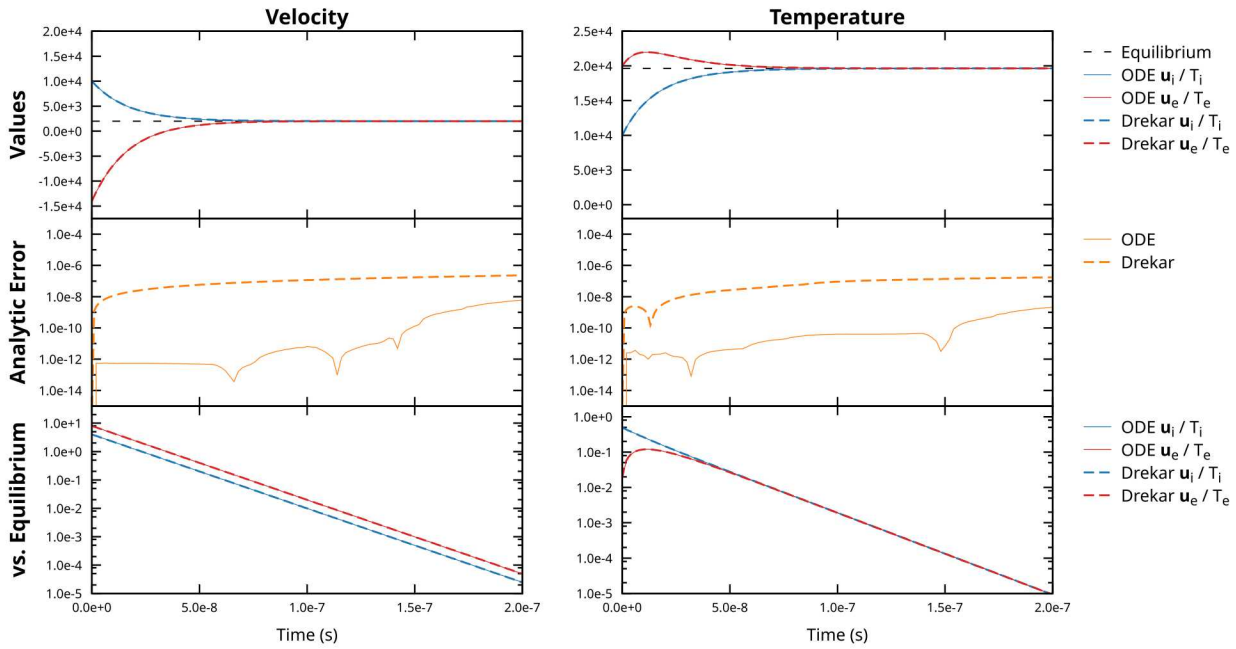

Figure 5-6. Results for two-fluid collisional relaxation problem.

If the friction coefficients $\alpha_{s;t}$ are assumed to be constant, analytic solutions may be derived for the two-fluid case. The velocity difference between species is given by

$$\mathbf{u}_e(t) - \mathbf{u}_i(t) = \left(\mathbf{u}_e(t_0) - \mathbf{u}_i(t_0)\right) \exp\left(-A_{e;i}\, t\right), \tag{118}$$

where

$$A_{e;i} = \alpha_{e;i}\left(\rho_e + \rho_i\right), \tag{119}$$

and the temperature difference between species is given by

$$T_e(t) - T_i(t) = \left(T_e(t_0) - T_i(t_0)\right) \exp\left(-B_{e;i}\, t\right) + \frac{C_{e;i}}{B_{e;i} - 2A_{e;i}} \left[\exp\left(-2A_{e;i}\, t\right) - \exp\left(-B_{e;i}\, t\right)\right], \tag{120}$$

where

$$B_{e;i} = 3\left(\gamma - 1\right)\alpha_{e;i} \frac{m_e m_i}{m_e + m_i}\left(n_e + n_i\right), \tag{121}$$

$$C_{e;i} = \frac{\gamma - 1}{k_\mathrm{B}} \alpha_{e;i}\left(\rho_i - \rho_e\right) \frac{m_e m_i}{m_e + m_i}\left(\mathbf{u}_e(t_0) - \mathbf{u}_i(t_0)\right)^2. \tag{122}$$

The time evolution of numerically computed velocity and temperature values from Drekar and an explicit ODE solver are compared in Figures 5-6 and 5-7. For the two-fluid case in Figure 5-6, each solver is additionally compared to the analytic solutions (118) and (120). We observe that: (i) the numerical implementations are in very good agreement, (ii) each numerical implementation relaxes toward the appropriate equilibrium values, and (iii) both numerical implementations yield small errors relative to the analytic solutions for the two-fluid case. The results of convergence studies using various implicit and explicit time-integration schemes made available through the Tempus library are shown in Figure 5-8 for a simulation time of $t = 4.0\text{E-}8$. The expected convergence orders are observed for all schemes considered.

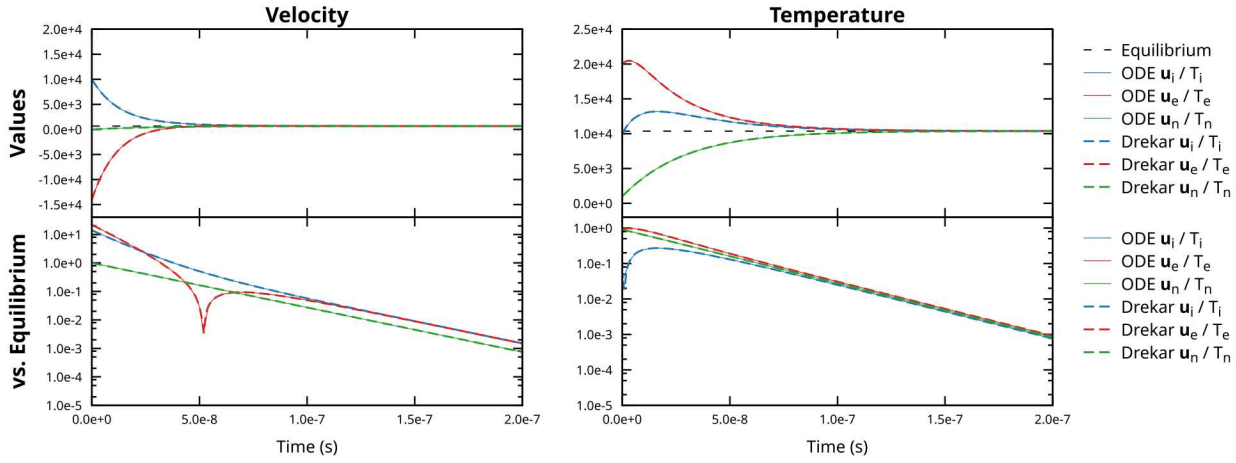

(a) Three-fluid relaxation problem with constant friction coefficients.

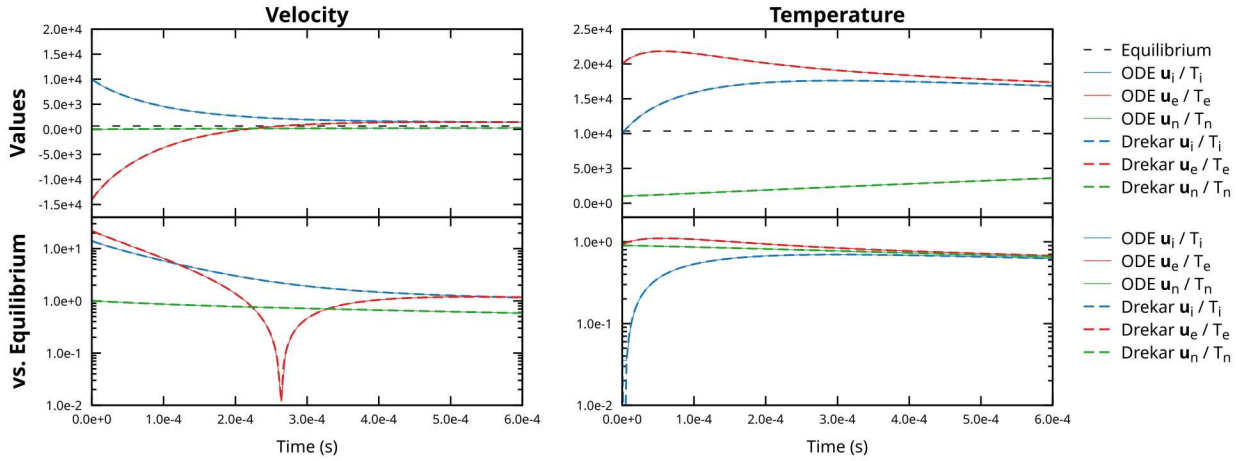

(b) Three-fluid collisional relaxation problem with friction coefficients computed using (22) and (25).

Figure 5-7. Results for three-fluid collisional relaxation problems.

5.2.2. Three-species plasma oscillations

We now consider cases where the effects of electric fields induced by the motion of charged particles are included, but contributions due to magnetic fields and external electric fields are omitted. Here the evolution of the electric field $\mathbf{E}$ is described by

$$\epsilon_0 \partial_t \mathbf{E} + \mathbf{J} = \mathbf{0}, \tag{123}$$

where ϵ_0 is the permittivity of free space and the total current density $\mathbf{J}$ is given by

$$\mathbf{J} \stackrel{\text{def}}{=} \sum_s \frac{q_s}{m_s} \rho_s \mathbf{u}_s. \tag{124}$$

We consider four scenarios:

(i) A collisionless two-fluid system containing ion and electron species interacting only through the electric field coupling. The result is an undamped oscillation.

(ii) A collisional two-fluid system containing ion and electron species with constant friction coefficients with the value $\alpha_{e;i} = 1.0\text{E}{+}18$. The result is a damped oscillation.

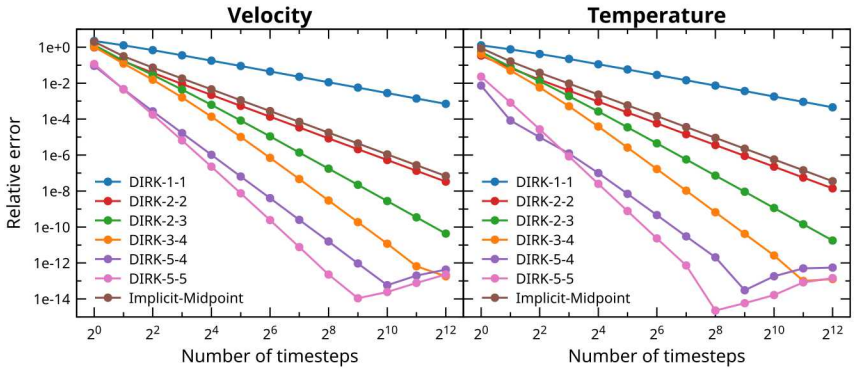

(a) Implicit methods.

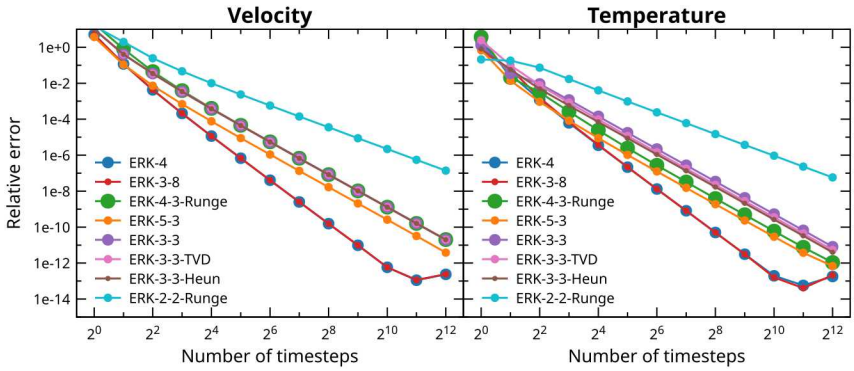

(b) Explicit methods.

Figure 5-8. Convergence results for two-fluid relaxation problem.

(iii) A collisional three-fluid system containing ion, electron, and neutral species with constant friction coefficients $\alpha_{e;i} = 1.0\text{E}{+}18$ and $\alpha_{n;e} = \alpha_{n;i} = 2.0\text{E}{+}17$. The result is again a damped oscillation.

(iv) A collisional three-fluid system containing ion, electron, and neutral species with friction coefficients computed using (22) and (25). The result is a damped oscillation in which the oscillation frequency is much smaller than the timescale over which collisional relaxation occurs.

If the friction coefficients $\alpha_{s;t}$ are assumed to be constant, analytic solutions may be derived for the two-fluid case with the additional assumption of charge-neutrality; ie., we assume that $n_i = n_e$ in this case. The velocity difference between the charged species is given by

$$\mathbf{u}_e(t) - \mathbf{u}_i(t) = \left(\mathbf{u}_e(t_0) - \mathbf{u}_i(t_0)\right) \exp\left(-\frac{\nu_{e;i}\, t}{2}\right) \frac{\cos\left(\eta_{e;i}\, t - \phi_{e;i}\right)}{\cos\phi_{e;i}}, \tag{125}$$

where

$$\nu_{e;i} = \alpha_{e;i}\left(\rho_e + \rho_i\right), \qquad \omega_{e;i}^2 = \frac{q_e^2}{\epsilon_0} n_i \left(\frac{1}{m_e} + \frac{1}{m_i}\right), \tag{126a}$$

$$\eta_{e;i}^2 = \omega_{e;i}^2 - \frac{\nu_{e;i}^2}{4}, \qquad \phi_{e;i} = \tan^{-1}\left(-\frac{\nu_{e;i}}{2\eta_{e;i}}\right). \tag{126b}$$

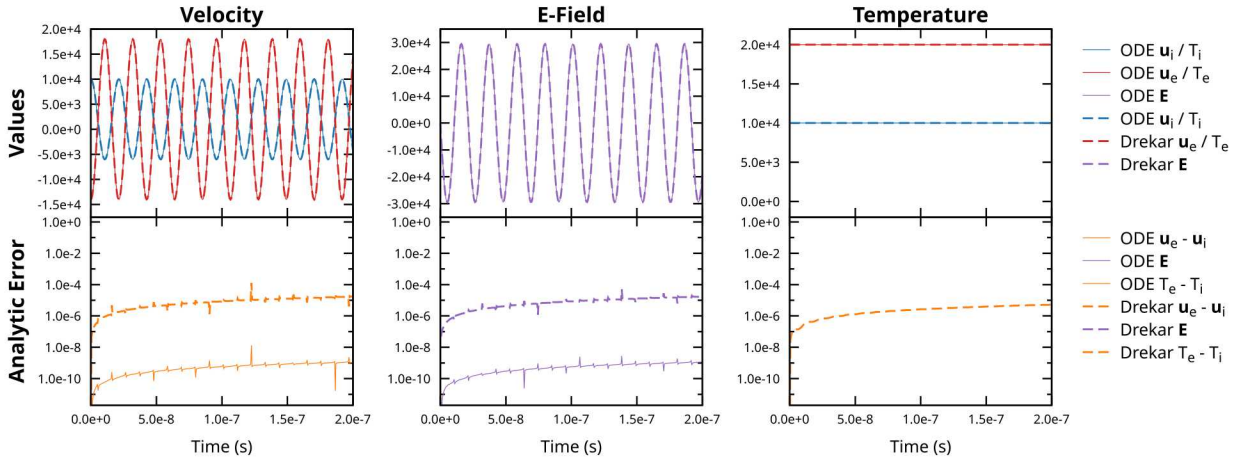

(a) Two-fluid collisionless oscillation.

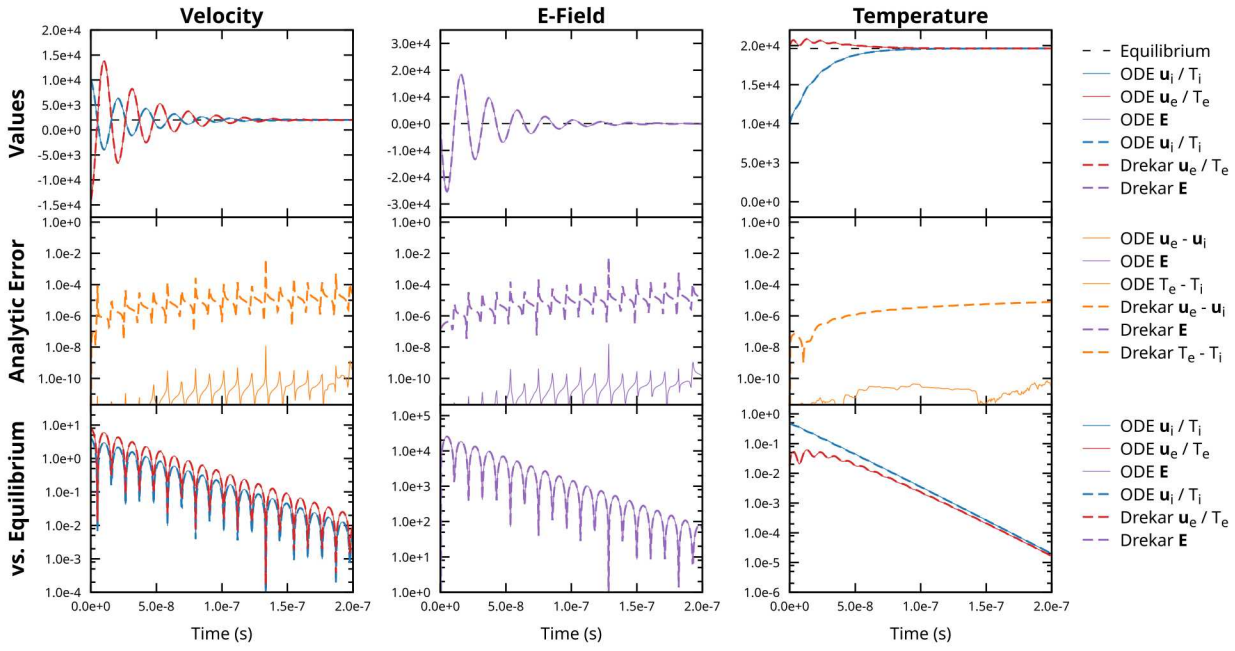

(b) Two-fluid damped oscillation.

Figure 5-9. Results for two-fluid collisional and collisionless plasma oscillations.

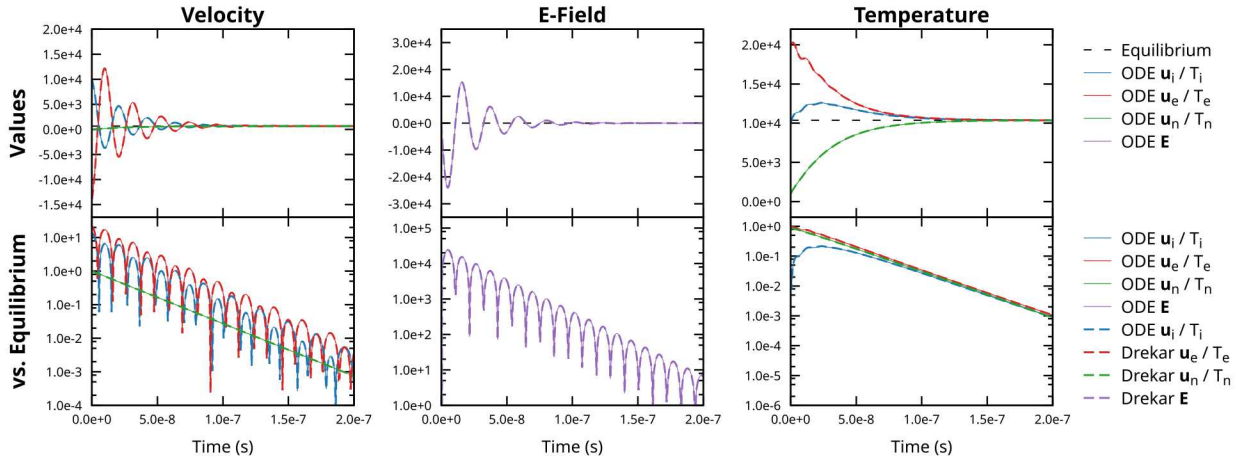

(a) Three-fluid damped oscillation with constant friction coefficients.

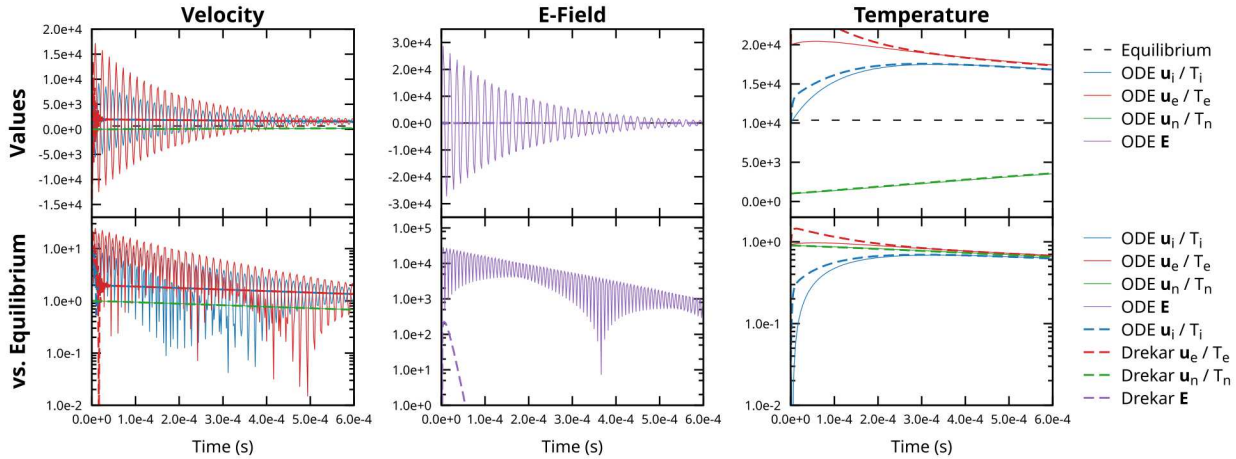

(b) Three-fluid damped oscillation with friction coefficients computed using (22) and (25).

Figure 5-10. Results for three-fluid collisional plasma oscillations.

The electric field $\mathbf{E}$, which is initially zero, is given by

$$\begin{aligned}\mathbf{E}(t) = -\left(\mathbf{u}_e(t_0) - \mathbf{u}_i(t_0)\right)\frac{q_e n_i}{\epsilon_0}\frac{\exp\left(-\nu_{e;i}\,t/2\right)}{\omega_{e;i}^2\cos\phi_{e;i}}\Big[\eta_{e;i}\sin\left(\eta_{e;i}\,t-\phi_{e;i}\right)\\ -\frac{\nu_{e;i}}{2}\cos\left(\eta_{e;i}\,t-\phi_{e;i}\right)+\exp\left(\nu_{e;i}\,t/2\right)\left(\frac{\nu_{e;i}}{2}\cos\phi_{e;i}+\eta_{e;i}\sin\phi_{e;i}\right)\Big].\end{aligned} \tag{127}$$

The temperature difference between the charge species is given by

$$\begin{aligned}T_e(t) - T_i(t) = \exp\left(-A_{e;i}\,t\right)C_{e;i} + \frac{D_{e;i}\exp\left(-\nu_{e;i}\,t\right)}{\cos^2\phi_{e;i}}\Big[4\eta_{e;i}^2 + 2G_{e;i}^2\cos^2\left(\eta_{e;i}\,t-\phi_{e;i}\right)\\ +4\eta_{e;i}G_{e;i}\sin\left(\eta_{e;i}\,t-\phi_{e;i}\right)\cos\left(\eta_{e;i}\,t-\phi_{e;i}\right)\Big],\end{aligned} \tag{128}$$

where

$$A_{e;i} = 2\alpha_{e;i}\frac{m_e m_i}{m_e+m_i}\left(n_e+n_i\right), \tag{129a}$$

$$B_{e;i} = \frac{\gamma-1}{k_\mathrm{B}}\alpha_{e;i}\left(\rho_i-\rho_e\right)\frac{m_e m_i}{m_e+m_i}\left(\mathbf{u}_e(t_0)-\mathbf{u}_i(t_0)\right)^2, \tag{129b}$$

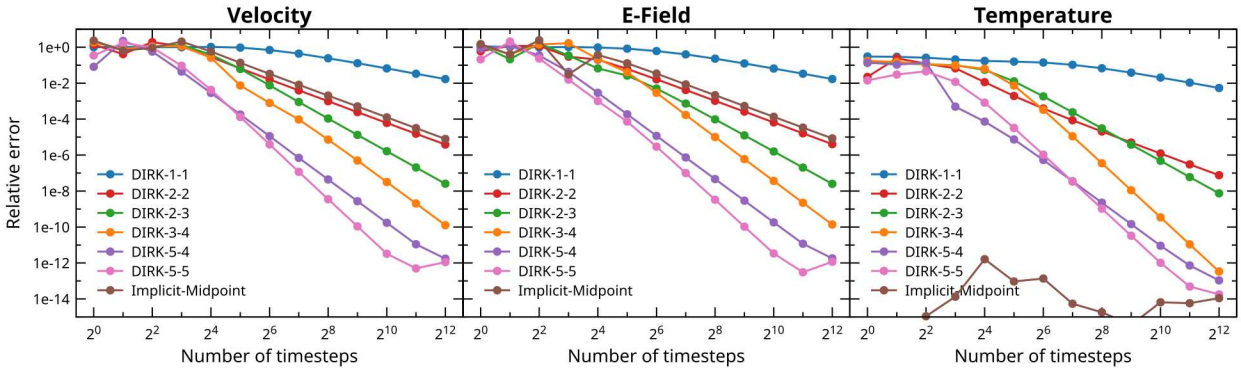

(a) Implicit methods (Tempus).

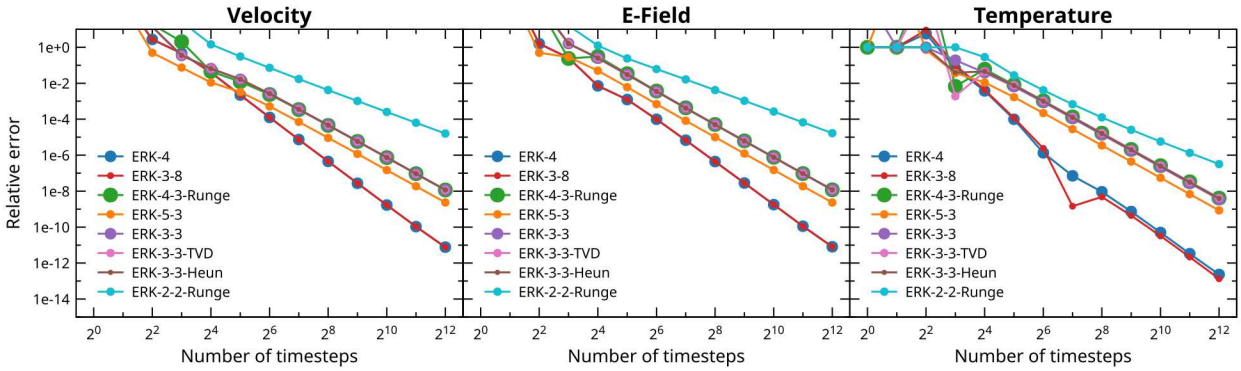

(b) Explicit methods (Tempus).

Figure 5-11. Convergence tests for two-fluid collisionless oscillation.

$$C_{e;i} = \left(T_e\left(t_0\right) - T_i\left(t_0\right)\right) - D_{e;i}\left[\frac{4\eta_{e;i}^2}{\cos^2\phi_{e;i}} + 2G_{e;i}\left(G_{e;i} - 2\eta_{e;i}\tan\phi_{e;i}\right)\right], \tag{129c}$$

$$D_{e;i} = \frac{B_{e;i}}{2G_{e;i}\left(4\eta_{e;i}^2 + G_{e;i}^2\right)}, \tag{129d}$$

$$G_{e;i} = A_{e;i} - \nu_{e;i}. \tag{129e}$$

The time evolution of numerically computed velocity and temperature values from Drekar and an explicit ODE solver are compared in Figures 5-9 and 5-10. For the two-fluid cases Figure 5-9, each solver is additionally compared to the analytic solutions (125), (127) and (128). For the cases with constant or zero friction coefficients, we observe that: (i) the numerical implementations are in very good agreement, (ii) each numerical implementation relaxes toward the appropriate equilibrium values, and (iii) both numerical implementations yield small errors relative to the analytic two-fluid solutions. The results of convergence studies for the two-fluid scenarios using various implicit and explicit time-integration schemes made available through the Tempus library are shown in Figures 5-11 and 5-12 for a simulation time of $t = 4.0\text{E}{-8}$.

In the case of the three-fluid damped oscillation with friction coefficients computed using (22) and (25), the oscillation frequency is much larger than the timescale over which collisional relaxation occurs. For this problem, the ODE solution is computed using an explicit embedded method that resolves the fast timescale associated with the oscillation frequency. Meanwhile, the Drekar solution is computed using an L-stable implicit method using a timestep size that is much larger than that required to resolve the oscillation frequency. In Figure 5-10(b), the effect of the implicit method used in the Drekar calculation is clear: the oscillation

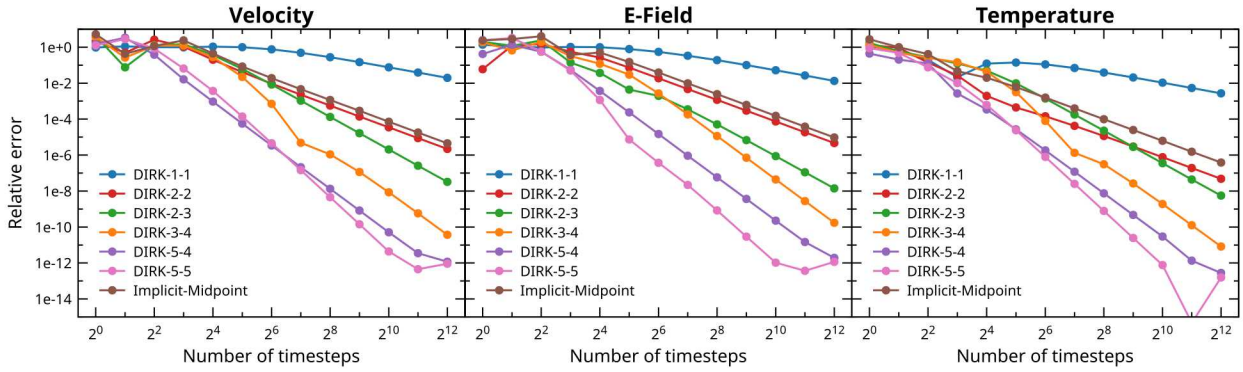

(a) Implicit methods (Tempus).

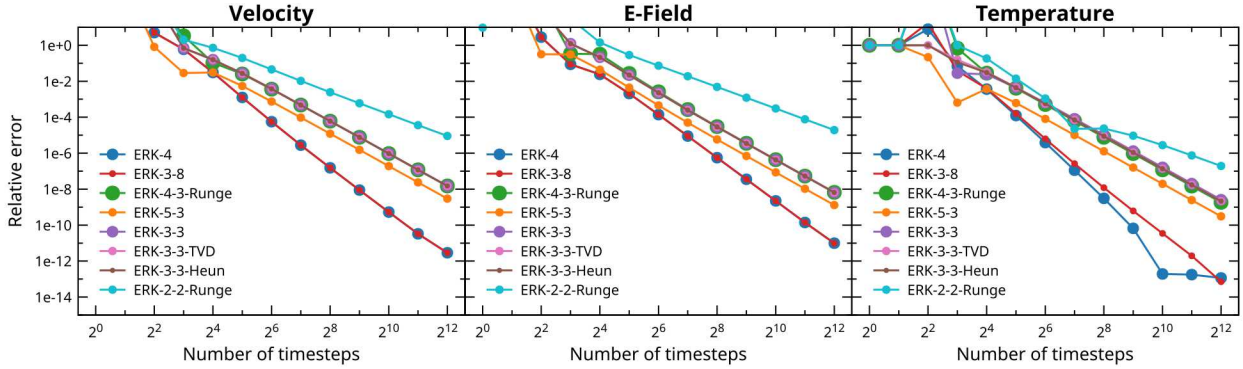

(b) Explicit methods (Tempus).

Figure 5-12. Convergence tests for two-fluid damped oscillation.

is not resolved, but the solution is appropriately damped in a manner that is consistent with the long-time collisional relaxation of the ODE solution.

5.3. Verification and Evaluation of Ionization/recombination Processes

Verification of the ionization and recombination rate implementation in Drekar is performed by comparing the average charge state values generated by: (i) directly computing the equilibrium ionization fractions for a reduced ODE model, and (ii) integrating the reaction system in time using Drekar to a large final time. Here only ionization and recombination source terms are included in (110), and the contributions due to electric and magnetic fields are assumed to be zero. To prevent the ionization and recombination rates from changing as energy is transferred between species, this test does not use an energy equation for each species: Instead, the temperature of all species is set to the same constant value.

Each test contains an electron species and all charge states of one atomic species, with a total ion number density of $1.0\text{E}{+}24\ \text{m}^{-3}$. The ionization fractions for each charge state are initially equal (ie., a uniform distribution across the charge states is used). In order to ensure that the reactions progress reasonably quickly even in the low-temperature limit (where the average charge state would be near zero) we do not assume quasi-neutrality: instead, initial electron number density is increased by $1.0\text{E}{+}24\ \text{m}^{-3}$ beyond the quasi-neutral density value. That is, the initial electron number density is given by

$$(1.0\text{E}{+}24)\left(1+\overline{Z}_0\right), \tag{130}$$

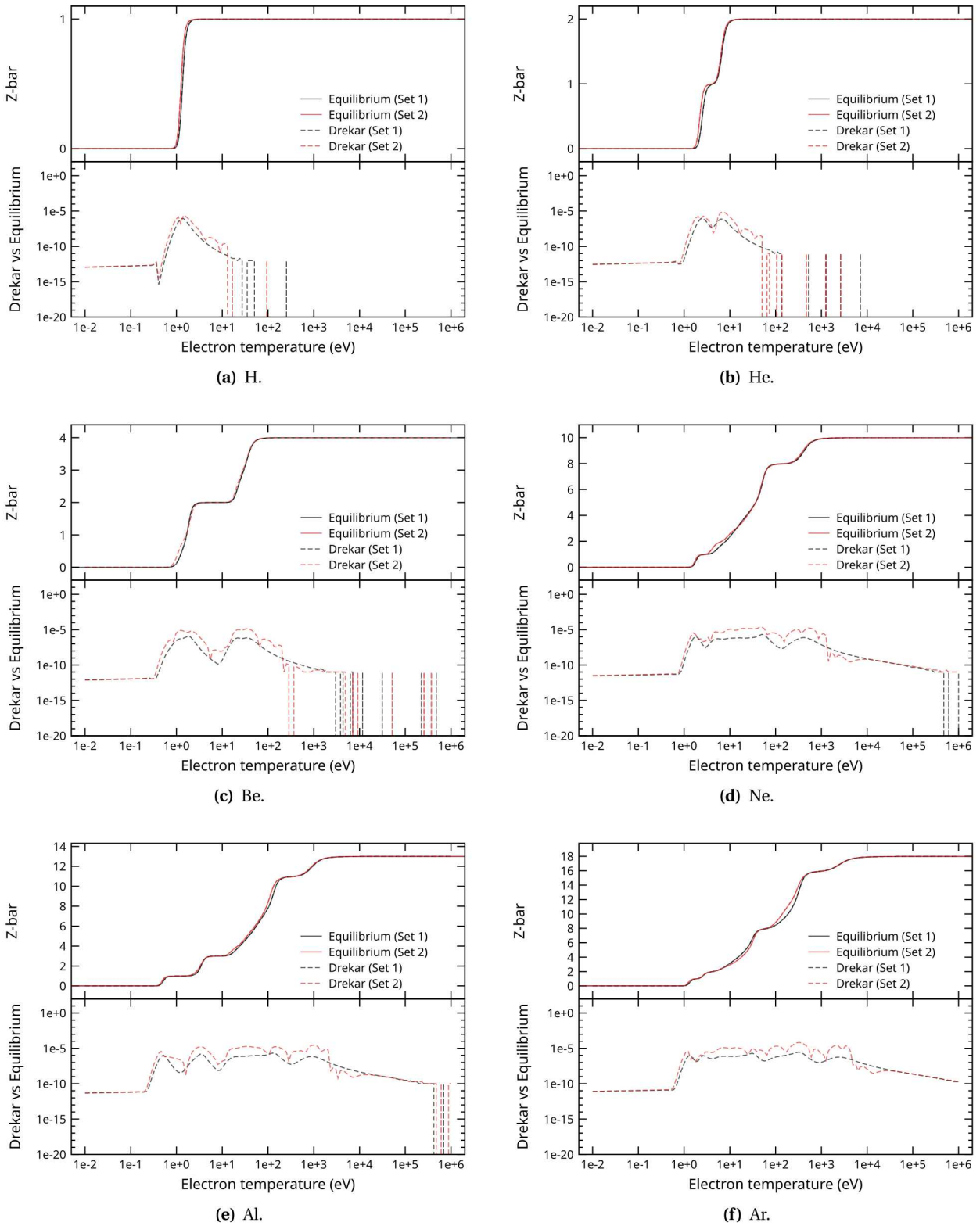

(a) H. **(b)** He. **(c)** Be. **(d)** Ne. **(e)** Al. **(f)** Ar.

Figure 5-13. Results of verification tests for ionization/recombination.

where $\overline{Z}_0$ is the initial average ion charge state.

The equilibrium ionization fractions are computed as follows. Let

$$f_{(\alpha,k)} \stackrel{\text{def}}{=} \frac{n_{(\alpha,k)}}{\sum_\ell n_{(\alpha,\ell)}}, \qquad (k = 1,\ldots,z_\alpha), \tag{131}$$

denote the ionization fractions of the charge states of species α. The ionization fractions of two successive charge states are related by

$$\frac{f_{(\alpha,k+1)}}{f_{(\alpha,k)}} = \frac{I_{(\alpha,k)}}{R_{(\alpha,k+1)}}, \qquad (k = 1,\ldots,z_\alpha - 1). \tag{132}$$

Combining the relations (132) with the additional constraint

$$\sum_{k=1}^{z_\alpha} f_{(\alpha,k)} = 1 \tag{133}$$

yields a linear system for the values of the equilibrium ionization fractions, which can be written as

$$\begin{pmatrix} 1 & 1 & 1 & \cdots & 1 \\ -I_{(\alpha,1)} & R_{(\alpha,2)} & & & \\ & -I_{(\alpha,2)} & R_{(\alpha,3)} & & \\ & & \ddots & \ddots & \\ & & & -I_{(\alpha,z_\alpha-1)} & R_{(\alpha,z_\alpha)} \end{pmatrix} \begin{pmatrix} f_{(\alpha,1)} \\ f_{(\alpha,2)} \\ f_{(\alpha,3)} \\ \vdots \\ f_{(\alpha,z_\alpha)} \end{pmatrix} = \begin{pmatrix} 1 \\ 0 \\ 0 \\ \vdots \\ 0 \end{pmatrix}. \tag{134}$$

Once the system (134) is solved, the ionization fractions obtained can be used to compute required quantities such as the average ion charge state $\overline{Z}_{(\alpha,i)}$.

The Drekar runs are integrated to a final time of $t = 1.0\text{E}{-4}$ using the implicit Euler scheme. Note that the final time is chosen large enough that each configuration should reach a state that is close to the equilibrium value by the end of the simulation. The results of the tests for a selection of species of interest over a broad range of temperatures are shown in Figure 5-13. The agreement between the exact equilibrium values and the time-evolved values is very good in each case.

5.4. Solution of the Multffluid EM Plasma Model in the Asymptotic Resistive MHD Limit

In the context of developing a robust and accurate multifluid model and set of associated computational solution methods for these complex systems an important necessary condition to apply the model to a large range of potential plasma physics applications is to demonstrate that the model can be solved when component length and time-scale are coarsely, and even unresolved, in the simulation. That is for this complex multiple-time-scale system broad application of the computational model requires the ability, when appropriate, to overstep in a stable manner, time-scales such as transverse EM waves, collisions, cyclotron and plasma frequencies, diffusion time scales and still resolve accurately slower dynamics such as hydrodynamics, Alfven and magnetosonic wave propagation. In this context fully-implicit and IMEX methods have shown considerable progress [89]. Additionally since electron dynamics can often be orders of magnitude faster than ion time-scales the ability to differentially handle not only componnet mechanisms but also electron dynamics implicitly is also a significant advantage in developing a computationally tractable computational formulation for the multifluid EM plasma model. in the brief section that follows we describe some initial results of applying IMEX methods and solving the multifluid EM model in the asymptotic limits of visco-resistive and ideal MHD. For a more detailed and self contained discussion of these topics please see [89].

5.4.1. Visco-resistive Alfven wave propagation

While linear waves are good for testing linear terms, they do not stress resistive, viscous, or convective terms. The visco-resistive Alfven wave problem is classically used to test resistive MHD models [91] and the multifluid development is detailed in [89]. The problem uses a magnetized viscous boundary layer, known as a Hartmann layer, to generate an Alfven wave which propagates into an infinite domain. Application of a multi-fluid plasma model to the problem is difficult due to consistency issues discussed herein. Figure 5-14 outlines the problem geometry, where the Alfven wave is propagated along an imposed magnetic field creating a shear flow profile.

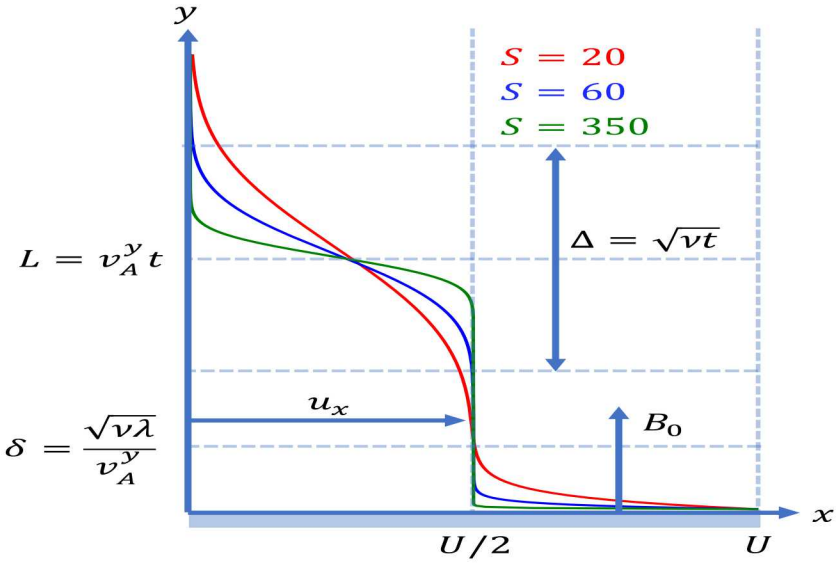

Figure 5-14. Example profiles for shear velocity u_x for Alfven wave problem showing the effect of increasing the effective Lundquist number S. Length scales include the Hartmann layer thickness δ, diffusion thickness Δ, and Alfven wave propagation distance L.

For MHD, the problem derivation can be found in [91], however, adaptation to the two-fluid model requires additional constraints to support the MHD asymptotic limit. The solution is derived from incompressible, resistive-viscous MHD in a slab geometry where $\partial_x \cdot = \partial_z \cdot = 0$. The density and pressure are assumed constant. The problem defines sheared flow along the $\hat{y}$ axis, which leads to two sets of equations

$$\partial_t u_x = v_y^A \partial_y v_A^x + \nu \partial_y^2 u_x \tag{135}$$

$$\partial_t v_x^A = v_y^A \partial_y u_x + \lambda \partial_y^2 v_x^A \tag{136}$$

and

$$\partial_t u_z = v_y^A \partial_y v_z^A + \nu \partial_y^2 u_z \tag{137}$$

$$\partial_t v_z^A = v_y^A \partial_y u_z + \lambda \partial_y^2 v_z^A, \tag{138}$$

describing the evolution of the shear flows u_x and u_z, and the Alfven velocity

$$v_i^A = \frac{B_i}{\sqrt{\mu_0 \rho}} \tag{139}$$

in terms of the kinematic viscosity $\nu = \mu/\rho$ and magnetic diffusivity $\lambda = \eta/\mu_0$, where the resistivity is given by

$$\eta = \frac{m_e \nu_{ei}}{n_e e^2}. \tag{140}$$

For this analysis, the focus will be on a flow along $\hat{x}$, represented by Eqs. (135) and (136).

From [91], the solution for this system is found when $\lambda = \nu = D$. Given a wall velocity of U the solution takes the form

$$u_x = \frac{U}{4}\left(\text{erfc}(\eta_+)\left(1+\exp\left(\frac{y}{Y}\right)\right)+\text{erfc}(\eta_-)\left(1+\exp\left(-\frac{y}{Y}\right)\right)\right) \tag{141}$$

$$v_x^A = \frac{U}{4}\left(\text{erfc}(\eta_+)\left(1-\exp\left(\frac{y}{Y}\right)\right)-\text{erfc}(\eta_-)\left(1-\exp\left(-\frac{y}{Y}\right)\right)\right) \tag{142}$$

where the normalized coordinate

$$\eta_\pm = \frac{\frac{y}{Y} \pm \frac{t}{\tau}}{2\sqrt{\frac{t}{\tau}}} \tag{143}$$

is defined by a length scale

$$Y = \frac{\lambda}{v_y^A} \tag{144}$$

and time scale

$$\tau = \frac{Y}{v_y^A}. \tag{145}$$

The simulation time for this problem is defined by an effective Lundquist number at a point in time $t = T$. The Alfven wave generated in this problem propagates a length $L = v_A T$, which can be used in the definition of the effective Lundquist number,

$$S = \frac{L v_y^A}{\lambda} = \frac{L}{Y} = \frac{T}{\tau}, \tag{146}$$

to give a relationship between simulation time and domain size. Figure 5-14 shows the effect of increasing Lundquist number on the solution profile. Note that while the wavefront remains diffused for the given examples, the Hartmann layer thickness decreases dramatically. This leads to an issue when using the multi-fluid plasma model where the Hartmann layer must be resolved to converge to the proper shear velocity profile. In practice the mesh is biased to increase the number of cells in the Hartmann layer.

Additionally, it is important to remember that this problem is derived from resistive MHD, and, therefore, ignores Hall physics. To keep the multi-fluid plasma model consistent with this, the plasma regime must be chosen such that the Hall parameter

$$H = \frac{\omega_{ce}}{\nu_{ei}} \ll 1. \tag{147}$$

This regime is easier to define by rewriting the Hall parameter as

$$H = \frac{d_i}{Y}, \tag{148}$$

with ion skin depth d_i, which gives a method for choosing a plasma density consistent with a small Hall parameter for a given viscosity and magnetic field.

Since the commonly applied bulk-viscosity, Navier-Stokes style operators employed for resistive MHD models are only consistent with multi-fluid in the asymptotic sense, an approximation is used to keep the models in agreement. Namely, that the bulk viscosity is the sum of electron and ion viscosities

$$\mu = \mu_e + \mu_i. \tag{149}$$

This approximation supports the asymptotic relation since the electron and ion shear velocities are equal along $\hat{x}$ due to the large resistivity driving $j_x \to 0$. In the literature [24, 50], viscosity scales with

$$\mu_\alpha \propto \frac{P_\alpha}{\nu_{\alpha\alpha}} \tag{150}$$

and intraspecies collisions scale with

$$\frac{\nu_{ee}}{\nu_{ii}} \approx \sqrt{\frac{m_i}{m_e}} \tag{151}$$

which combine to give

$$\mu_i = \sqrt{\frac{m_e}{m_i}}\mu_e \tag{152}$$

where

$$\mu_e = \nu(\rho_e + \rho_i)\frac{1}{1+\sqrt{\frac{m_e}{m_i}}}. \tag{153}$$

A similar relationship can be derived for the thermal conductivities.

The problem's parameter regime is controlled by setting ratios between characteristic variables in the system. The Hall parameter is chosen at $H = 10^{-4}$. The plasma is a hydrogen plasma with $m_i = 1836 m_e$, the Alfven velocity is $v_A^y = 10^{-3}c$, the wall velocity is $u_0 = 10^{-3}v_A^y$. The ion sound speed is $v_{si} = 10^{-3}v_A^y$. The adiabatic index is $\gamma = 5/3$. The domain length is set at $L_y = 3L$ to fit the entire Alfven wave with its diffusive tails, while the mesh itself is biased to increase the number of cells at the moving boundary. Boundary conditions set the shear wall velocity $u_x^\alpha = U$, and the inbound flow to $u_y^\alpha = 0$. The boundary conditions for the electromagnetics, density, energy, and orthogonal velocity u_z^α are zero Neumann conditions.

The physical parameter regime can be normalized, and, for this application, the speed of light is set to $c = 10^3$, permeability is $\mu_0 = 1$, and elementary charge $e = 1$. Figure 5-15 shows convergence results for three effective Lundquist numbers. Table 5-3 shows the time scales for this problem. The collision frequency, plasma frequency, and cyclotron frequencies are all integrated far outside of their explicit stability limits. Since the diffusion numbers are resolved, the model is effectively being integrated over MHD time scales.

5.4.2. Plasma vortex (Z-pinch) advection

The two-fluid plasma vortex problem describes the advection of a smooth z-pinch within a plane. This problem is an extension of the ideal MHD vortex problem introduced in [13], and is depicted in Fig. 5-16. Naturally, the two-fluid solution must be consistent with the MHD solution.

The vortex problem is designed to test the ability for the discretization to advect a plasma equilibrium. The plasma is assumed to be quasi-neutral such that

$$\rho = m_e n_e + m_i n_i = m_i \frac{n}{Z_i}(1+R) \tag{154}$$

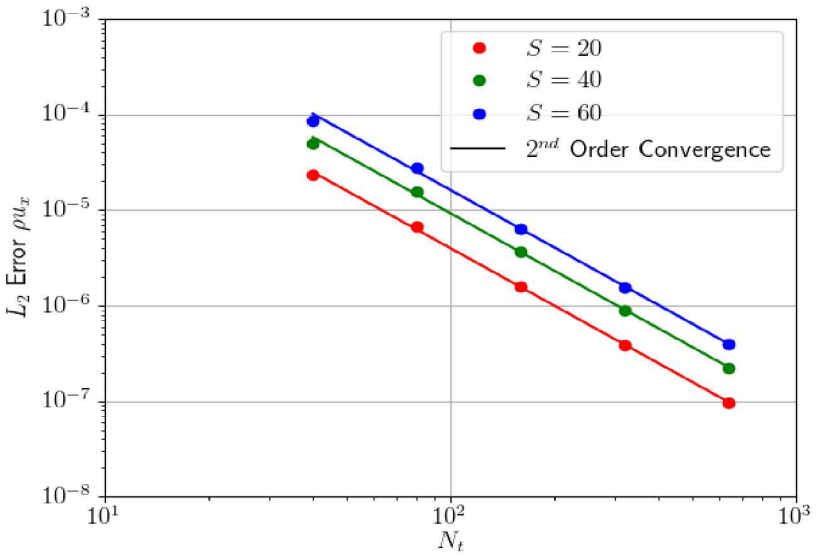

Figure 5-15. Alfven wave results for three effective Lundquist numbers S. Results show the expected 2^{nd} order convergence. Mesh resolution ranges from 20 to 320 cells across the shear flow, however the mesh has a linearly biased resolution which increases near the boundary layer and decreases near the open boundary.

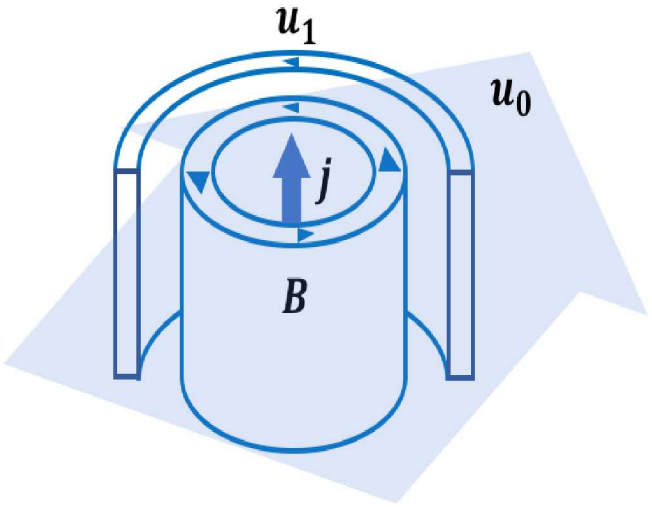

Figure 5-16. Orientations of fields in vortex problem. A pressure gradient balances the magnetic $\mathbf{j} \times \mathbf{B}$ forces and the cetripital forces due to the rotating flow. The entire vortex is advected diagonally in the 2D domain at velocity u_0.

where $n_e = n$, $n_i = n/Z_i$, and

$$R = Z_i \frac{m_e}{m_i}. \tag{155}$$

Table 5-3. Time scales for effective Lundquist number $S = 60$. Frequency and diffusive time scales are expressed as a range since convergence is tested over a constant CFL $\Delta t \propto \Delta x$. Operators associated with bold terms are treated implicitly.

	Electrons	Ions
$\omega_p \Delta t$	$\mathbf{4 \cdot 10^7}$ - $\mathbf{1.3 \cdot 10^9}$	$\mathbf{9.4 \cdot 10^5}$ - $\mathbf{3 \cdot 10^7}$
$\omega_c \Delta t$	$\mathbf{1.7 \cdot 10^6}$ - $\mathbf{5.5 \cdot 10^7}$	$\mathbf{9.4 \cdot 10^2}$ - $\mathbf{3 \cdot 10^4}$
$\nu_{\alpha\beta} \Delta t$	$\mathbf{1.7 \cdot 10^{10}}$ - $\mathbf{5.5 \cdot 10^{11}}$	$\mathbf{9.4 \cdot 10^6}$ - $\mathbf{3 \cdot 10^8}$
$v_s \frac{\Delta t}{\Delta x}$	$7 \cdot 10^{-3}$	$2 \cdot 10^{-4}$
$\frac{\mu}{\rho} \frac{\Delta t}{\Delta x^2}$	**0.4 - 12**	**0.01 - 0.3**
$c \frac{\Delta t}{\Delta x}$	**167**	

The magnetic field for the vortex is defined within the $(\hat{x}, \hat{y})$ plane

$$\mathbf{B} = \begin{bmatrix} -B_0 r_y \exp\left(\frac{1-r^2}{2}\right) \\ B_0 r_x \exp\left(\frac{1-r^2}{2}\right) \\ 0 \end{bmatrix} \tag{156}$$

where $r = |\mathbf{r}|$ with shifted radial vector

$$\mathbf{r} = \begin{bmatrix} \frac{x-u_0 t}{L} \\ \frac{y-u_0 t}{L} \\ 0 \end{bmatrix}. \tag{157}$$

The length scale L defines the shell width of the vortex, and u_0 is the convection velocity. The current required to support this magnetic field is then

$$\mathbf{j} = \begin{bmatrix} \frac{q_e}{m_e}\rho_e u_x^e + \frac{q_i}{m_i}\rho_i u_x^i \\ \frac{q_e}{m_e}\rho_e u_y^e + \frac{q_i}{m_i}\rho_i u_y^i \\ \frac{q_e}{m_e}\rho_e u_z^e + \frac{q_i}{m_i}\rho_i u_z^i \end{bmatrix} = \frac{1}{\mu_0}\nabla \times \mathbf{B} = \begin{bmatrix} 0 \\ 0 \\ \frac{B_0}{\mu_0 L}(2 - r^2)\exp\left(\frac{1-r^2}{2}\right) \end{bmatrix}. \tag{158}$$

The problem also defines the bulk flow velocity

$$\mathbf{u} = \begin{bmatrix} \frac{\rho_e u_x^e + \rho_i u_x^i}{\rho_e + \rho_i} \\ \frac{\rho_e u_y^e + \rho_i u_y^i}{\rho_e + \rho_i} \\ \frac{\rho_e u_z^e + \rho_i u_z^i}{\rho_e + \rho_i} \end{bmatrix} = \begin{bmatrix} u_0 - u_1 r_y \exp\left(\frac{1-r^2}{2}\right) \\ u_0 + u_1 r_x \exp\left(\frac{1-r^2}{2}\right) \\ 0 \end{bmatrix}, \tag{159}$$

where u_1 is the vorticial flow velocity. The bulk velocity and current density combine to give the velocities for the ions

$$\mathbf{u}_i = \begin{bmatrix} u_0 - u_1 r_y \exp\left(\frac{1-r^2}{2}\right) \\ u_0 + u_1 r_x \exp\left(\frac{1-r^2}{2}\right) \\ \frac{R}{1+R}\frac{B_0}{\mu_0 Len}(2 - r^2)\exp\left(\frac{1-r^2}{2}\right) \end{bmatrix} \tag{160}$$

and electrons

$$\mathbf{u}_e = \begin{bmatrix} u_0 - u_1 r_y \exp\left(\frac{1-r^2}{2}\right) \\ u_0 + u_1 r_x \exp\left(\frac{1-r^2}{2}\right) \\ -\frac{1}{1+R}\frac{B_0}{\mu_0 Len}(2 - r^2)\exp\left(\frac{1-r^2}{2}\right) \end{bmatrix}. \tag{161}$$

The pressure gradient separately balances rotational forces,

$$P_u = -\frac{1}{2}\rho u_1^2 \exp\left(\frac{1-r^2}{2}\right), \tag{162}$$

and magnetic forces,

$$P_m = \frac{B_0^2}{2\mu_0}\left(1-r^2\right)\exp\left(\frac{1-r^2}{2}\right). \tag{163}$$

The pressures are decomposed between the electrons,

$$P_e = \frac{1}{2}P_0 + \frac{R}{1+R}P_u + \frac{1}{1+R}P_m, \tag{164}$$

and ions

$$P_i = \frac{1}{2}P_0 + \frac{1}{1+R}P_u + \frac{R}{1+R}P_m \tag{165}$$

such that the total pressure $P = P_e + P_i$ is consistent with the ideal MHD form from [13].

The ideal MHD formulation also defines a time dependent electric field to satisfy Ampere's law

$$\mathbf{E} = \begin{bmatrix} 0 \\ 0 \\ -B_0 u_0 (r_x + r_y)\exp\left(\frac{1-r^2}{2}\right) \end{bmatrix}. \tag{166}$$

Similar to the Alfvén wave problem, the two-fluid vortex is only valid in the asymptotic limit of MHD. Since the multi-fluid formulation includes a displacement current in Ampere's law, there is a growing deviation from equilibrium which scales as

$$\frac{\epsilon_0 \partial_t E_z}{j_z} \propto \frac{u_0^2}{c^2} \tag{167}$$

which restricts the applicability to slow advection velocities. In the asymptotic limit of ideal MHD this is naturally satisfied, however for the multi-fluid model this must be directly enforced.

The problem is defined independent from the mass ratio, and, therefore, the problem is tested at three mass ratios $m_i/m_e \in (10, 100, 1836)$. The ions are singly charged. Problem is setup with $u_0 = 1$, $u_1 = B_0 = \frac{1}{2\pi}$, $P_0 = 1$, $n = 1$, and $L = 1$ on a 2D domain $x \in (-5, 5)$ and $y \in (-5, 5)$. The parameters are chosen in a normalized parameter regime where $m_i = 1$, $\mu_0 = 1$ and $c = 1000$.

The results are shown in Fig. 5-17 which shows 2^{nd} order convergence. The time scales for this problem, given in Table 5-4, show that while the electrostatics and electromagnetics are being stepped over by a large factor, the simulation still converges properly.

6. DEMONSTRATION ON COMPLEX PLASMA PROBLEMS: MHD AND MULTIFLUID EM PLASMA RELATED TO MIF

6.1. High Density Single Shell Liner MHD Implosions (Ideal Gas)

This simple example, proof-of-principle computation, is a demonstration of a resistive MHD implosion for a high density gas cylinder. A simple analytic ideal gas equation of state is used and a Knopfel electrical

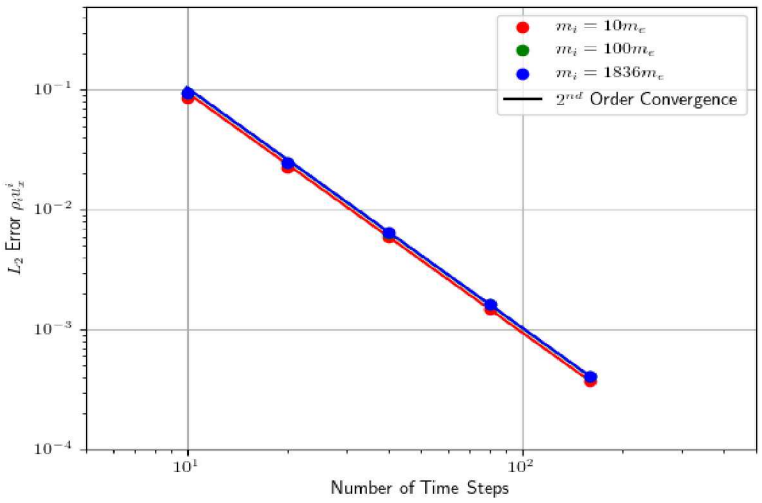

Figure 5-17. Two-fluid vortex momentum convergence has expected 2^{nd} order convergence for the three mass ratios tested at an end time of $t = 0.1$. Convergence is tested at a constant CFL such that $\Delta t \propto \Delta x = \Delta y$. Mesh resolution ranges from $8x8$ to $128x128$ cells across the domain.

conductivity model. These representations are clearly non-physical for the entire range of parameters of the implosion problem but this initial study is included as a proof of principle that the resistive MHD model, the stabilization of the hyperbolic systems, and the iterative solution of the linear systems work for this class of reasonably complex plasma problems. The boundary conditions are Neumann type zero flux conditions on the density, and momentum, with the **B** field specified in the flux boundary condition for total energy and a Dirichlet condition on By. The time profile for By is given by an analytic profile for $q = 6$ [14] for which the implosion time is set at 100 ns, and is shown graphically in Figure 6-1. The initial conditions is for a constant pressure high density gas (see image for the initial condition) has a maximum initial density of 10^3 and a minimum initial density of $10^{-4} kg/m^3$. In Figure 6-2 the evolution of the implosion for the profiles of density and By is shown. In this case the AFC stabilization is demonstrated for the resistive MHD system. The image progression shows the liner imploding as the **B** field increases and then the rebound/relaxation of the liner as the By field is decreased. At this point the evolution of the liner appears plausible, however future more comprehensive studies, and comparisons with experiments for more realistic conditions, are

Table 5-4. Time scales for mass ratio of $m_i = 1836m_e$. Frequency and diffusive time scales are expressed as a range since convergence is tested over a constant CFL $\Delta t \propto \Delta x$. Operators associated with bold terms are treated implicitly.

	Electrons	Ions
$\omega_p \Delta t$	**23 - 270**	**0.55 - 6.3**
$\omega_c \Delta t$	**1 - 12**	$\mathbf{5.5 \cdot 10^{-4}}$ **- 6.3** $\cdot \mathbf{10^{-3}}$
$v_s \frac{\Delta t}{\Delta x}$	0.25	$5.7 \cdot 10^{-3}$
$c \frac{\Delta t}{\Delta x}$		**6.3**

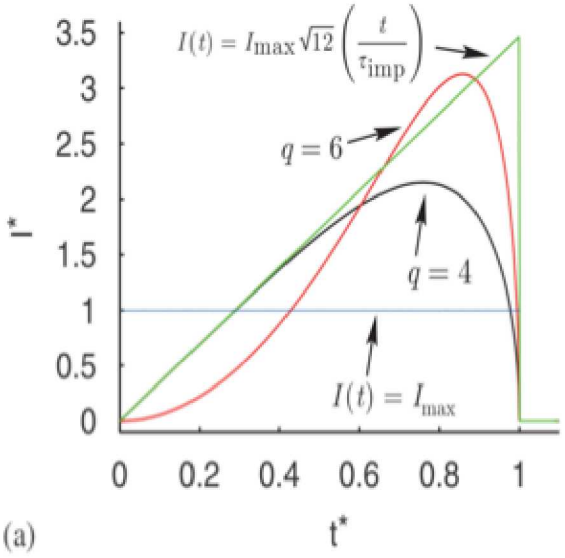

Figure 6-1. Non-dimensional time history profile used for specifications of boundary conditions (By in this case) [14].

required for evaluation of the formulation. Even with these limitations these initial results are encouraging. The compressible resistive MHD system is integrated at a maximum time step of about 5×10^{-10} seconds with an implicit SDIRK22 L-stable method and the simulation progresses through the maximum compression and the rebound phase.

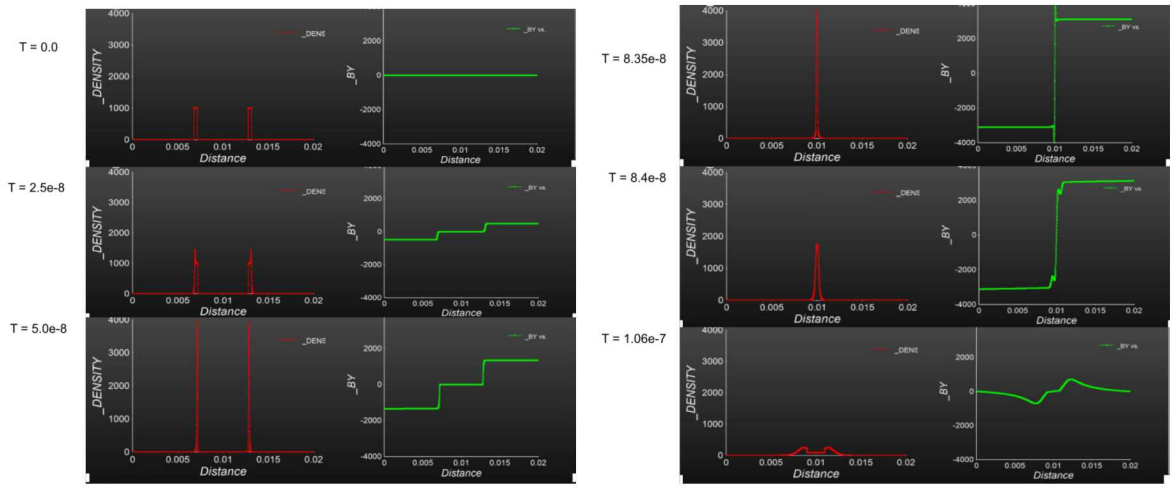

(a) Density and By during compression

(b) Density and By close to peak compression and rebound

Figure 6-2. Density and By for single shell high density one-dimensional MHD Z-pinch.

We also include below both a 2D and 3D version of the high density gas liner MHD implosion. It generalizes the same initial conditions as the 1D to multiD and then applies the $q = 6$ boundary drive for B_θ. In this case developing a peak of roughly 60MA. Representative results are presented in Figure 6-3 and Figure 6-4. For the 3D case constant surfaces of density are visualized with the mesh also represented. Clearly evident is the

more unstable, non axis-symmetric constant density surfaces as the gas shell implodes.

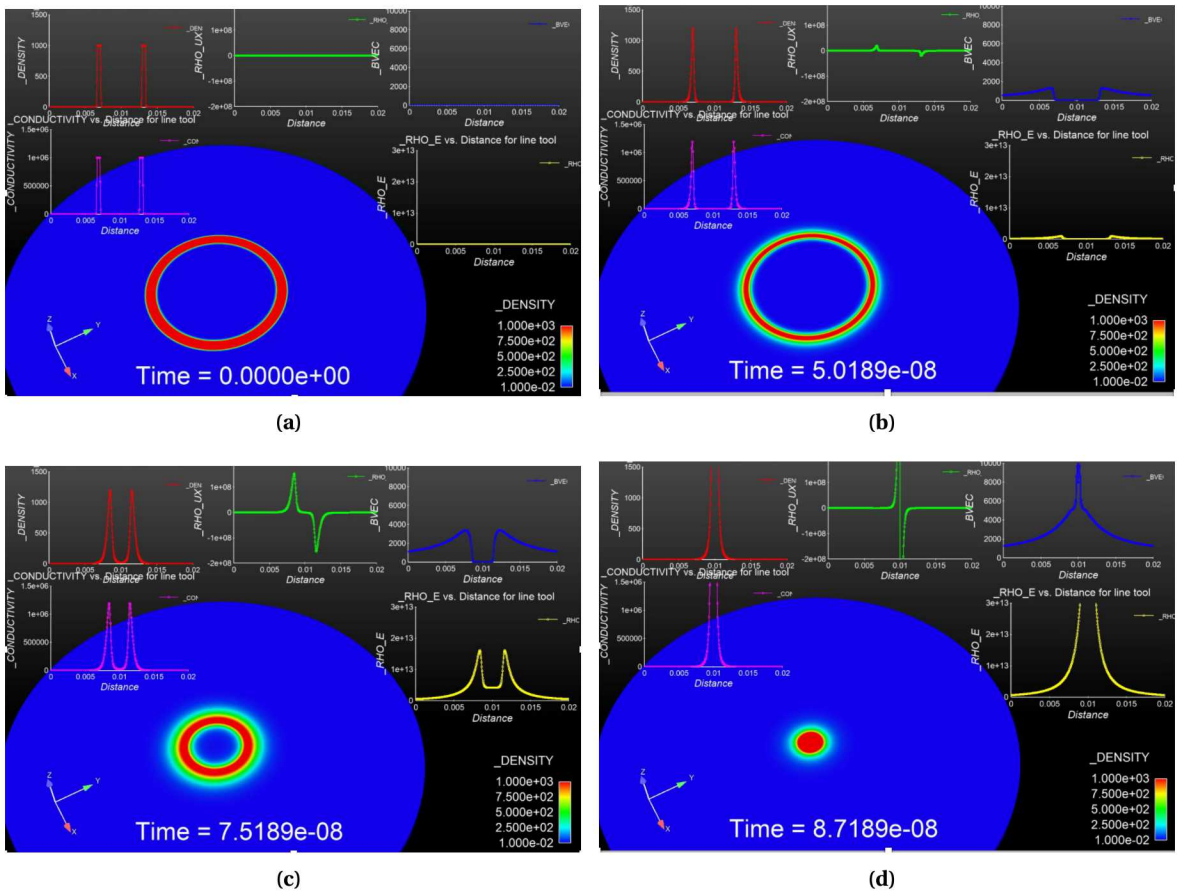

Figure 6-3. Plots of profiles for a single shell high density 2D MHD Z-pinch.

Finally we compare the density profiles (filled color contours) for the 2D (a very thin 3D disk) and 3D (cylinder) implosions on the upper surface in Figure 6-5. Clearly seen is the more non axis-symmetric profiles that are generated in the context of the 3D implosion dynamics as would be expected since the B_θ field does not inhibit variation in the z-direction from being generated on axis.

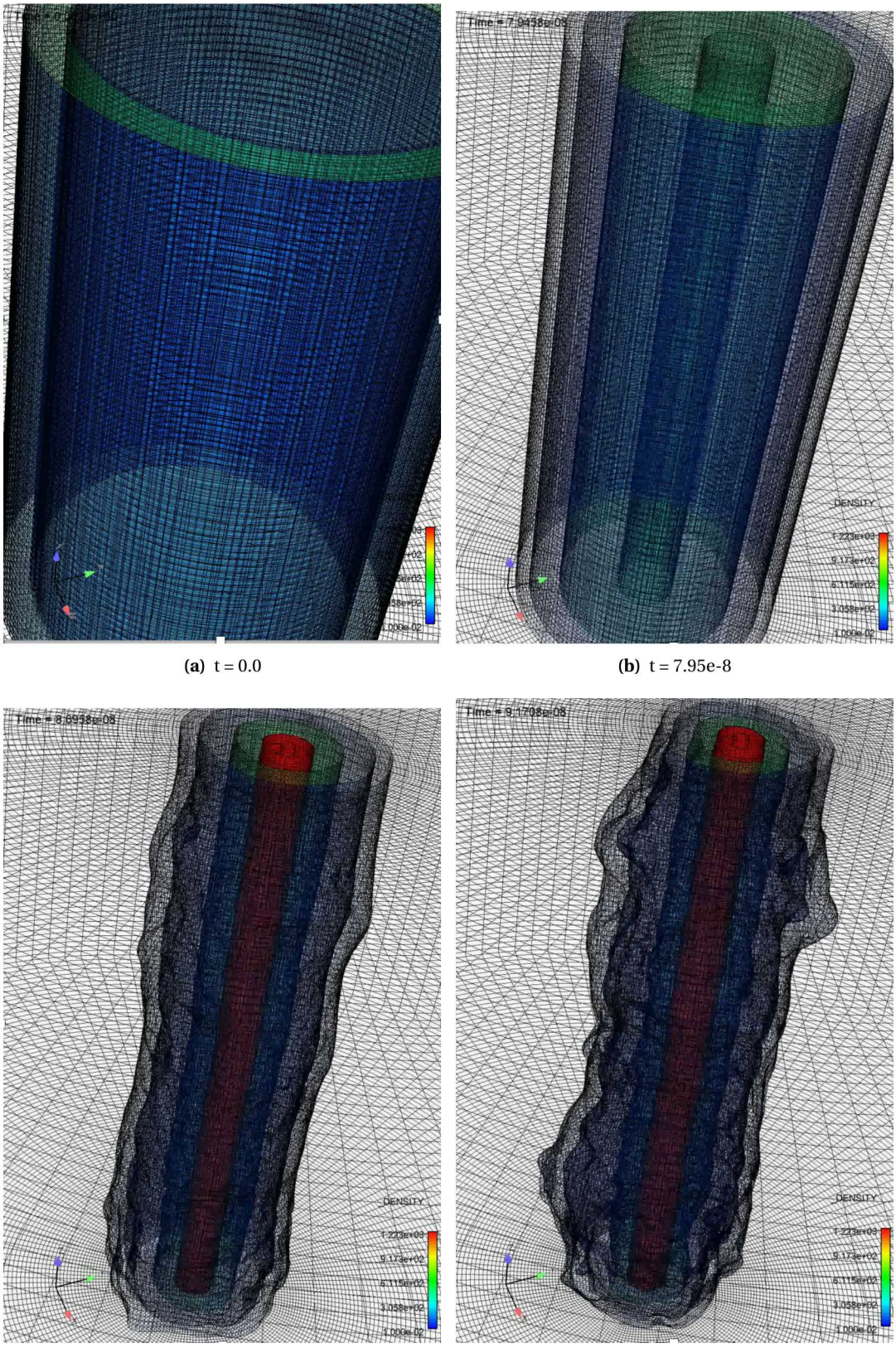

(a) t = 0.0

(b) t = 7.95e-8

(c) t = 8.7e-8

(d) t = 9.17e-8

Figure 6-4. Plots of constant density surfaces (with mesh) for a single shell high density 3D MHD Z-pinch.

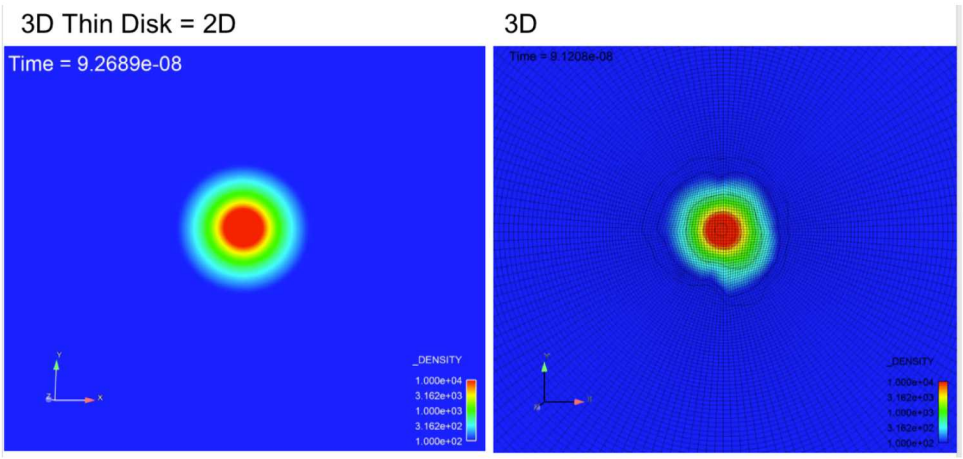

Figure 6-5. Comparison of density profiles (filled color contours) for the 2D (a very thin 3D disk) and 3D (cylinder) implosions on the upper surface.

6.2. MHD Single Shell Liner Implosion Type Problems with Complex EoS (Al, Be)

In this section, we describe aluminum and beryllium metal liner implosion simulations using the MHD model. The addition of complex materials such as metal liners represents a additional complication for modeling the equation-of-state (eos) and constituative properties. While some analytical models exist, development of these models can be quite time consuming and are material dependent. Instead, for complex materials, we have chosen to use table lookups for eos and constituative properties. For this purpose, we have implemented a UTri [26] table lookup interface in Drekar.

UTri [26] is an unstructured adaptive triangular tabular format for interpolating table based eos and constituative coefficients. When solving the resistive MHD equations for complex materials like aluminum, UTri provides; pressure, temperature, sound speed, electrical conductivity, thermal conductivity, entropy and specific heat at constant volume, given density and internal energy. Conductivity is computed and tabulated using the Lee-More-Desjarlais (LMD) [68], [38] model.

The driving magnetic field at left and right boundaries is $B_0(t)$ given by the analytic expression

$$B_0(t) = B_{max}\sqrt{q(q-1)(1-\tau^q)\tau^{q-2}} \tag{168}$$

where $B_{max} = 1{,}000\ (Tesla)$, $q = 6$, $\tau = t/t_{imp}$ and t is time normalized by the implosion time $t_{imp} \approx 100\ (ns)$. The boundary magnetic wave form is shown in Figure 6-6. This is the dimensional version of Figure 6-1, shown earlier in this report. The peak is 3000 $(Tesla)$ occurring at approximately 85 (ns).

Preliminary one-dimensional simulations of an aluminum liner implosion using the magnetic wave form and UTri eos interface were performed with the Drekar MHD model. The domain was $L = 20\ mm$, liner outer radius $r_o = 3.2\ mm$, inner radius $r_i = 2.8\ mm$ and liner width is $0.4\ mm$. A local Lax-Friedrichs (LLF) flux function where the maximum wave speed was based on velocity magnitude, sound speed and fast magneto wave speed was used for stabilization. The domain was initialized with constant pressure $P = 5000\ Pa$. The solid aluminum density was $\rho_s = 2700\ kg/m^3$ and the density of the void regions outside and inside the liner was $\rho_v = 0.001\ kg/m^3$. The void density value is chosen to be small enough to approximate a vacuum state without destabilizing the computation. Zero inflow boundary conditions were inforced along with an Neumann magnetic energy flux condition. Implicit time integration was used with a maximum timestep size $\Delta t_{max} = 0.1\ ns$.

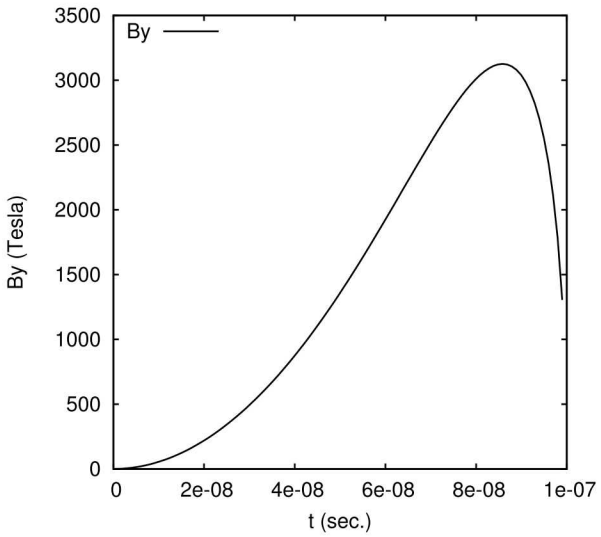

Figure 6-6. Driving Magnetic field in one-dimensional Z-pinch simulations.

Solutions for density, x-momentum, total energy and y-component of **B** at the initial state and three later states are shown in Figure 6-7. The three later states are approximately the point when the density starts to compress on the axis and the point of maximum density ($\rho_{max} \approx 15000\ kg/m^3$) which occurs at 101 ns. The final time is an arbitrary point during the rebound phase of the evolution. Notice that the maximum density is close to the initial value and the momentum has changed sign on either side of the axis.

Next, a beryllium liner implosion was simulated in one-dimension. The geometry was the same as the aluminum simulation discussed above. The aluminum table was built from the ground up for UTri. Initially, no beryllium UTri table was available. A new beryllium UTri table was constructed by converting an existing SESAME [80] eos and LMD conductivity table to the UTri format by John Carpenter. This new table was used in out beryllium liner implosion simulations. For beryllium, the solid density was specified $\rho_s = 1850\ kg/m^3$ and vapor density $\rho_v = 0.001\ kg/m^3$. The intial pressure in the system was again $P = 5000\ Pa$. Solutions for density, x-momentum, total energy and y-component of magnetic field By at the initial state and three later states are shown in Figure 6-8. The three later states are approximately the point when the density starts to compress on the axis, the point of maximum density ($\rho_{max} \approx 4930\ kg/m^3$) which occurs at 95 ns and an arbitray point during rebound. Relative to aluminum, the beryllium implosion produced a much lower ρ_{max} by a factor of three. The reasons for this is still being investigated. One reason may simply be the difference in mass between aluminum and beryllium which could account for different dynamics. Another difference is the total energy. In these simulations kinetic and magnetic components of energy make up a large fraction of the total energy. Therefore, computing internal energy can be prone to error. In addition, the dynamics of these simulations is so great that density and internal energy are often outside the range of the table. When this occurs, a zero-order extrapolation (constant) of pressure and temperature are returned from UTri. There may be other extenuating circumstances but these two alone may account for lower ρ_{max} in the case of beryllium. Nevertheless, these preliminary simulations show good promise towards being able to accurately simulate realisitic metal liner implosions.

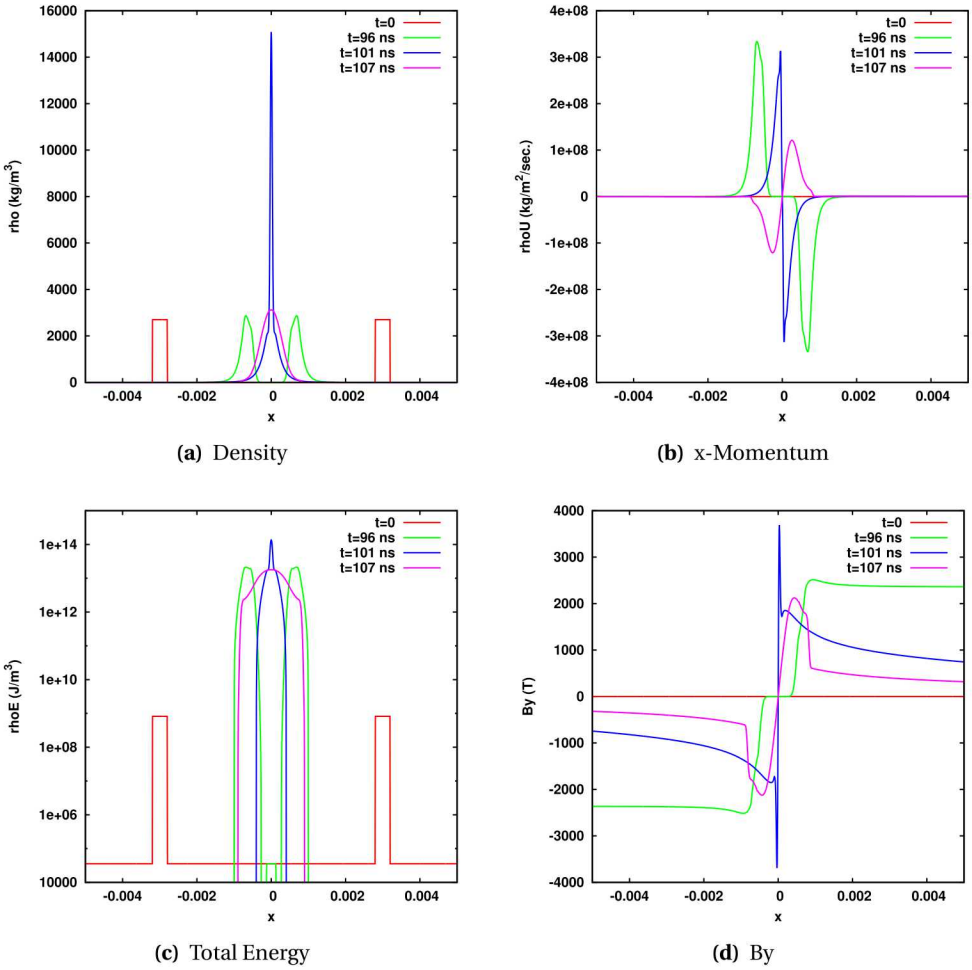

(a) Density **(b)** x-Momentum

(c) Total Energy **(d)** By

Figure 6-7. One dimensional Z-pinch of an aluminum liner with the MHD model.

6.3. Preliminary Flyer Plate Simulation and Comparison with Experiment Complex EoS (Al)

Flyer plate experiments consisting of 400 micron thick aluminum plates attached to the current return electrodes of Z-pinch targets are used to estimate return electrical currents by measuring plate velocity. The plate is accelerated by Lorentz forces and the evolution is captured by a velocity interferometer system for any reflector (VISAR) diagnostic system. At large enough distances from the center axis, in this case approximately 13 mm, the magnetic load is approximately one-dimensional and therefore, a one-dimensional simulation can be executed that accurately approximates the load forces on the plate with the expectation that the velocity evolution of the plate can be accurately predicted given the current drive pluse history. Therefore, this is a good validation test problem for our MHD model. An estimate of the drive magnetic field strengh which is a function of the current $I(t)$ is given by an experimentally measured current wave form

$$B_y(t) = \frac{2.7E-7\ I(t)}{r_p} \tag{169}$$

where r_p is the radius from the center axis to the left side of the plate. This magnetic field produces a force on the plate in the x-direction causing it to accelerate to the right. For the Drekar MHD simulations, the domain starts at a radius of $r_i = 11.2\ mm$ and ends at $r_o = 15.2\ mm$. The left edge of the plate is situated at

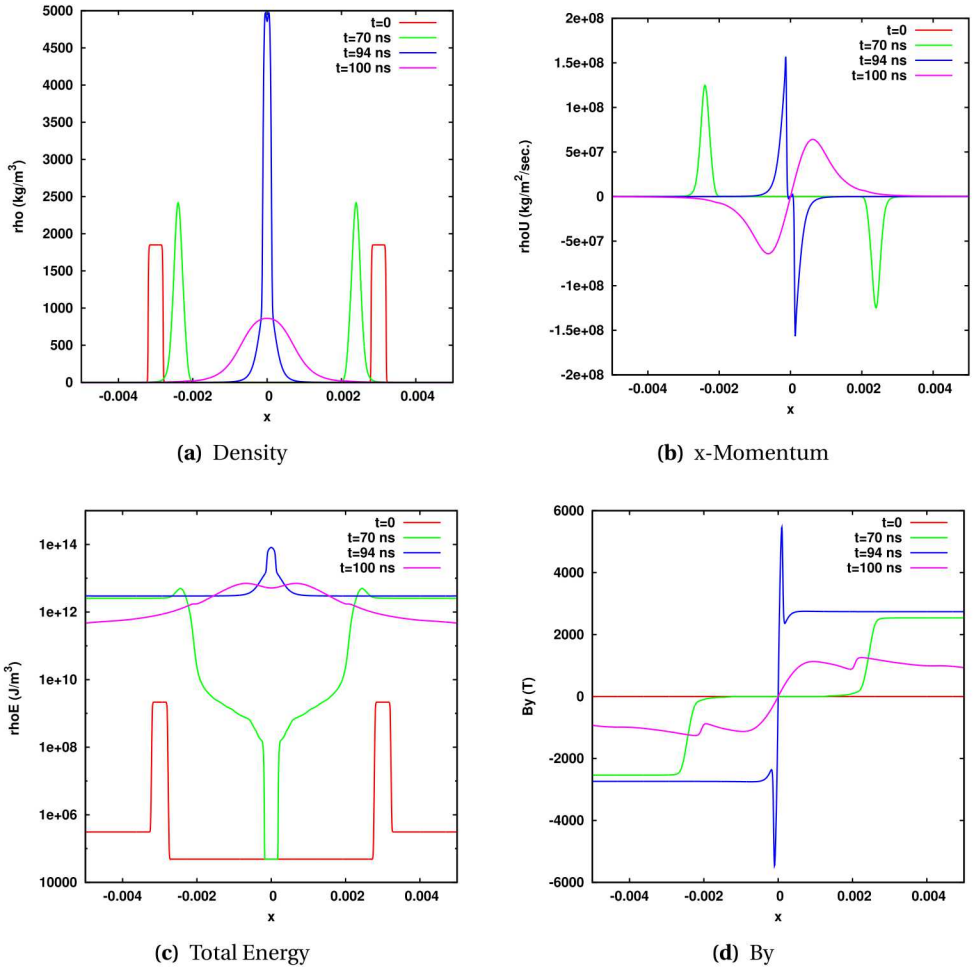

(a) Density **(b)** x-Momentum

(c) Total Energy **(d)** By

Figure 6-8. One dimensional Z-pinch of an beryllium liner with the MHD model.

$r_p = 13\ mm$, the domain is initialized with constant pressure $P = 5000\ Pa$ and 1,000 cells were used in the radial direction. The solid density was $\rho_s = 2700\ kg/m^3$ and the void density was $\rho_v = 0.001\ kg/m^3$. The current wave form for Z-pinch experiment Z2851 is shown in Figure 6-9 (a). Measured and predicted plate velocities are shown in Figure 6-9 (b). It can be seen in right panel that the simulation predicts an earlier acceleration than experiment. There is some uncertainty in the time shifted experimental data that may account for some of the early rise time, however most of the velocity history is well captured by simulation.

6.4. Multifluid Gas Puff Z-pinch Implosion Type Problems

In this section we present preliminary results on the path towards complete multifluid simulations of Ar gas puff Z-pinch experiments. We consider a common gas puff configuration consisting of two concentric annular shells of gas emitted from an 8cm diameter nozzle [54]. An idealized one-dimensional configuration is used on a domain of length 50 cm centered across the nozzle. The initial radial gas distribution consists of a sum of two Gaussian profiles for the inner and outer shells. The profiles are selected in correspondence with experimental density profiles from [54] such that the peak values and spread of the distributions approxi-

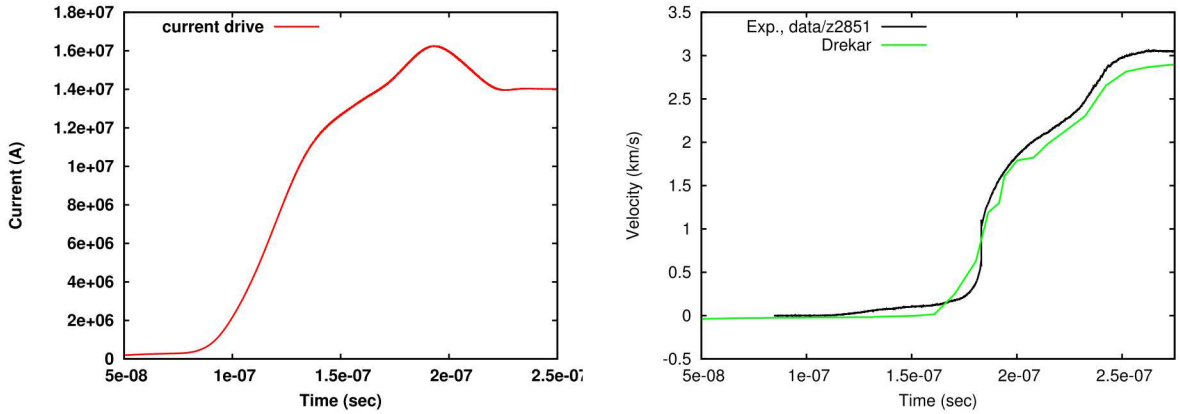

(a) Current drive

(b) Velocity evolution

Figure 6-9. Velocity evolution of an aluminum flyer plate with the one-dimensional MHD model.

mately match those of the experimental data[3]. The inner and outer gas shells are given peak number density values of 1.1E+24 m^{-3} and 3.5E+23 m^{-3}, respectively. To limit the computational cost of the simulation and avoid introducing additional complexities due to the initial breakdown phase, we assume that the initial density profile consists of only Ar^{2+} and electrons in a quasi-neutral state, and permit the gas to ionize only up to Ar^{5+}. The simulation performed as stated contains a total of 5 sets of fluid equations plus the 6 Maxwell's equations: This yields a total of 31 coupled equations.

The one-dimensional configuration is simulated on a three-dimensional Cartesian mesh consisting of 4000 mesh cells in the x-dimension and one mesh cell in the y- and z-dimensions, and applying periodic conditions across the boundaries in the y and z dimensions. The results of the simulation are shown in Figures 6-10 and 6-11 in the context of a zoomed in section of the domain ($[-0.15\text{cm}, 0.15\text{cm}]$ rather than the computational domain of $[-0.25\text{cm}, 0.25\text{cm}]$) near the initial gas puff for visualization purposes. In the first column of each subfigure, Ar^{2+} is shown in green, Ar^{3+} is shown in orange, Ar^{4+} is shown in purple, Ar^{5+} is shown in teal, and the center-of-mass quantities over all simulated charge states of Ar are shown in black. The problem is driven by placing boundary conditions for E_z along the left and right edges of the domain using a simplified $\sin^2$ profile with a rise time of 120 ns.

We have a few initial comments concerning these results. It is clear that the treatment of the electrons is over-diffusive, which has a strong impact on the distribution of current carried along the z-dimension. One would expect that the current profile would be at least somewhat compressed as the gas compresses, but this is unfortunately not the case. After the ions have begun to compress, most of the current is carried in the outer lower-density region where the electrons have diffused. This behavior significantly affects the evolution of the driving electromagnetic fields. Additionally, a large E_x field (not shown) is generated in these simulations: we are currently working to better understand how this field is generated. At this point, we suspect that this is due to an inconsistency in our treatment of the stabilization of the continuity equations and Ampere's law.

While still very preliminary, these results are encouraging. The most important processes of the gas puff Z-pinch – ionization and compression of the ion species – progress in a plausible manner as the fields build up and penetrate the dense gas. Compared to initial resistive MHD results (for 1D cf. Figure 6-13 and for 2D Figure 6-14) using a perfect gas equation of state, a simplified Knopfel conductivity model, and driven by the magnetic field profile shown in Figure 6-6, the final compressed state of the ions in the multifluid simulation

[3]While the peak density values and spread of the initial gas profiles used agrees quite well with the referenced experimental data, we note that our initial gas profiles yield smaller density values in the regions between the annular shells than is suggested by experiments.

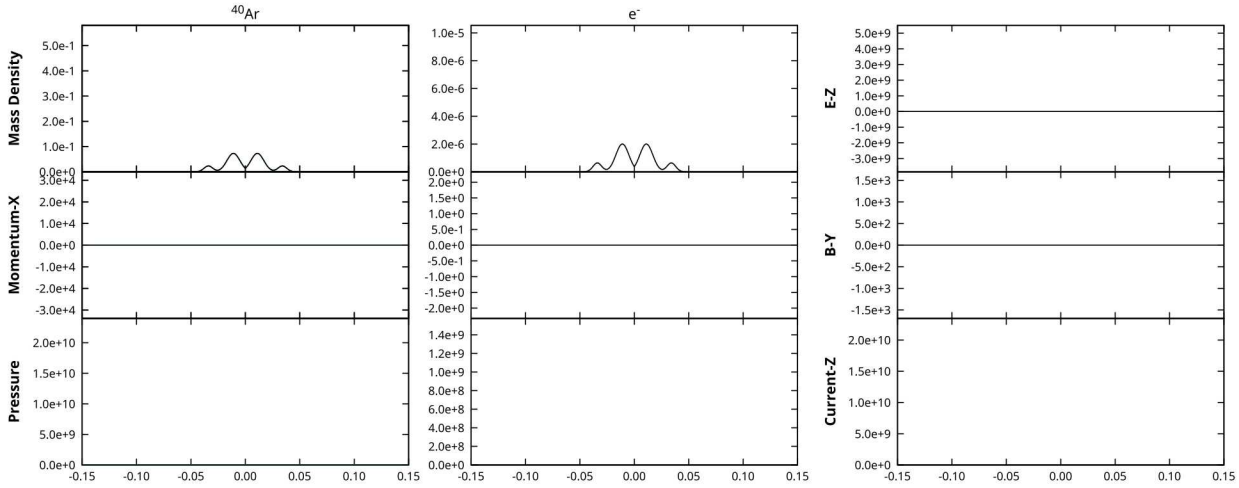

(a) t = 0.0

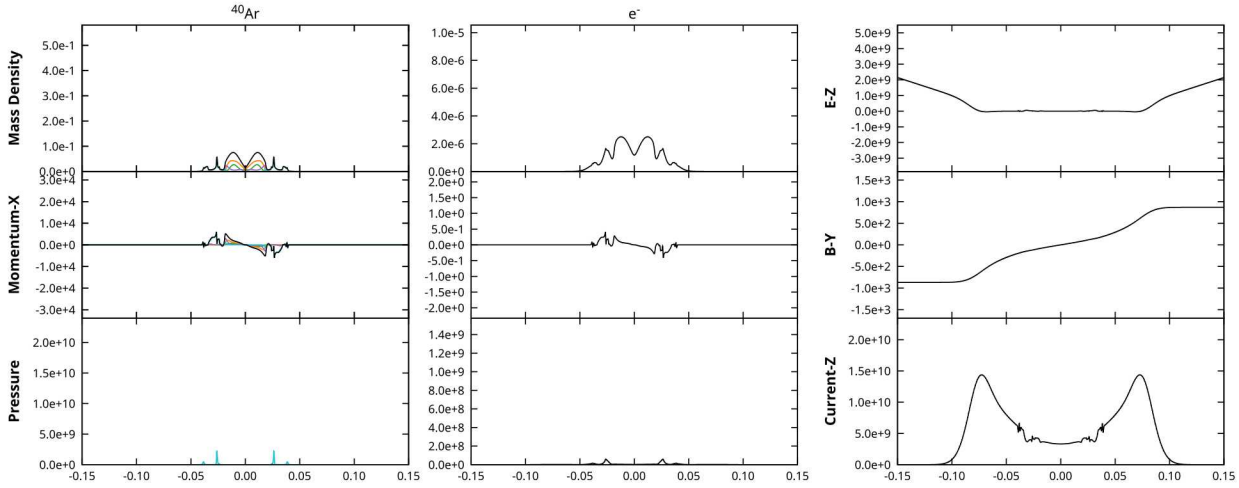

(b) t = 9.3e-7

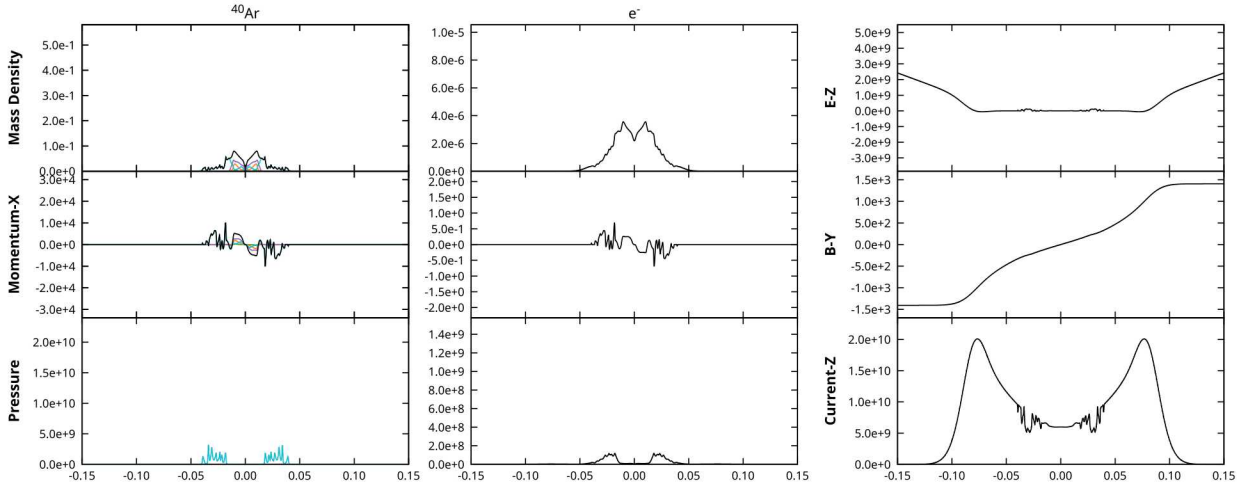

(c) t = 1.15e-7

Figure 6-10. Preliminary multifluid Ar gas puff Z-pinch tracking charge levels between Ar^{2+} and Ar^{5+} – Part I. The images are a subset of the domain and detail the subdomain $[-0.15\mathrm{cm}, 0.15\mathrm{cm}]$.

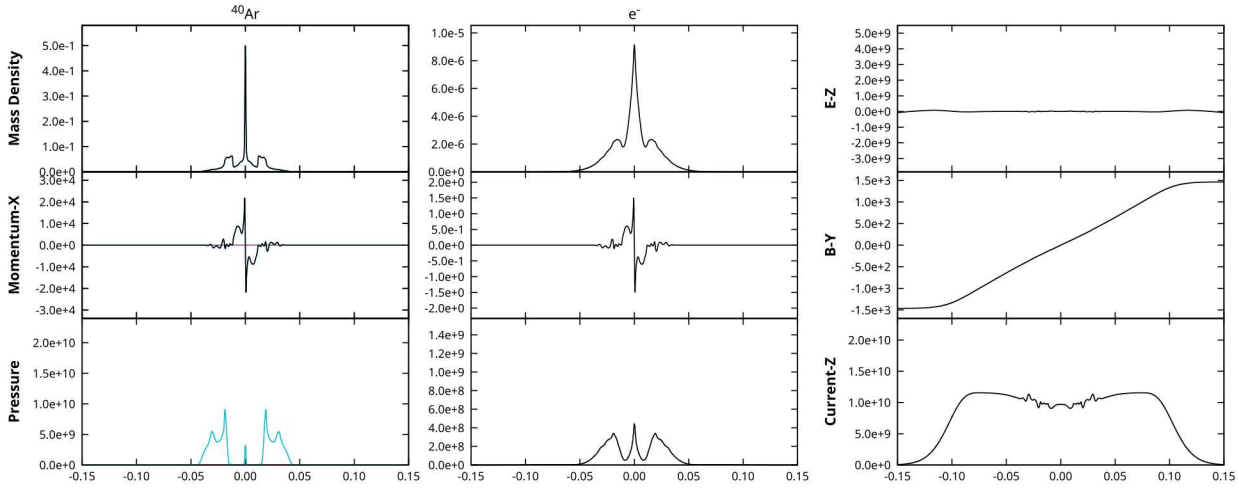

(a) t = 1.5e-7

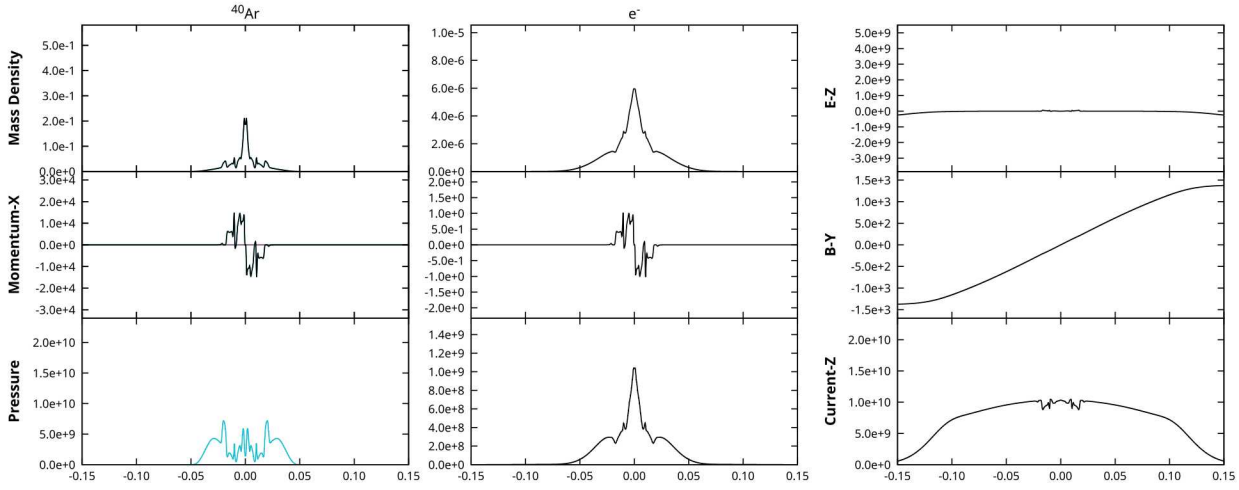

(b) t = 2.0e-7

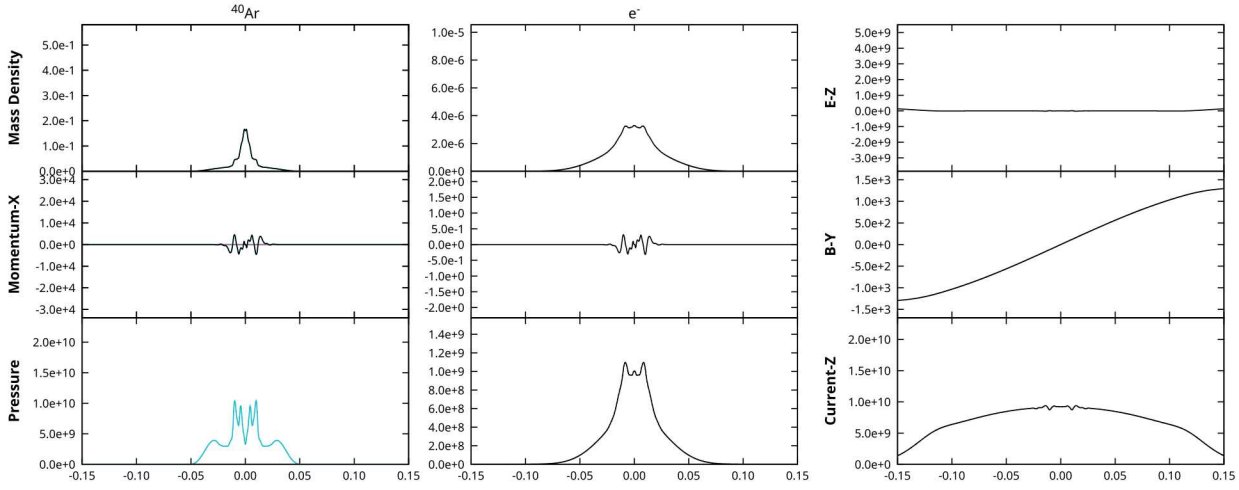

(c) t = 2.5e-7

Figure 6-11. Preliminary multifluid Ar gas puff Z-pinch tracking charge levels between Ar^{2+} and Ar^{5+} – Part II. The images are a subset of the domain and detail the subdomain $[-0.15\mathrm{cm}, 0.15\mathrm{cm}]$.

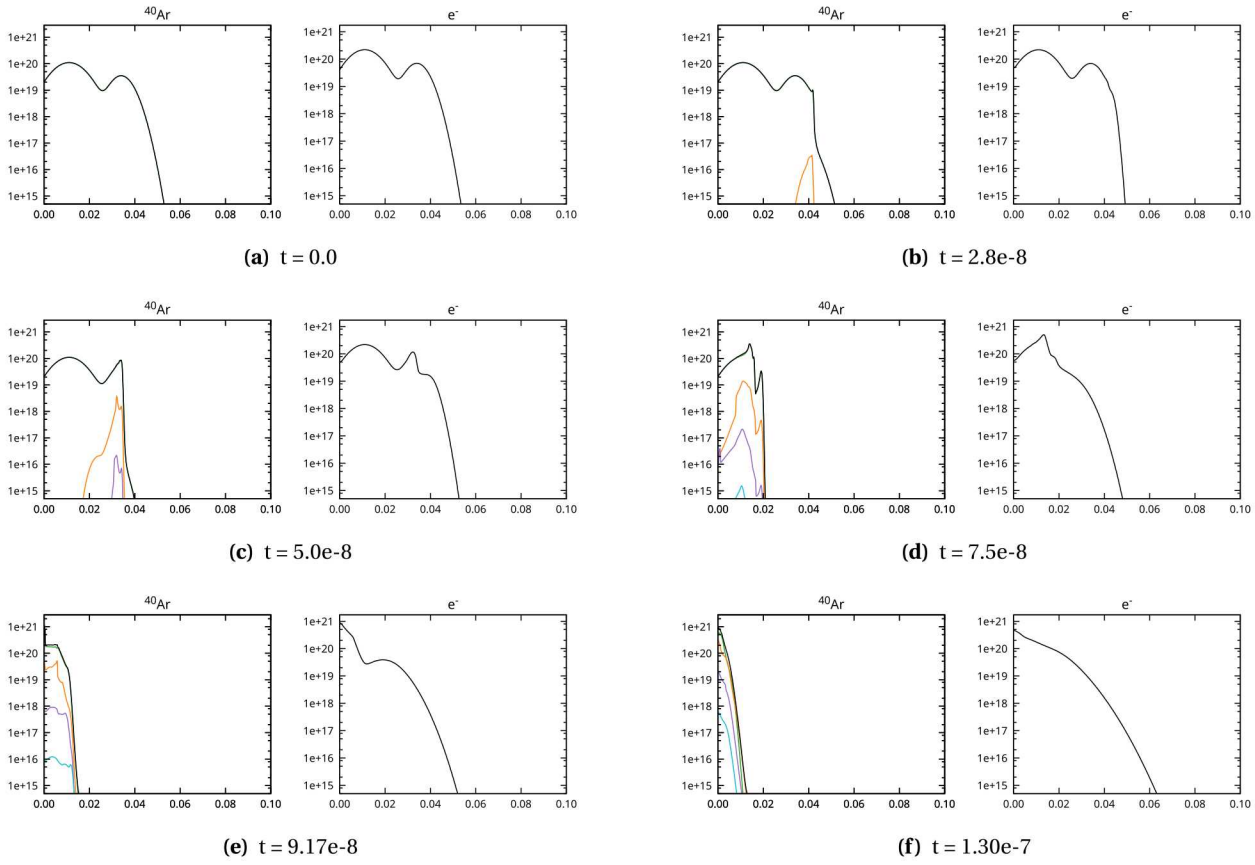

(a) t = 0.0 **(b)** t = 2.8e-8

(c) t = 5.0e-8 **(d)** t = 7.5e-8

(e) t = 9.17e-8 **(f)** t = 1.30e-7

Figure 6-12. Number density of ionization states of low-density multifluid Ar gas puff Z-pinch tracking charge levels between Ar^{2+} and Ar^{5+}. The images are a subset of the domain and detail the subdomain $[-0.1\text{cm}, 0.1\text{cm}]$.

seems to compare reasonably well. Even though differences in the problem setup of the multifluid and resistive MHD simulations lead to different timings of the compression, there is a qualitative correspondence between the ion density at stagnation, maximum pressure values, and to a certain extent temperatures in the compressed core.

Results for a second simulation using lower initial density values are shown in Figure 6-12, more clearly showing the progress of ionization in the Ar gas. As current begins to flow through the gas, the electrons are heated from the initial temperature of 8000 degrees K, and the gas proceeds to ionize. This ionization contributes to the current carrying capacity of the plasma, and the ionized gas compresses under the influence of the magnetic field. We note here that the lower-density conditions of this simulation significantly limit the degree to which the Ar is able to ionize, and simulations using higher-density conditions closer to that used in experimental setups ionize much more rapidly and to much higher charge states.

In both simulations presented here, the dissipation in the electron fluid due to the low-order Rusanov AFC stabilization contributes significantly to the spreading of the electron population. We are currently examining this issue more carefully and pursuing mitigation strategies, such as the use of Roe-type AFC stabilization and higher-order AFC methods, both of which introduce less dissipation into the solution.

Work is currently underway to extend the multifluid simulation results in several directions. First, we have begun to attempt two-dimensional thin disk multifluid implosions to capture asymmetric instabilities in the compression of the gas. Second, it is clear that including more charge states of Ar in the simulation is of

crucial importance. We have been slowly extending the range of charge states considered so that (i) the initial breakdown can be represented to some degree, and (ii) the gas is able to ionize further, ideally to a level where K-shell emission would be possible.

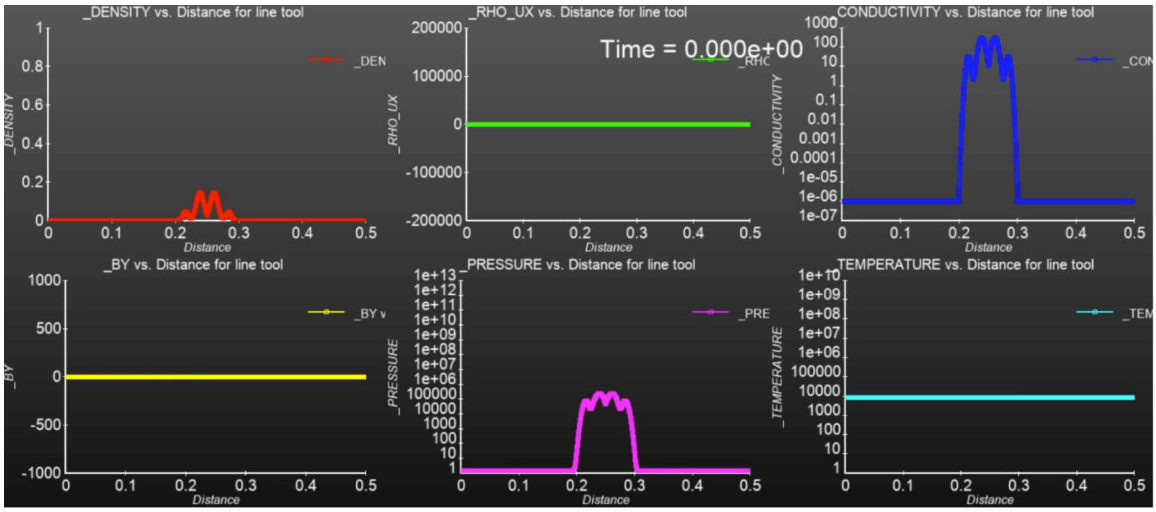

(a) t = 0.0

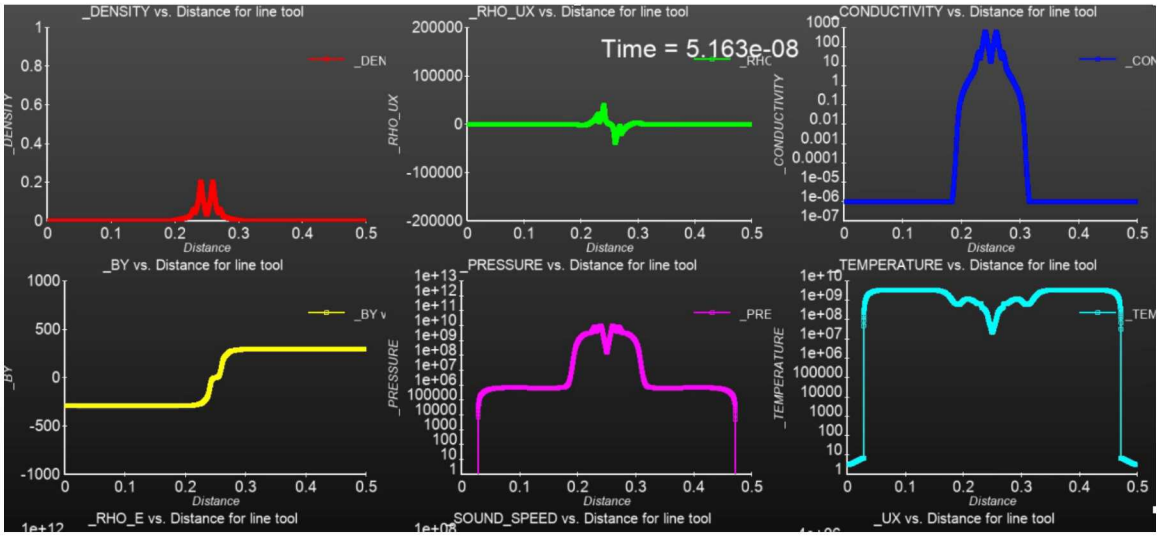

(b) 5.163e-8

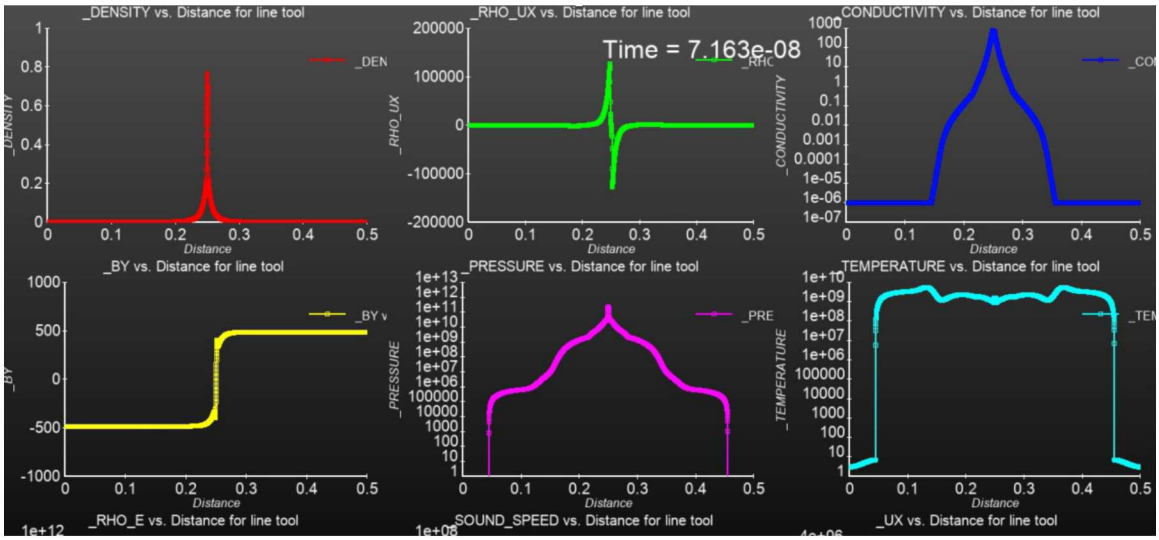

(c) 7.163e-8

Figure 6-13. Preliminary 1D resistive MHD gas puff Z-pinch implosions for Ar ideal gas with rough Knopfel conductivity model

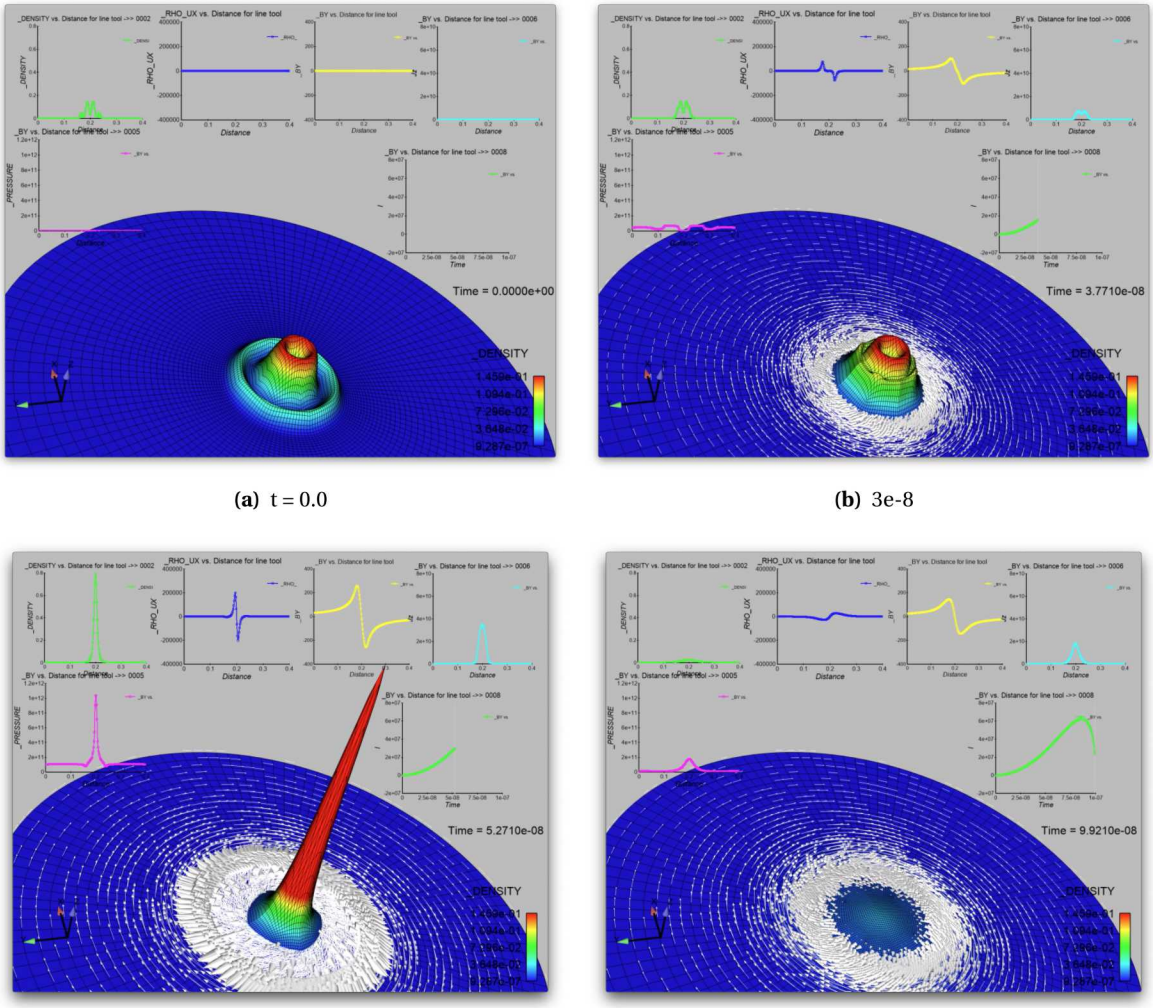

(a) t = 0.0 **(b)** 3e-8

(c) 5.3e-8 **(d)** 1e-7

Figure 6-14. Preliminary 2D resistive MHD gas puff Z-pinch implosions for Ar ideal gas with rough Knopfel conductivity model. Drive is with $q = 6$ and with a maximum current of 60MA and implosion time of 100ns.

7. INITIAL COMPARISONS WITH A PIC CODE ON CHALLENGING PROBLEMS

7.1. Expansion into Near Vacuum

In this section and the next, we compare PIC solutions to the multifluid model in two one-dimensional expansion problems. The motivation is to show consistency between the two formulation. The first problem we consider is an expansion of a quasi-neutral plasma into a near vacuum. The domain of the problem is taken to be one-dimensional ($\mathbf{v_s} = [\mathrm{v}_s]$) spanning $-L \le x \le L$, $L = 0.01$ m, with the initial conditions for the electrons and ions given with a specified nominal number density n_0:

$$n_e = \begin{cases} n_0 & |x| < L/20 \\ n_0 \times 10^{-6} & |x| \ge L/20 \end{cases} \mathrm{m}^{-3} \tag{170}$$

$$\mathrm{v}_e = 0 \tag{171}$$

$$T_e = 10{,}000\,\mathrm{K} \tag{172}$$

$$n_i = \begin{cases} n_0 & |x| < L/20 \\ n_0 \times 10^{-6} & |x| \ge L/20 \end{cases} \mathrm{m}^{-3} \tag{173}$$

$$\mathrm{v}_i = 0 \tag{174}$$

$$T_i = 10\,\mathrm{K} \tag{175}$$

The mass ratio between electrons and ions was taken as $m_i/m_e = 10$, where $m_e \approx 9.109 \times 10^{-31}$ kg and the charges given $q_i = -q_e = e \approx 1.602 \times 10^{-16}$ C. Simulations of collisionless cases were run until a final time of 5×10^{-9} s.

In the electrostatic approximation Maxwell's equations reduce to a single scaler potential equation

$$\nabla \cdot \mathbf{E} = \nabla \cdot \nabla \phi = \frac{q}{\epsilon_0}. \tag{176}$$

Aleph [17] solves the scalar potential equation (176) (ES) for determining the electric field. Drekar solves either the full Maxwell's equations Figure 2-1 (EB) or the potential equation (ES). A comparison between the electrostatic and electrodynamic model formulations was investigated at a nominal number density $n_0 = 10^{16}$. The results for a range of resolutions are depicted in Figure 7-1-7-3. While the high density region electron number density converges to plotting accuracy relatively quickly (on a log scale) the low density regions are observed to not be converged to plotting accuracy even at the highest resolution of $\Delta x = 2L/16384$. Both the ion number density and electric field converge to plotting accuracy for both cases. This trend is similar for both the electrostatic and electrodynamic cases which yield similar results at the highest resolutions as can be seen in comparison presented in Figure 7-4 at the highest resolution of $\Delta x = 2L/16384$ and are compared to the Aleph PIC solution.

Comparing the PIC results to those obtained with the multifluid approach implemented in Drekar reasonable agreement between the two can be seen considering the significant differences in modeling approaches. However, both the ion and electron high density regions in the fluid simulations spread further than in the PIC computation. In addition, although the electron density is not converged, the electron density is overpredicted in the low density region in the fluid code compared to the kinetic approach. This difference then leads to an overpredition in the electric field as well in this region as suggested by the electrostatic approximation, Eq. 176. Additional differences in the electric field can also be seen in the inner region between the two modeling approaches.

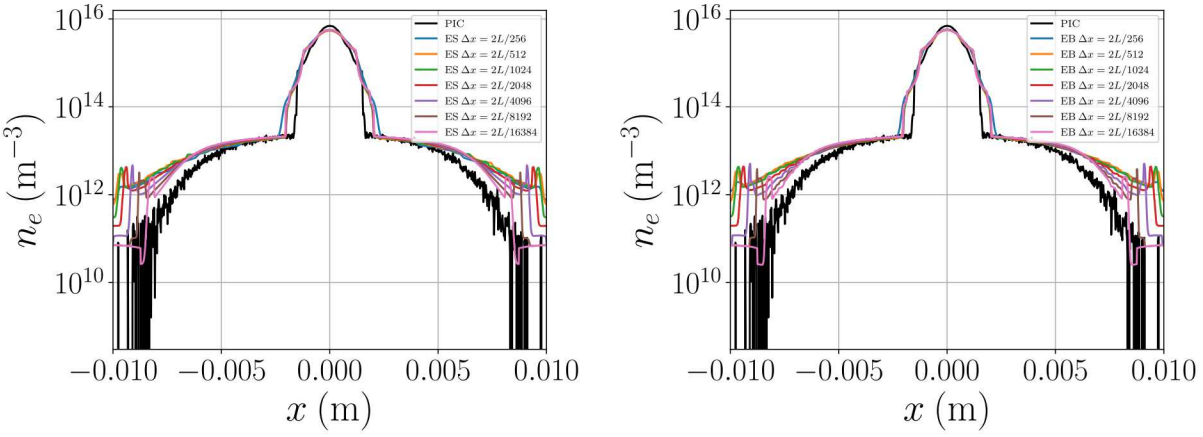

(a) Electrostatic **(b)** Electrodynamic

Figure 7-1. Electron number density profiles as a function of spatial resolution.

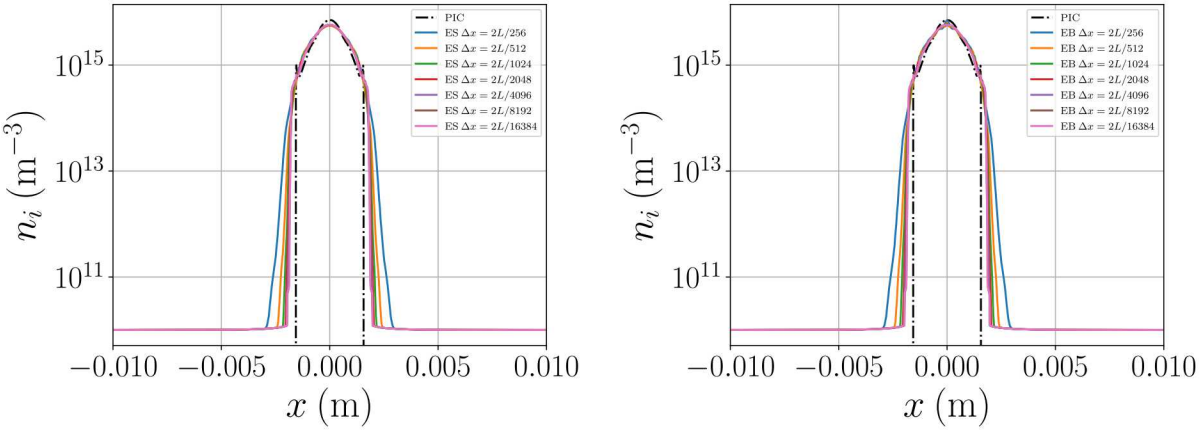

(a) Electrostatic **(b)** Electrodynamic

Figure 7-2. Ion number density profiles as a function of spatial resolution.

7.2. Neutral Expanding One-dimensional Slab

The second PIC/Multifluid comparison is of a neutral expanding one-dimensional "slab". The situation is very similar to the previous example with two exceptions. First, positively charged particles are assumed to have the same mass as electrons and will be referred to as positrons. Second, a background gas with density ratio $Ns = 0.01$ is surrounding the slab. Robinson [107] has derived both kinetic and continuum solutions for this problem, valid for short wave propagation time durations. The two solutions are quite different. The kinetic solution is assumed to be collisionless. It is smooth and diffused compared to the fluid soltion which is assumed collisional containing expansion, slip discontinuity and shock waves resembling two apposing shocktubes.

The domain is $L = 0.02\ m$ and the slab width is $Lp = 0.001\ m$. The number density in the slab is $n_{e0} = n_{i0} = 1.0e16$ and the temperature is $T_e = T_i = 10,000\ K$. Solutions for electrons or positrons should be equivalent so we consider just one species. Intial drift velocities are zero and pressure in the slab is determined by

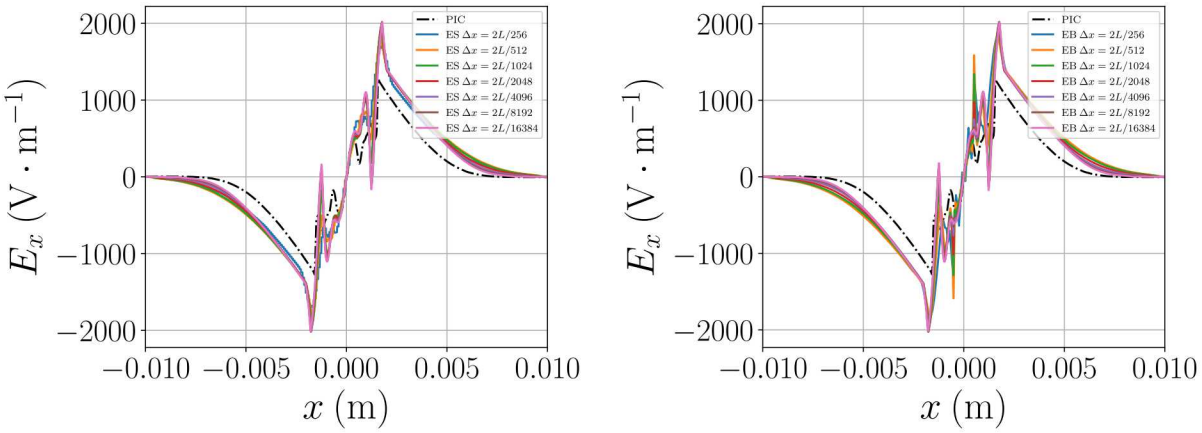

(a) Electrostatic

(b) Electrodynamic

Figure 7-3. Electric field profiles as a function of spatial resolution.

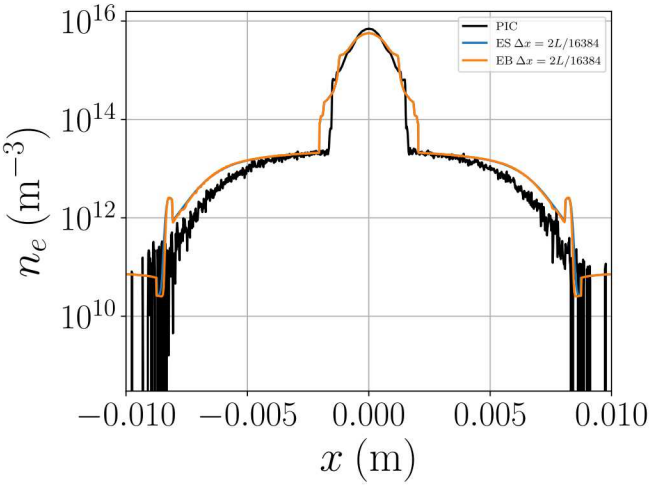

Figure 7-4. Comparison between electrostatic and electrodynamic electron number densities for $\Delta x = 2L/16384$.

$P_0 = \rho_0 \sigma^2$ where $\rho_0 = n_{e0} m_e$ is mass density, $\sigma = \sqrt{k_B T_e / m_e}$ and k_B is Boltzmann's constant. Density and pressure in the background are $\rho_1 = Ns\rho_0$ and $P_1 = Ns\rho_0\sigma$ respectively. At time $t = 0$, similar to a shocktube, the slab begins to expand outward.

Comparisons for number density, velocity and pressure between Aleph PIC solutions and the kinetic analytic solution and between Drekar multifluid solutions with the fluid analytic solution at $t = 2\ ns$ are shown in Figure 7-5 respectively. For these comparisons, 2048 cells were used. Note that the Aleph solutions agree well with the kinetic and Drekar multifluid solutions agree well with the fluid analytic solutions.

For the densities used in this problem collisions are not important and so the kinetic solution is the expected instead of the fluid solution. To see why, we estimate the Knusen number Kn. The Knusen number is defined as ($Kn = \lambda / L \approx 10^7$) where λ is the mean free path and L is a characteristic length scale. For a continuum assumption to be valid, $Kn \leq 1$.

Using PIC terminology, $Kn = \frac{1}{L\sigma_e n_e}$ where $\sigma_e = \pi d^2$ is the cross sectional area of the particle. If this scaling

holds for the continuum assumption, σ_e or n_e can be increased in order to decrease Kn. In order to capture the fluid solution in the PIC code, and test consistency between the two formulations, d was artificially increased by a factor $1.58e7$ to reduce $Kn \approx 1.3e-4$, and elastic collisions were activated using a variable hard sphere model. The results are shown in Figure 7-6. Notice now that the PIC solution is capturing the three wave solution approximating the fluid solution instead of the kinetic including the shock and slip discontinuities.

Studies like these are important for establishing consistency between PIC and multifluid plasma descriptions. We have initiated PIC/Multifluid comparisons of a neutral gas injected into a hot plasma. These simulations include ionization and recombination of plasmas with multipe charge states. These results will be reported in the future.

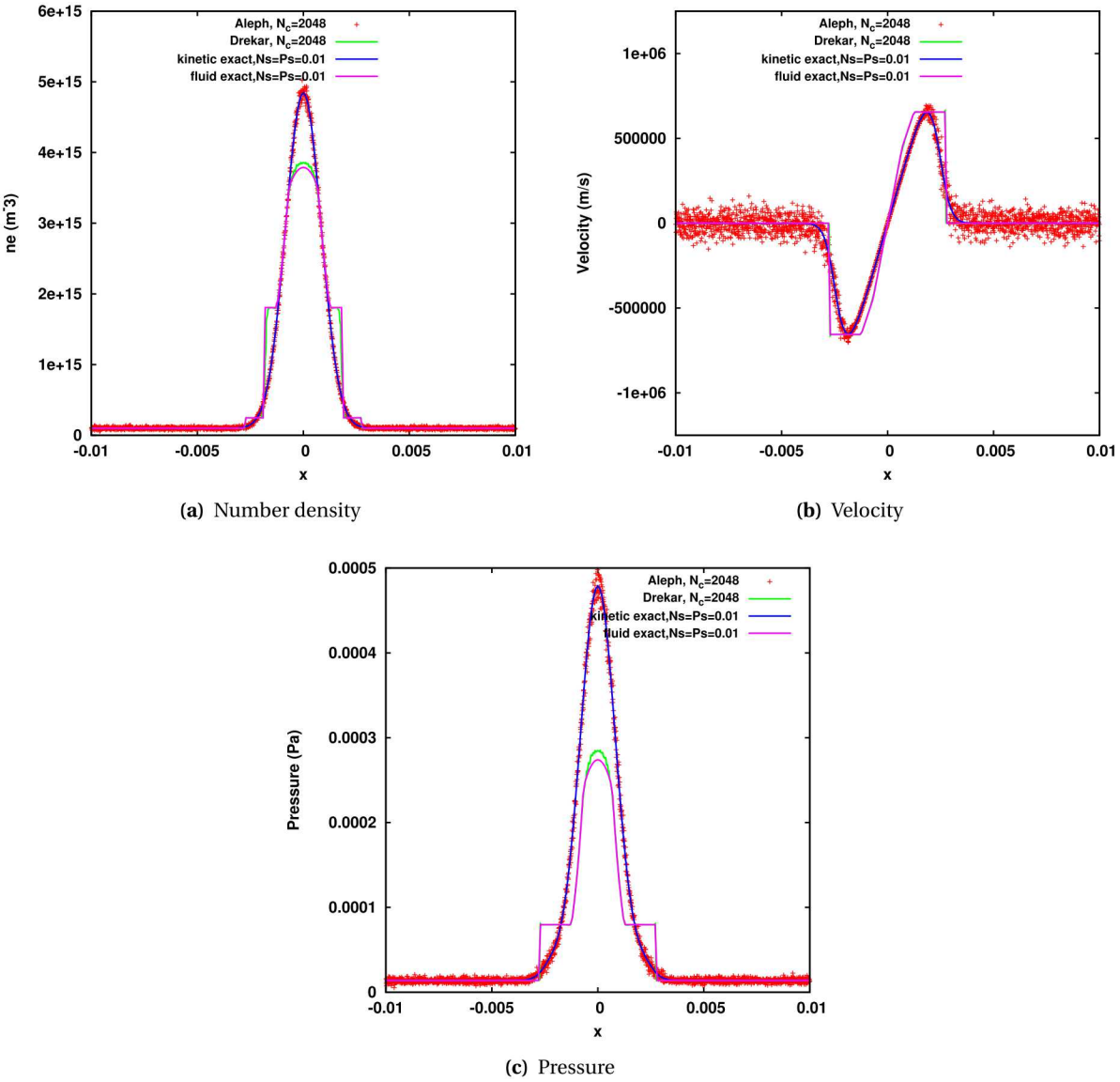

(a) Number density

(b) Velocity

(c) Pressure

Figure 7-5. Comparision of PIC solution with elastic collisions between like species with an ion/electron multifluid model to analytic solutions.

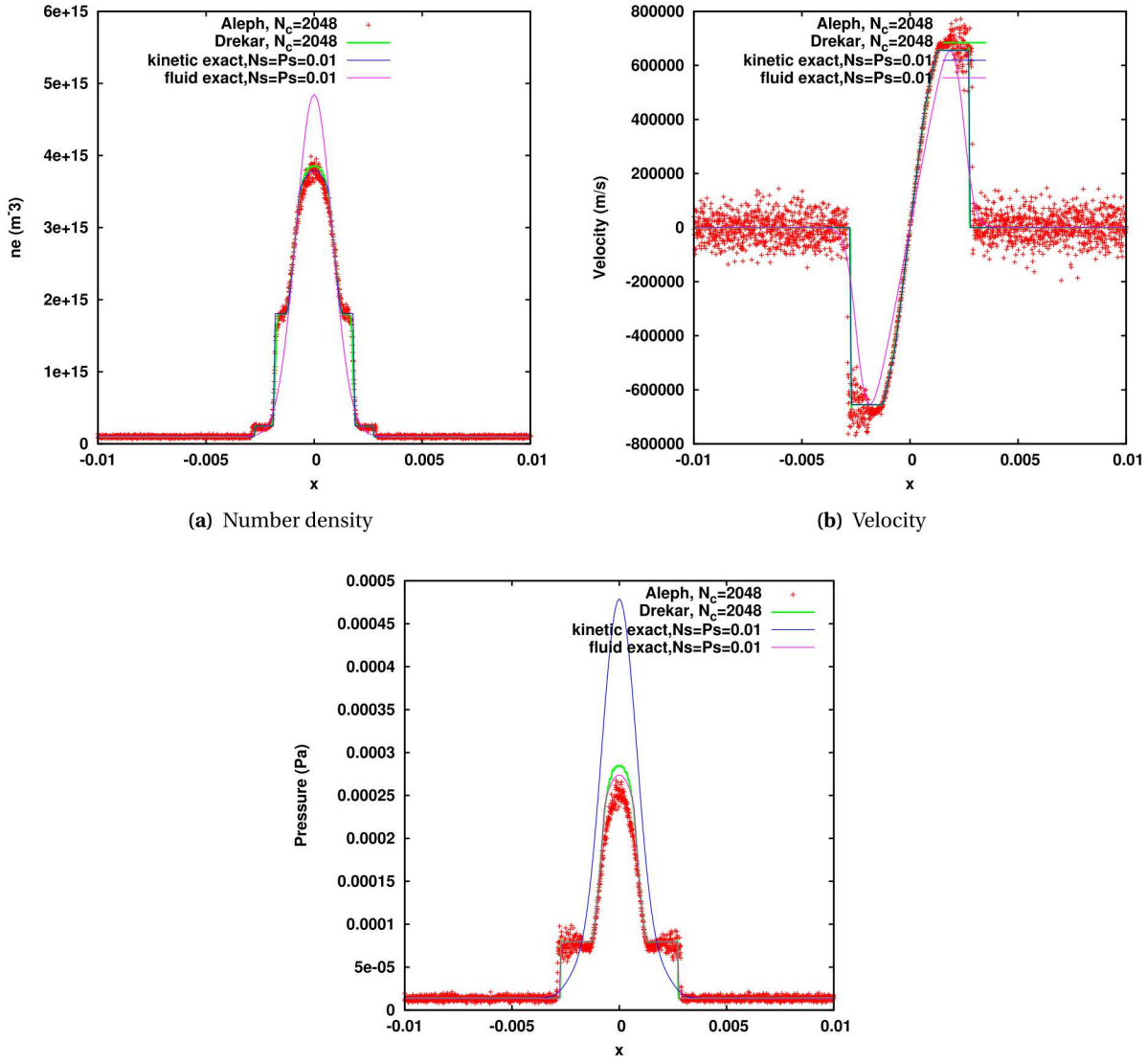

(a) Number density

(b) Velocity

(c) Pressure

Figure 7-6. Comparision of PIC solution without collisions between like species with an ion/electron multifluid model to analytic solutions.

8. CONCLUSIONS

Critical DOE and Sandia science and weapons applications require analysis of strongly electromagnetically (EM) driven experiments producing complex multiphysics plasmas. These include pulsed-power experiments for radiation effects, dynamic materials, magneto-inertial fusion (MIF), and basic high energy density physics. Our overarching goal in this project has been the initial development of a unique, robust, and accurate implicit/explicit (IMEX) computational physics/mathematical approach for multi-fluid multi-physics plasma research that will help to uniquely position SNL at the forefront of continuum computational analysis supporting pulsed-power sciences.

The key research and development results of this effort include:

- We have carried out the development and demonstration of new implicit/implicit-explicit (IMEX) time-integration and scalable iterative solvers for multifluid electromagnetic plasmas for simulations with high electromagnetic (EM) CFL, high plasma oscillation / cyclotron frequencies and zero electrical conductivity regions. We have also demonstrated scalable solution of full-Maxwell's equations in the long-time-scale / low-frequency limit, as well as the solution of a full multifluid electromagnetic plasma formulation in the single-fluid MHD limit for visco-resistive and Ideal MHD. These capabilities are necessary for efficient simulations of multifluid plasma systems extending to
  - higher densities,
  - strong magnetic fields,
  - domains with significant charge separation and quasi-neutral sub-regions,
  - multi-scale physics requiring high resolution meshes (1 micro meter)
- This unique implicit/IMEX Eulerian formulation has has been demonstrated for multifluid electromagnetic plasma systems with fully-ionized collsionless systems, as well as partially ionized collisional plasma systems with ionization/recombination effects modeled with an integrated coronal model.
- The multifluid formulation was demonstrated to be reasonably robust and accurate on a significant number of verification type problems. These included linear waves of the multifluid system (including magnetized and unmagnetized systems), collisional relaxation problems for damped plasma oscillations, long-time scale integration for equilibrium charge level distributions for the coronal model of classical plasmas, and also to allow solution of the full multifluid EM plasma systems in the asymptotic limit of visco-resistive and ideal (dispersive) MHD.
- The multifluid EM plasma model, implicit/IMEX formulations and solution methods appear very promising for advanced computational analysis of complex multiple-time-scale multifluid plasma systems and have been demonstrated for smooth solutions, and prototype multifluid shock systems.
- We have demonstrated quantitative long-time-scale time-integration of ionization/recombination to an equilibrium solution for the charge-level distribution or a number of atomic species (H,He,Be,Ne,Al,Ar) compared to direct-solution of a coronal model for plasma equilibrium.
- We have demonstrated a initial proof-of-principle demonstration of the solution of the full multifluid EM plasma model with collisions, ionization/recombination for a reasonably realistic Ar gas puff Z-pinch configuration driven with a specified boundary condition for a transverse electromagnetic wave specified by an electric field. The results while very preliminary have some very encouraging aspects of being able to track the ionization front in the Ar gas as it penetrates the plasma, couples the magnetic field to the load, and implodes the gas puff. Clearly as outlined in our report there are significant issues that must still be addressed but these initial results are encouraging.

- The development and evaluation of new adaptive embedded error-control for IMEX time integration methods that enforce both strong-stability-preservation and L-stability properties for time integration of complex multiphysics multifluid EM plasma systems.
- Completed development of an implicit iteratively limited algebraic flux correction (AFC) continuous Galerkin finite element (FE) method for general conservation law systems (e.g. Euler), for ideal/resistive MHD, and an implementation for the full multifluid EM plasma model.
- The development and an initial demonstration (both quantitative and qualitative results) that the Drekar IMEX multiphysics multifluid EM plasma code can be applied as a valuable applied math and computational algorithm development R&D platform for challenging problems of critical importance to SNL and DOE. Clearly, further development and a much more comprehensive quantitative evaluation of these algorithms and the corresponding software implementations is required. However, we believe there is a credible path forward for the successful algorithms, mathematical models, and this prototype research code as a technology-base to help contribute to the development of a next-generation multiphysics multifluid EM plasma capabilities at SNL.
- As an important specific pulsed power mission impact, this activity has also influenced the development of new capabilities in the ALEGRA production MHD code which is now using an IMEX-like time discretization, inspired by Drekar's approach, to simulate a single fluid plasma with classical Ohm's law. While this model is not capable of describing important physics such as the Hall effect (described by the multifluid model), this new generation ALEGRA model benefits from non-degeneracy in the limit of zero conductivity and low density removing fast magnetosonic time-step restrictions. The transfer of ideas and methodology from a research code to a production code demonstrates the increased maturity and technology readiness of the IMEX approach to continuum plasma physics. This new full-Maxwell hydrodynamics (FMHD) model in the ALEGRA production code is expected to enable more robust and efficient solutions of challenging pulsed power and HEDP relevant applications (Comments contributed by A. Robinson and D. McGregor of the ALEGRA development team.)
- As two additional important specific pulsed power mission impacts, the R&D carried out in this LDRD effort has also (1) very significantly enabled the development, implementation and evaluation of the EMPIRE-fluid effort in the context of solution methods, multifluid plasma verification problems, and for important comparisons of solutions for challenging problem for evaluation of the EMPIRE-fluid multifluid formulation, (2) also enabled progress in the GCLDRD for hybrid fluid/kinetic modeling and comparisons between PIC and multifluid models.

REFERENCES

[1] S. A. Abdel-Naby, D. Nikolić, T. W. Gorczyca, K. T. Korista, and N. R. Badnell, *Dielectronic recombination data for dynamic finite-density plasmas: XIV. The aluminum isoelectronic sequence*, Astronomy & Astrophysics, 537 (2012), p. A40, doi:10.1051/0004-6361/201117544.

[2] Z. Altun, A. Yumak, N. R. Badnell, J. Colgan, and M. S. Pindzola, *Dielectronic recombination data for dynamic finite-density plasmas: VI. The boron isoelectronic sequence*, Astronomy & Astrophysics, 420 (2004), pp. 775–781, doi:10.1051/0004-6361:20040964.

[3] Z. Altun, A. Yumak, N. R. Badnell, J. Colgan, and M. S. Pindzola, *Erratum to: Dielectronic recombination data for dynamic finite-density plasmas: VI. The boron isoelectronic sequence*, Astronomy & Astrophysics, 433 (2005), pp. 395–395, doi:10.1051/0004-6361:20040003e.

[4] Z. Altun, A. Yumak, N. R. Badnell, S. D. Loch, and M. S. Pindzola, *Dielectronic recombination data for dynamic finite-density plasmas: XI. The sodium isoelectronic sequence*, Astronomy & Astrophysics, 447 (2006), pp. 1165–1174, doi:10.1051/0004-6361:20053278.

[5] Z. Altun, A. Yumak, I. Yavuz, N. R. Badnell, S. D. Loch, and M. S. Pindzola, *Dielectronic recombination data for dynamic finite-density plasmas: XIII. The magnesium isoelectronic sequence*, Astronomy & Astrophysics, 474 (2007), pp. 1051–1059, doi:10.1051/0004-6361:20078238.

[6] D. N. Arnold, P. B. Bochev, R. B. Lehoucq, R. A. Nicolaides, and M. Shashkov, *Compatible spatial discretizations*, vol. 142, Springer Science & Business Media, 2007.

[7] U. Ascher, S. Ruuth, and B. Wetton, *Implicit-explicit methods for time-dependent partial differential equations*, SIAM Journal on Numerical Analysis, 32 (1995), pp. 797–823, doi:10.1137/0732037, https://doi.org/10.1137/0732037, arXiv:https://doi.org/10.1137/0732037.

[8] U. M. Ascher and L. R. Petzold, *Computer Methods for Ordinary Differential Equations and Differential-Algebraic Equations*, Society for Industrial and Applied Mathematics, Philadelphia, PA, USA, 1st ed., 1998.

[9] U. M. Ascher, S. J. Ruuth, and R. J. Spiteri, *Implicit-explicit runge-kutta methods for time-dependent partial differential equations*, Applied Numerical Mathematics, 25 (1997), pp. 151 – 167, doi:https://doi.org/10.1016/S0168-9274(97)00056-1, http://www.sciencedirect.com/science/article/pii/S0168927497000561. Special Issue on Time Integration.

[10] N. R. Badnell, *Dielectronic recombination data for dynamic finite-density plasmas: X. The hydrogen isoelectronic sequence*, Astronomy & Astrophysics, 447 (2006), pp. 389–395, doi:10.1051/0004-6361:20053269.

[11] N. R. Badnell, *Radiative recombination data for modeling dynamic finite-density plasmas*, The Astrophysical Journal Supplement Series, 167 (2006), pp. 334–342, doi:10.1086/508465.

[12] N. R. Badnell, M. G. O'Mullane, H. P. Summers, Z. Altun, M. A. Bautista, J. Colgan, T. W. Gorczyca, D. M. Mitnik, M. S. Pindzola, and O. Zatsarinny, *Dielectronic recombination data for dynamic finite-density plasmas: I. Goals and methodology*, Astronomy & Astrophysics, 406 (2003), pp. 1151–1165, doi:10.1051/0004-6361:20030816.

[13] D. S. Balsara, *Second-order-accurate schemes for magnetohydrodynamics with divergence-free reconstruction*, The Astrophysical Journal Supplement Series, 151 (2004), p. 149.

[14] J. Banks and J. Shadid, *An euler system source term that develops prototype z-pinch implosions intended for the evaluation of shock-hydro methods*, International journal for numerical methods in fluids, 61 (2009), pp. 725–751.

[15] C. F. BARNETT, *Atomic data for fusion – Volume 1: Collisions of H, H2, He, and Li atoms and ions with atoms and molecules*, Tech. Report ORNL-6086/V1, Oak Ridge National Laboratory, Oak Ridge, TN, 1990.

[16] M. A. BAUTISTA AND N. R. BADNELL, *Dielectronic recombination data for dynamic finite-density plasmas: XII. The helium isoelectronic sequence*, Astronomy & Astrophysics, 466 (2007), pp. 755–762, doi:10.1051/0004-6361:20077056.

[17] M. T. BETTENCOURT, J. J. BOERNER, P. S. CROZIER, A. S. FIERRO, A. M. GRILLET, R. W. HOOPER, M. M. HOPKINS, T. P. HUGHES, H. E. MEYER, C. H. MOORE, S. G. MOORE, L. C. MUSSON, AND J. L. PACHECO, *Aleph manual*, Tech. Report SAND-2017-10343, Sandia National Laboratories, 2016.

[18] J. A. BITTENCOURT, *Fundamentals of Plasma Physics*, Springer New York, 2004.

[19] P. BOCHEV, H. C. EDWARDS, R. C. KIRBY, K. PETERSON, AND D. RIDZAL, *Solving PDEs with Intrepid*, Scientific Programming, 20 (2012), pp. 151–180.

[20] P. BOCHEV AND J. HYMAN, *Principles of mimetic discretizations of differential operators*, Compatible spatial discretizations, (2006), pp. 89–119.

[21] P. B. BOCHEV AND A. C. ROBINSON, *Matching algorithms with physics: exact sequences of finite element spaces*, Collected Lectures on Preservation of Stability Under Discretization, (2002), pp. 145–166.

[22] S. BOSCARINO, L. PARESCHI, AND G. RUSSO, *Implicit-explicit runge–kutta schemes for hyperbolic systems and kinetic equations in the diffusion limit*, SIAM Journal on Scientific Computing, 35 (2013), pp. A22–A51, doi:10.1137/110842855, `https://doi.org/10.1137/110842855`, arXiv:https://doi.org/10.1137/110842855.

[23] T. BOYD, T. BOYD, AND J. SANDERSON, *The physics of plasmas*, Cambridge University Press, 2003.

[24] S. I. BRAGINSKII, *Transport processes in a plasma*, Reviews of plasma physics, 1 (1965), p. 205.

[25] P. N. BROWN AND Y. SAAD, *Convergence theory of nonlinear Newton–Krylov algorithms*, SIAM J. Optimization, 4 (1994), pp. 297–330.

[26] J. CARPENTER, N. BELCOURT, AND R. NOURGALIEV, *General purpose steam table library: CASL L3:THM.CFD.P7.04 milestone report*, Tech. Report SAND-2013-7328, Sandia National Laboratories, 2013.

[27] J. H. CHAUDHRY, D. ESTEP, V. GINTING, J. N. SHADID, AND S. TAVENER, *A posteriori error analysis of imex multi-step time integration methods for advection–diffusion–reaction equations*, Computer Methods in Applied Mechanics and Engineering, 285 (2015), pp. 730–751.

[28] E. CLEMENTI, D. L. RAIMONDI, AND W. P. REINHARDT, *Atomic screening constants from SCF functions. II. Atoms with 37 to 86 electrons*, The Journal of Chemical Physics, 47 (1967), pp. 1300–1307, doi:10.1063/1.1712084.

[29] J. COLGAN, M. S. PINDZOLA, AND N. R. BADNELL, *Dielectronic recombination data for dynamic finite-density plasmas: V. The lithium isoelectronic sequence*, Astronomy & Astrophysics, 417 (2004), pp. 1183–1188, doi:10.1051/0004-6361:20034197.

[30] J. COLGAN, M. S. PINDZOLA, AND N. R. BADNELL, *Erratum to: Dielectronic recombination data for dynamic finite-density plasmas: V. The lithium isoelectronic sequence*, Astronomy & Astrophysics, 429 (2005), pp. 369–369, doi:10.1051/0004-6361:20042105.

[31] J. COLGAN, M. S. PINDZOLA, A. D. WHITEFORD, AND N. R. BADNELL, *Dielectronic recombination data for dynamic finite-density plasmas: III. The beryllium isoelectronic sequence*, Astronomy & Astrophysics, 412 (2003), pp. 597–601, doi:10.1051/0004-6361:20031362.

[32] S. CONDE, I. FEKETE, AND J. N. SHADID, *Embedded error estimation and adaptive step-size control for optimal explicit strong stability preserving Runge–Kutta methods*, arXiv e-prints, (2018), arXiv:1806.08693, arXiv:1806.08693.

[33] S. CONDE, S. GOTTLIEB, Z. J. GRANT, AND J. N. SHADID, *Implicit and implicit–explicit strong stability preserving runge–kutta methods with high linear order*, Journal of Scientific Computing, 73 (2017), pp. 667–690, doi:10.1007/s10915-017-0560-2, https://doi.org/10.1007/s10915-017-0560-2.

[34] E. C. CYR, J. N. SHADID, AND R. S. TUMINARO, *Teko: A Block Preconditioning Capability with Concrete Applications in Navier-Stokes and MHD*, SIAM J. Sci. Comput., 38 (2016), pp. S307–S331.

[35] A. DEDNER, F. KEMM, D. KRÖNER, C. D. MUNZ, T. SCHNITZER, AND M. WESENBERG, *Hyperbolic divergence cleaning for the MHD equations*, Journal of Computational Physics, 175 (2002), pp. 645–673, doi:10.1006/jcph.2001.6961.

[36] R. S. DEMBO, S. C. EISENSTAT, AND T. STEIHAUG, *Inexact Newton methods*, SIAM J. Numer. Anal., 19 (1982), pp. 400–408.

[37] J. E. DENNIS, JR. AND R. B. SCHNABEL, *Numerical Methods for Unconstrained Optimization and Nonlinear Equations*, Series in Automatic Computation, Prentice-Hall, Englewood Cliffs, NJ, 1983.

[38] M. DESJARLAIS, *Practical improvements to the lee-more conductivity near the metal-insulator transition*, Contributions in Plasma Physics, 41 (2001), pp. 267–270.

[39] A. S. DICKINSON, M. S. LEE, AND L. A. VIEHLAND, *The mobility of He^+ ions in helium gas*, Journal of Physics B: Atomic, Molecular and Optical Physics, 32 (1999), pp. 4919–4930, doi:10.1088/0953-4075/32/20/309.

[40] S. C. EISENSTAT AND H. F. WALKER, *Globally convergent inexact Newton methods*, SIAM J. Optimization, 4 (1994), pp. 393–422.

[41] S. C. EISENSTAT AND H. F. WALKER, *Choosing the forcing terms in an inexact Newton method*, SIAM J. Sci. Comput., 17 (1996), pp. 16–32.

[42] W. L. FITE, A. C. H. SMITH, AND R. F. STEBBINGS, *Charge transfer in collisions involving symmetric and asymmetric resonance*, Proceedings of the Royal Society A: Mathematical, Physical and Engineering Sciences, 268 (1962), pp. 527–536, doi:10.1098/rspa.1962.0156.

[43] J. GAIDAMOUR, J. HU, C. SIEFERT, AND R. TUMINARO, *Design considerations for a flexible multigrid preconditioning library*, Scientific Programming, 20 (3) (2012), pp. 223–239.

[44] S. GOTTLIEB, D. KETCHESON, AND C. SHU, *Strong Stability Preserving Runge-Kutta and Multistep Time Discretizations*, World Scientific, 2011, https://books.google.com/books?id=MHmAINTBIkQC.

[45] M. F. GU, *Radiative recombination rate coefficients for bare through F-like isosequences of Mg, Si, S, Ar, Ca, Fe, and Ni*, The Astrophysical Journal, 589 (2003), pp. 1085–1088, doi:10.1086/374796.

[46] M. A. HEROUX, R. A. BARTLETT, V. E. HOWLE, R. J. HOEKSTRA, J. J. HU, T. G. KOLDA, R. B. LEHOUCQ, K. R. LONG, R. P. PAWLOWSKI, E. T. PHIPPS, A. G. SALINGER, H. K. THORNQUIST, R. S. TUMINARO, J. M. WILLENBRING, A. WILLIAMS, AND K. S. STANLEY, *An overview of the trilinos project*, ACM Trans. Math. Softw., 31 (2005), pp. 397–423, doi:10.1145/1089014.1089021, http://doi.acm.org/10.1145/1089014.1089021.

[47] I. HIGUERAS, *Strong stability for additive rungeâĂŞkutta methods*, SIAM Journal on Numerical Analysis, 44 (2006), pp. 1735–1758, doi:10.1137/040612968, https://doi.org/10.1137/040612968, arXiv:https://doi.org/10.1137/040612968.

[48] I. HIGUERAS, *Characterizing strong stability preserving additive runge-kutta methods*, Journal of Scientific Computing, 39 (2009), pp. 115–128, doi:10.1007/s10915-008-9252-2, https://doi.org/10.1007/s10915-008-9252-2.

[49] I. HIGUERAS, N. HAPPENHOFER, O. KOCH, AND F. KUPKA, *Optimized strong stability preserving imex rungeâĂŞkutta methods*, Journal of Computational and Applied Mathematics, 272 (2014), pp. 116 – 140, doi:https://doi.org/10.1016/j.cam.2014.05.011, http://www.sciencedirect.com/science/article/pii/S0377042714002477.

[50] F. L. HINTON, *Collisional transport in plasma*, Handbook of Plasma Physics, 1 (1983), p. 147.

[51] W. HUNDSDORFER AND S. J. RUUTH, *Imex extensions of linear multistep methods with general monotonicity and boundedness properties*, Journal of Computational Physics, 225 (2007), pp. 2016–2042.

[52] W. HUNDSDORFER AND S. J. RUUTH, *Imex extensions of linear multistep methods with general monotonicity and boundedness properties*, J. Comput. Phys., 225 (2007), pp. 2016–2042, doi:10.1016/j.jcp.2007.03.003, http://dx.doi.org/10.1016/j.jcp.2007.03.003.

[53] C. A. JENNINGS, M. E. CUNEO, E. WAISMAN, D. SINARS, D. AMPLEFORD, G. BENNETT, W. STYGAR, AND J. CHITTENDEN, *Simulations of the implosion and stagnation of compact wire arrays*, Physics of Plasmas, 17 (2010), p. 092703.

[54] B. JONES, C. A. JENNINGS, D. C. LAMPPA, S. B. HANSEN, A. J. HARVEY-THOMPSON, D. J. AMPLEFORD, M. E. CUNEO, T. STRIZIC, D. JOHNSON, M. C. JONES, N. W. MOORE, T. M. FLANAGAN, J. L. MCKENNEY, E. M. WAISMAN, C. A. COVERDALE, M. KRISHNAN, P. L. COLEMAN, K. W. ELLIOT, R. E. MADDEN, J. THOMPSON, A. BIXLER, J. W. THORNHILL, J. L. GIULIANI, Y. K. CHONG, A. L. VELIKOVICH, A. DASGUPTA, AND J. P. APRUZESE, *A Renwed Capability for Gas Puff Science on Sandia's Z Machine*, IEEE Transactions on Plasma Science, 42 (2013), pp. 1145–1152, doi:10.1109/TPS.2013.2287180.

[55] J. KAUR, T. W. GORCZYCA, AND N. R. BADNELL, *Dielectronic recombination data for dynamic finite-density plasmas: XV. The silicon isoelectronic sequence*, Astronomy & Astrophysics, 610 (2018), p. A41, doi:10.1051/0004-6361/201731243.

[56] I. A. KOTELNIKOV AND A. I. MILSTEIN, *Electron radiative recombination with a hydrogen-like ion*, Physica Scripta, 94 (2019), p. 055403, doi:10.1088/1402-4896/ab060a.

[57] J. F. B. M. KRAAIJEVANGER, *Contractivity of runge-kutta methods*, BIT Numerical Mathematics, 31 (1991), pp. 482–528, doi:10.1007/BF01933264, https://doi.org/10.1007/BF01933264.

[58] KRAMER, MCGREGOR, ROBINSON, SHADID, PHILLIPS, AND GARDINER, *On a continuum plasma modeling hierarchy*, Tech. Report in preparation, Sandia National Laboratories, 2018.

[59] KRAMER, ROBINSON, PHILLIPS, SHADID, AND CYR, *Plasma model hierarchies and numerical methods for next generation architectures and production usability*, Tech. Report in preparation, Sandia National Laboratories, 2016.

[60] H. KUMAR AND S. MISHRA, *Entropy stable numerical schemes for two-fluid plasma equations*, Journal of Scientific Computing, 52 (2012), pp. 401–425, doi:10.1007/s10915-011-9554-7, https://doi.org/10.1007/s10915-011-9554-7.

[61] F. KUPKA, N. HAPPENHOFER, I. HIGUERAS, AND O. KOCH, *Total-variation-diminishing implicitâĂŞexplicit rungeâĂŞkutta methods for the simulation of double-diffusive convection in astrophysics*, Journal of Computational Physics, 231 (2012), pp. 3561 – 3586, doi:https://doi.org/10.1016/j.jcp.2011.12.031, http://www.sciencedirect.com/science/article/pii/S0021999111007522.

[62] D. KUZMIN, M. MOLLER, AND S. TUREK, *High resolution FEM-FCT schemes for multidimensional conservation laws*, Comput. Meth. Appl. Mech. Engrg., 193 (2004), pp. 4915–4946.

[63] D. KUZMIN AND J. N. SHADID, *Gradient-based nodal limiters for artificial diffusion operators in finite element schemes for transport equations*, International Journal for Numerical Methods in Fluids, 84 (2017), pp. 675–695.

[64] D. KUZMIN, M. J. SHASHKOV, AND D. SVYATSKIY, *A constrained finite element method satisfying the discrete maximum principle for anisotropic diffusion problems*, Journal of Computational Physics, 228 (2009), pp. 3448–3463.

[65] D. KUZMIN AND S. TUREK, *Explicit and implicit high-resolution finite element schemes based on the Flux-Corrected-Transport algorithm,*, in F. Brezzi et. al. (Eds.), Proceedings of the 4th European Conference on Numerical Mathematics and Advances Applications, Springer-Verlag (2002), pp. 133–143.

[66] M. LANDINI AND B. C. MONSIGNORI FOSSI, *The X-UV spectrum of thin plasmas*, Astronomy & Astrophysics Supplement Series, 82 (1990), pp. 229–260.

[67] M. LANDINI AND B. C. MONSIGNORI FOSSI, *Ion equilibrium for minor components in a thin plasma*, Astronomy & Astrophysics Supplement Series, 91 (1991), pp. 183–196.

[68] Y. LEE AND R. MORE, *An electron conductivity model for dense plasmas*, The Physics of Fluids, 27 (1984), pp. 1273–1286.

[69] N. R. LEWKOW, V. KHARCHENKO, AND P. ZHANG, *Energy relaxation of helium atoms in astrophysical gases*, The Astrophysical Journal, 756 (2012), p. 57, doi:10.1088/0004-637X/756/1/57.

[70] P. T. LIN, M. SALA, J. N. SHADID, AND R. S. TUMINARO, *Performance of a geometric and an algebraic multilevel preconditioner for incompressible flow and transport*, in Computational Mechanics: WCCM VI in conjunction with APCOM'04, Tsinghus Univ. Press, Springer-Verlag, 2004.

[71] P. T. LIN, M. SALA, J. N. SHADID, AND R. S. TUMINARO, *Performance of fully-coupled algebraic multilevel domain decomposition preconditioners for incompressible flow and transport*, Int. J. Num. Meth. Eng., 67 (2006), pp. 208–225.

[72] P. T. LIN, J. N. SHADID, J. J. HU, R. P. PAWLOWSKI, AND E. C. CYR, *Performance of fully-coupled algebaric multigrid preconditioners for large-scale vms resistive mhd*, Submitted to J. Comp. and Applied Math, (2017).

[73] P. T. LIN, J. N. SHADID, J. J. HU, R. P. PAWLOWSKI, AND E. C. CYR, *Performance of fully-coupled algebraic multigrid preconditioners for large-scale vms resistive mhd*, Journal of Computational and Applied Mathematics, 344 (2018), pp. 782–793.

[74] P. T. LIN, J. N. SHADID, R. S. TUMINARO, AND M. SALA, *Performance of a petrov-galerkin algebraic multilevel preconditioner for finite element modeling of the semiconductor device drift-diffusion equations*, Int. J. Num. Meth. Eng., 84 (2010), pp. 448–469.

[75] P. T. LIN, J. N. SHADID, R. S. TUMINARO, M. SALA, G. L. HENNIGAN, AND R. P. PAWLOWSKI, *A parallel fully-coupled algebraic multilevel preconditioner applied to multiphysics PDE applications: Drift-diffusion, flow/transport/reaction, resistive MHD*, Int. J. Num. Meth. Fluids, 64 (2010), pp. 1148–1179.

[76] W. LOTZ, *Electron-impact ionization cross-sections and ionization rate coefficients for atoms and ions from hydrogen to calcium*, Zeitschrift für Physik, 216 (1968), pp. 241–247, doi:10.1007/BF01392963.

[77] W. LOTZ, *Electron-impact ionization cross-sections and ionization rate coefficients for atoms and ions from scandium to zinc*, Zeitschrift für Physik, 220 (1969), pp. 466–472, doi:10.1007/BF01394789.

[78] J. LOVERICH, A. HAKIM, AND U. SHUMLAK, *A discontinuous galerkin method for ideal two-fluid plasma equations*, Communications in Computational Physics, 9 (2011), pp. 240–268.

[79] J. LOVERICH AND U. SHUMLAK, *Nonlinear full two-fluid study of m= 0 sausage instabilities in an axisymmetric z pinch*, Physics of Plasmas, 13 (2006), p. 082310.

[80] S. Lyon and J. e. Johnson, *Sesame: The los alamos national laboratory equation of state database*, Tech. Report LA-UR-92-3407, Los Alamos National Laboratory, 1992.

[81] S. Mabuza, J. Shadid, E. Cyr, R. Pawlowski, and D. Kuzmin, *A positivity and linearity preserving nodal variation limiting algorithm for continuous Galerkin discretization of ideal MHD equations*.

[82] S. Mabuza, J. Shadid, and D. Kuzmin, *Local bounds preserving stabilization for continuous Galerkin discretization of hyperbolic systems*, Journal of Computational Physics, 361 (2018), doi:10.1016/j.jcp.2018.01.048.

[83] D. Martínez-Gómez, R. Soler, and J. Terradas, *Multi-fluid approach to high-frequency waves in plasmas. I. Small-amplitude regime in fully ionized media*, The Astrophysical Journal, 832 (2016), p. 101, doi:10.3847/0004-637X/832/2/101.

[84] D. Martínez-Gómez, R. Soler, and J. Terradas, *Multi-fluid approach to high-frequency waves in plasmas. II. Small-amplitude regime in partially ionized media*, The Astrophysical Journal, 837 (2017), p. 80, doi:10.3847/1538-4357/aa5eab.

[85] E. Meier, V. Lukin, and U. Shumlak, *Spectral element spatial discretization error in solving highly anisotropic heat conduction equation*, Computer Physics Communications, 181 (2010), pp. 837–841.

[86] E. Meier and U. Shumlak, *A general nonlinear fluid model for reacting plasma-neutral mixtures*, Physics of Plasmas, 19 (2012), p. 072508, doi:10.1063/1.4736975.

[87] E. T. Meier, *Modeling Plasmas with Strong Anisotropy, Neutral Fluid Effects, and Open Boundaries*, PhD thesis, University of Washington, 2011.

[88] E. T. Meier and U. Shumlak, *A general nonlinear fluid model for reacting plasma-neutral mixtures*, Physics of Plasmas, 19 (2012), p. 072508.

[89] S. Miller, E. Cyr, J. Shadid, R. Kramer, E. Phillips, S. Conde, and R. Pawlowski, *Imex and exact sequence discretization of the multi-fluid plasma model*, Journal of Computational Physics, 397 (2019), p. 108806.

[90] D. M. Mitnik and N. R. Badnell, *Dielectronic recombination data for dynamic finite-density plasmas: VIII. The nitrogen isoelectronic sequence*, Astronomy & Astrophysics, 425 (2004), pp. 1153–1159, doi:10.1051/0004-6361:20041297.

[91] R. J. Moreau, *Magnetohydrodynamics*, Fluid Mechanics and Its Applications, Springer Netherlands, 1990.

[92] M. F. Murphy, G. H. Golub, and A. J. Wathen, *A note on preconditioning for indefinite linear systems*, SIAM J. Sci. Comput., 21 (2000), pp. 1969–1972.

[93] D. Nikolić, T. W. Gorczyca, K. T. Korista, M. Chatzikos, G. J. Ferland, F. Guzmán, P. A. M. van Hoof, R. J. R. Williams, and N. R. Badnell, *Suppression of dielectronic recombination due to finite density effects. II. Analytical refinement and application to density-dependent ionization balances and AGN broad-line emission*, The Astrophysical Journal Supplement Series, 237 (2018), p. 41, doi:10.3847/1538-4365/aad3c5.

[94] D. Nikolić, T. W. Gorczyca, K. T. Korista, G. J. Ferland, and N. R. Badnell, *Suppression of dielectronic recombination due to finite density effects*, The Astrophysical Journal, 768 (2013), p. 82, doi:10.1088/0004-637X/768/1/82.

[95] P. K. Notz, R. P. Pawlowski, and J. C. Sutherland, *Graph-based software design for managing complexity and enabling concurrency in multiphysics PDE software*, ACM Trans. Math Softw., 39 (2012), pp. 1:1–1:21, `http://doi.acm.org/10.1145/2382585.2382586`.

[96] L. Pareschi and G. Russo, *Recent trends in numerical analysis*, (2000), pp. 269–288, http://dl.acm.org/citation.cfm?id=380227.380258.

[97] L. Pareschi and G. Russo, *Implicit–explicit runge–kutta schemes and applications to hyperbolic systems with relaxation*, Journal of Scientific computing, 25 (2005), pp. 129–155.

[98] L. Pareschi and G. Russo, *Implicit–explicit runge–kutta schemes and applications to hyperbolic systems with relaxation*, Journal of Scientific Computing, 25 (2005), pp. 129–155, doi:10.1007/s10915-004-4636-4, https://doi.org/10.1007/s10915-004-4636-4.

[99] M. Parsani, D. Ketcheson, and W. Deconinck, *Optimized explicit runge–kutta schemes for the spectral difference method applied to wave propagation problems*, SIAM Journal on Scientific Computing, 35 (2013), pp. A957–A986, doi:10.1137/120885899, https://doi.org/10.1137/120885899, arXiv:https://doi.org/10.1137/120885899.

[100] H. Pauls, G. Zank, and L. Williams, *Interaction of the solar wind with the local interstellar medium*, Journal of Geophysical Research, 100 (1995), pp. 21595–21604, doi:10.1029/95JA02023.

[101] R. P. Pawlowski, E. T. Phipps, and A. G. Salinger, *Automating embedded analysis capabilities and managing software complexity in multiphysics simulation, part I: Template-based gen eric programming*, Scientific Programming, 20 (2012), pp. 197–219.

[102] R. P. Pawlowski, E. T. Phipps, A. G. Salinger, S. J. Owen, C. M. Siefert, and M. L. Staten, *Automating embedded analysis capabilities and managing software complexity in multiphysics simulation, part II: Application to pa rtial differential equations*, Scientific Programming, 20 (2012), pp. 327–345.

[103] R. P. Pawlowski, J. N. Shadid, J. P. Simonis, and H. F. Walker, *Globalization techniques for newton–krylov methods and applications to the fully coupled solution of the navier–stokes equations*, SIAM review, 48 (2006), pp. 700–721.

[104] E. G. Phillips, J. N. Shadid, and E. C. Cyr, *Scalable preconditioners for structure preserving discretizations of Maxwell equations in first order form*, In Preparation, (2017).

[105] E. G. Phillips, J. N. Shadid, and E. C. Cyr, *Scalable preconditioners for structure preserving discretizations of maxwell equations in first order form*, SIAM Journal on Scientific Computing, 40 (2018), pp. B723–B742.

[106] E. G. Phillips, J. N. Shadid, E. C. Cyr, and S. T. Miller, *Enabling scalable multifluid plasma simulations through block preconditioning*, Lecture Notes in Science and Engineering, In press (2019).

[107] A. Robinson, M. Swan, R. Hooper, T. Smith, R. R. Drake, and N. Bennett, *Neutral expansion exact solutions for plasma code verification*, Tech. Report SAND-2019-8612A, Sandia National Laboratories, 2016.

[108] C. Roedig, O. Zanotti, and D. Alic, *General relativistic radiation hydrodynamics of accretion flows–ii. treating stiff source terms and exploring physical limitations*, Monthly Notices of the Royal Astronomical Society, 426 (2012), pp. 1613–1631.

[109] A. Rohde, *Eigenvalues and eigenvectors of the Euler equations in general geometries*, AIAA, 1 (1999), p. 1, http://www.microcfd.com/download/pdf/aiaa2001-2609.pdf.

[110] S. J. Ruuth and R. J. Spiteri, *Two barriers on strong-stability-preserving time discretization methods*, Journal of Scientific Computing, 17 (2002), pp. 211–220, doi:10.1023/A:1015156832269, https://doi.org/10.1023/A:1015156832269.

[111] M. Sala, J. N. Shadid, and R. S. Tuminaro, *An improved convergence bound for aggregation-based domain decomposition preconditioners*, SIAM J. Matrix Analysis, 27 (2006), pp. 744–756.

[112] M. SALA AND R. TUMINARO, *A new Petrov-Galerkin smoothed aggregation preconditioner for nonsymmetric linear systems*, SIAM J. Sci. Stat., 31 (2008), pp. 143–166.

[113] A. SANDU AND M. GÃIJNTHER, *A generalized-structure approach to additive runge–kutta methods*, SIAM Journal on Numerical Analysis, 53 (2015), pp. 17–42, doi:10.1137/130943224, https://doi.org/10.1137/130943224, arXiv:https://doi.org/10.1137/130943224.

[114] R. SCHUNK, *Mathematical structure of transport equations for multispecies flows*, Reviews of Geophysics, 15 (1977), pp. 429–445, doi:10.1029/RG015i004p00429.

[115] J. N. SHADID, R. P. PAWLOWSKI, J. W. BANKS, L. CHACÓN, P. T. LIN, AND R. S. TUMINARO, *Towards a scalable fully-implicit fully-coupled resistive mhd formulation with stabilized fe methods*, Journal of Computational Physics, 229 (2010), pp. 7649–7671.

[116] J. N. SHADID, R. P. PAWLOWSKI, E. C. CYR, R. S. TUMINARO, L. CHACON, AND P. D. WEBER, *Scalable implicit incompressible resistive mhd with stabilized fe and fully-coupled newton–krylov-amg*, Computer Methods in Applied Mechanics and Engineering, 304 (2016), pp. 1–25.

[117] J. N. SHADID, R. P. PAWLOWSKI, E. C. CYR, R. S. TUMINARO, L. CHACON, AND P. D. WEBER, *Scalable Implicit Incompressible Resistive MHD with Stabilized FE and Fully-coupled Newton-Krylov-AMG*, Comput. Methods Appl. Mech. Engrg., 304 (2016), pp. 1–25.

[118] J. N. SHADID, R. S. TUMINARO, AND H. F. WALKER, *An inexact Newton method for fully-coupled solution of the Navier–Stokes equations with heat and mass transport*, J. Comput. Phys., 137 (1997), pp. 155–185.

[119] C. SHU, *Total-variation-diminishing time discretizations*, SIAM Journal on Scientific and Statistical Computing, 9 (1988), pp. 1073–1084, doi:10.1137/0909073, https://doi.org/10.1137/0909073, arXiv:https://doi.org/10.1137/0909073.

[120] U. SHUMLAK AND J. LOVERICH, *Approximate riemann solver for the two-fluid plasma model*, Journal of Computational Physics, 187 (2003), pp. 620–638.

[121] S. SLUTZ, M. HERRMANN, R. VESEY, A. SEFKOW, D. SINARS, D. ROVANG, K. PETERSON, AND M. CUNEO, *Pulsed-power-driven cylindrical liner implosions of laser preheated fuel magnetized with an axial field*, Physics of Plasmas, 17 (2010), p. 056303.

[122] E. SOUSA AND U. SHUMLAK, *A blended continuous-discontinuous finite element method for solving the multi-fluid plasma model*, Journal of Computational Physics, 326 (2016).

[123] E. SOUSA AND U. SHUMLAK, *A blended continuousâĂŞdiscontinuous finite element method for solving the multi-fluid plasma model*, Journal of Computational Physics, 326 (2016), pp. 56 – 75, doi:https://doi.org/10.1016/j.jcp.2016.08.044, http://www.sciencedirect.com/science/article/pii/S0021999116304016.

[124] B. SRINIVASAN AND U. SHUMLAK, *Analytical and computational study of the ideal full two-fluid plasma model and asymptotic approximations for hall-magnetohydrodynamics*, Physics of Plasmas, 18 (2011), p. 092113.

[125] T. STIX, *Waves in plasmas*, Amer Inst of Physics, New York, 1992.

[126] R. TUMINARO, C. TONG, J. SHADID, K.D.DEVINE, AND D. DAY, *On a multilevel preconditioning module for unstructured mesh Krylov solvers: two-level schwarz*, Comm. Num. Method. Eng., 18 (2002), pp. 383–389.

[127] D. A. VERNER AND G. J. FERLAND, *Atomic data for astrophysics. I. Radiative recombination rates for H-like, He-like, Li-like, and Na-like ions over a broad range of temperature*, The Astrophysical Journal Supplement Series, 103 (1996), p. 467, doi:10.1086/192284.

[128] G. VORONOV, *A practical fit formula for ionization rate coefficients of atoms and ions by electron impact: z = 1-28*, Atomic Data and Nuclear Data Tables, 65 (1997), pp. 1–35, doi:10.1006/adnd.1997.0732.

[129] J. VRANJES AND P. S. KRSTIC, *Collisions, magnetization, and transport coefficients in the lower solar atmosphere*, Astronomy & Astrophysics, 554 (2013), p. A22, doi:10.1051/0004-6361/201220738.

[130] O. ZATSARINNY, T. W. GORCZYCA, J. FU, K. T. KORISTA, N. R. BADNELL, AND D. W. SAVIN, *Dielectronic recombination data for dynamic finite-density plasmas: IX. The fluorine isoelectronic sequence*, Astronomy & Astrophysics, 447 (2006), pp. 379–387, doi:10.1051/0004-6361:20053737.

[131] O. ZATSARINNY, T. W. GORCZYCA, K. KORISTA, N. R. BADNELL, AND D. W. SAVIN, *Dielectronic recombination data for dynamic finite-density plasmas: VII. The neon isoelectronic sequence*, Astronomy & Astrophysics, 426 (2004), pp. 699–705, doi:10.1051/0004-6361:20040463.

[132] O. ZATSARINNY, T. W. GORCZYCA, K. T. KORISTA, N. R. BADNELL, AND D. W. SAVIN, *Dielectronic recombination data for dynamic finite-density plasmas: II. The oxygen isoelectronic sequence*, Astronomy & Astrophysics, 412 (2003), pp. 587–595, doi:10.1051/0004-6361:20031462.

[133] O. ZATSARINNY, T. W. GORCZYCA, K. T. KORISTA, N. R. BADNELL, AND D. W. SAVIN, *Dielectronic recombination data for dynamic finite-density plasmas: IV. The carbon isoelectronic sequence*, Astronomy & Astrophysics, 417 (2004), pp. 1173–1181, doi:10.1051/0004-6361:20034174.

[134] H. ZHANG, A. SANDU, AND S. BLAISE, *Partitioned and implicit–explicit general linear methods for ordinary differential equations*, Journal of Scientific Computing, 61 (2014), pp. 119–144, doi:10.1007/s10915-014-9819-z, https://doi.org/10.1007/s10915-014-9819-z.

[135] E. ZHAROVSKY, A. SANDU, AND H. ZHANG, *A class of implicit-explicit two-step runge–kutta methods*, SIAM Journal on Numerical Analysis, 53 (2015), pp. 321–341, doi:10.1137/130937883, https://doi.org/10.1137/130937883, arXiv:https://doi.org/10.1137/130937883.

APPENDIX A. NOTATION

A.1. Notation Used in Discussion

The following notations are assumed throughout:

1. When used as a subscript, the symbol e will be used to denote quantities associated with the electron species.

2. N_A denotes the number of atomic species, which are indexed by $\alpha, \beta \in \{1, \ldots, N_A\}$.

3. z_α denotes the maximum tracked charge state of atomic species α. We note that this value may be different than the maximum charge state $z_\alpha^{\max}$ for the species; ie., $0 < z_\alpha \leq z_\alpha^{\max}$.

4. An ordered pair (α, k) will be used to denote associations with neutrals ($k = 0$) or ions ($k > 0$) of atomic species α with charge state k. We assume always that $k \geq 0$.

5. $\mathcal{N}_S \stackrel{\text{def}}{=} \{(\alpha, k) : \alpha = 1, \ldots, N_A; k = 0, \ldots, z_\alpha\}$ is the set of all neutral and ion species.

6. Standard non-bold fonts will be used for scalar quantities in $\mathbb{R}$.

7. Bold fonts will be used for vector quantities in $\mathbb{R}^3$ (eg., $\mathbf{v}$ for velocity).

8. Bold fonts with a single underline will be used for second-order tensors in $\mathbb{R}^3 \otimes \mathbb{R}^3$ (eg., $\underline{\mathbf{\Pi}}$ for shear stress).

9. An exponent applied to a vector quantity will be used to denote the dot product of that quantity with itself; ie., $\mathbf{v}^2 = \mathbf{v} \cdot \mathbf{v}$.

10. Quantities associated with a particle species s will be denoted as follows:

m_s	particle mass	p_s	scalar pressure
n_s	number density	$\underline{\mathbf{\Pi}}_s$	shear stress
ρ_s	mass density	$\mathcal{E}_s$	total energy
q_s	electric charge	e_s	specific internal energy
Z_s	signed charge number	$\mathbf{h}_s$	heat flux
$\mathbf{u}_s$	average fluid velocity	T_s	temperature

    These quantities satisfy the following relations:

$$\rho_s = m_s n_s, \qquad \mathcal{E}_s = \frac{1}{2}\rho_s \mathbf{u}_s^2 + \rho_s e_s,$$
$$q_s = -Z_s q_e.$$

11. The following constants are used:

    a) k_{B} is the Boltzmann constant.

    b) ϵ_0 is the vacuum electrical permittivity.

    c) q_e is the (negative) elementary electric charge; ie., the charge of one electron.

APPENDIX B. MULTIFLUID MODELS WITH AVERAGED HEAVY SPECIES DYNAMICS

We now consider reduced multifluid models in which certain sets of charge states for each species are combined into a single fluid representation.

B.1. Neutral, Averaged Ion Model Description

In the first model, the separate fluid equations for the individual ion charge states are replaced by a single fluid representing an average ionization state. The electron and neutral equations remain as in Section 3.1, with appropriate modifications to the interaction terms. In the remainder of this section, the subscript (α, i) will be used to denote quantities related to the averaged ionization state for atomic species α.

Define the total ion number and mass densities by

$$n_{(\alpha,i)} \stackrel{\text{def}}{=} \sum_{k=1}^{z_\alpha} n_{(\alpha,k)}, \tag{177a}$$

$$\rho_{(\alpha,i)} \stackrel{\text{def}}{=} \sum_{k=1}^{z_\alpha} \rho_{(\alpha,k)}, \tag{177b}$$

respectively, and define the mean ion velocity $\mathbf{u}_{(\alpha,i)}$ and total ion energy $\mathcal{E}_{(\alpha,i)}$ by

$$\rho_{(\alpha,i)}\mathbf{u}_{(\alpha,i)} \stackrel{\text{def}}{=} \sum_{k=1}^{z_\alpha} \rho_{(\alpha,k)}\mathbf{u}_{(\alpha,k)}, \tag{178a}$$

$$\mathcal{E}_{(\alpha,i)} \stackrel{\text{def}}{=} \sum_{k=1}^{z_\alpha} \mathcal{E}_{(\alpha,k)}. \tag{178b}$$

Defining the average ion charge state $\overline{Z}_{(\alpha,i)}$ by

$$n_{(\alpha,i)}\overline{Z}_{(\alpha,i)} \stackrel{\text{def}}{=} \sum_{k=1}^{z_\alpha} k n_{(\alpha,k)}, \tag{179}$$

the average ion charge is then written as $q_{(\alpha,i)} = -\overline{Z}_{(\alpha,i)} q_e$ and satisfies

$$q_{(\alpha,i)} n_{(\alpha,i)} = \sum_{k=1}^{z_\alpha} q_{(\alpha,k)} n_{(\alpha,k)}. \tag{180}$$

The ionization fractions $\{f_{(\alpha,k)}\}_{k=1}^{z_\alpha}$ and ion mass fractions $\{f^m_{(\alpha,k)}\}_{k=1}^{z_\alpha}$ are defined by

$$f_{(\alpha,k)} \stackrel{\text{def}}{=} \frac{n_{(\alpha,k)}}{n_{(\alpha,i)}}, \tag{181a}$$

$$f^m_{(\alpha,k)} \stackrel{\text{def}}{=} \frac{\rho_{(\alpha,k)}}{\rho_{(\alpha,i)}}, \tag{181b}$$

respectively. If one assumes that $m_e \ll m_{(\alpha,0)}$ and makes the approximation

$$m_\alpha \stackrel{\text{def}}{=} m_{(\alpha,0)} \approx m_{(\alpha,1)} \cdots \approx m_{(\alpha,z_\alpha)}, \tag{182}$$

then it follows that $f^m_{(\alpha,k)} = f_{(\alpha,k)}$ for $k = 1, \ldots, z_\alpha$. Given (181a) and (181b), the number and mass densities of the individual ionization states are given by

$$n_{(\alpha,k)} = f_{(\alpha,k)} n_{(\alpha,i)}, \tag{183a}$$

$$\rho_{(\alpha,k)} = f^m_{(\alpha,k)} \rho_{(\alpha,i)}, \tag{183b}$$

respectively. If one assumes further that the ion drift velocities $\mathbf{w}_{(\alpha,k)} = \mathbf{u}_{(\alpha,k)} - \mathbf{u}_{(\alpha,i)}$ are zero and the ion specific internal energies are all equal (ie., $e_{(\alpha,k)} = e_{(\alpha,i)}$ for $k = 1,\ldots,z_\alpha$), then the momenta and energy densities of the individual ionization states are given by

$$\rho_{(\alpha,k)}\mathbf{u}_{(\alpha,k)} = f^m_{(\alpha,k)}\rho_{(\alpha,i)}\mathbf{u}_{(\alpha,i)}, \tag{183c}$$

$$\mathcal{E}_{(\alpha,k)} = f^m_{(\alpha,k)}\mathcal{E}_{(\alpha,i)}, \tag{183d}$$

respectively. We will assume in the remainder that the approximation (182) is made so that $f_{(\alpha,k)} = f^m_{(\alpha,k)}$ for each k.

Continuity. Summing (4a) with $s = (\alpha,k)$ for $k = 1,\ldots,z_\alpha$ and applying the relations (177b) and (178a) yields the following continuity equation for the total ion mass density:

$$\partial_t \rho_{(\alpha,i)} + \nabla\cdot\left(\rho_{(\alpha,i)}\mathbf{u}_{(\alpha,i)}\right) = \mathcal{C}^{[0]}_{(\alpha,i)} + \mathcal{S}^{[0]}_{(\alpha,i)}, \tag{184}$$

where

$$\mathcal{C}^{[0]}_{(\alpha,i)} \stackrel{\text{def}}{=} \sum_{k=1}^{z_\alpha}\mathcal{C}^{[0]}_{(\alpha,k)} \qquad \text{and} \qquad \mathcal{S}^{[0]}_{(\alpha,i)} \stackrel{\text{def}}{=} \sum_{k=1}^{z_\alpha}\mathcal{S}^{[0]}_{(\alpha,k)}. \tag{185}$$

Summing the contributions due to ionization and recombination reactions, the collision source $\mathcal{C}^{[0]}_{(\alpha,i)}$ can be written explicitly as

$$\mathcal{C}^{[0]}_{(\alpha,i)} = m_\alpha\left(\Gamma^{\text{ion}}_{(\alpha,0)} - \Gamma^{\text{rec}}_{(\alpha,1)}\right). \tag{186}$$

The collision sources $\mathcal{C}^{[0]}_e, \mathcal{C}^{[0]}_{(\alpha,0)}$ remain as in (8).

Momentum. Summing (4b) with $s = (\alpha,k)$ for $k = 1,\ldots,z_\alpha$, assuming the ion drift velocities $\mathbf{w}_{(\alpha,k)}$ are zero, using the relations (178a) and (180), and transforming the system into a reference frame moving with the mean ion velocity $\mathbf{u}_{(\alpha,i)}$ yields

$$\begin{aligned}\partial_t\left(\rho_{(\alpha,i)}\mathbf{u}_{(\alpha,i)}\right) + \nabla\cdot\left(\rho_{(\alpha,i)}\mathbf{u}_{(\alpha,i)}\otimes\mathbf{u}_{(\alpha,i)} + p_{(\alpha,i)}\underline{\mathbf{I}} + \underline{\boldsymbol{\Pi}}_{(\alpha,i)}\right)\\ = q_{(\alpha,i)}n_{(\alpha,i)}\left(\mathbf{E} + \mathbf{u}_{(\alpha,i)}\times\mathbf{B}\right) + \boldsymbol{\mathcal{C}}^{[1]}_{(\alpha,i)} + \boldsymbol{\mathcal{S}}^{[1]}_{(\alpha,i)},\end{aligned} \tag{187}$$

where

$$\boldsymbol{\mathcal{C}}^{[1]}_{(\alpha,i)} \stackrel{\text{def}}{=} \sum_{k=1}^{z_\alpha}\boldsymbol{\mathcal{C}}^{[1]}_{(\alpha,k)} \qquad \text{and} \qquad \boldsymbol{\mathcal{S}}^{[1]}_{(\alpha,i)} \stackrel{\text{def}}{=} \sum_{k=1}^{z_\alpha}\boldsymbol{\mathcal{S}}^{[1]}_{(\alpha,k)}. \tag{188}$$

Summing the contributions of the collision terms for each charge state, the collision source $\boldsymbol{\mathcal{C}}^{[1]}_{(\alpha,i)}$ can be approximated by[4]

$$\boldsymbol{\mathcal{C}}^{[1]}_{(\alpha,i)} = m_\alpha\mathbf{u}_{(\alpha,0)}\Gamma^{\text{ion}}_{(\alpha,0)} - m_\alpha\mathbf{u}_{(\alpha,i)}\Gamma^{\text{rec}}_{(\alpha,1)} + m_e\mathbf{u}_e\sum_{k=2}^{z_\alpha}\Gamma^{\text{rec}}_{(\alpha,k)} + \sum_{s\in\Lambda_{\text{NAI}}\sim(\alpha,i)}\mathbf{R}_{(\alpha,i);s} + \boldsymbol{\mathcal{C}}^{\text{cx},[1]}_{(\alpha,i)}, \tag{189}$$

where

$$\mathbf{R}_{(\alpha,i);e} \stackrel{\text{def}}{=} \sum_{k=1}^{z_\alpha}\mathbf{R}_{(\alpha,k);e}, \qquad \mathbf{R}_{(\alpha,i);(\beta,0)} \stackrel{\text{def}}{=} \sum_{k=1}^{z_\alpha}\mathbf{R}_{(\alpha,k);(\beta,0)}, \qquad \mathbf{R}_{(\alpha,i);(\beta,i)} \stackrel{\text{def}}{=} \sum_{k=1}^{z_\alpha}\sum_{\ell=1}^{z_\beta}\mathbf{R}_{(\alpha,k);(\beta,\ell)}, \tag{190}$$

and

$$\boldsymbol{\mathcal{C}}^{\text{cx},[1]}_{(\alpha,i)} \stackrel{\text{def}}{=} m_\alpha\left(\mathbf{u}_{(\alpha,0)} - \mathbf{u}_{(\alpha,i)}\right)\Gamma^{\text{cx}}_{(\alpha,i)} + \mathbf{R}^{\text{cx}}_{(\alpha,i);(\alpha,0)} - \mathbf{R}^{\text{cx}}_{(\alpha,0);(\alpha,i)}, \tag{191}$$

with

$$\Gamma^{\text{cx}}_{(\alpha,i)} \stackrel{\text{def}}{=} \sum_{k=1}^{z_\alpha}\Gamma^{\text{cx}}_{(\alpha,k)}, \qquad \mathbf{R}^{\text{cx}}_{(\alpha,i);(\alpha,0)} \stackrel{\text{def}}{=} \sum_{k=1}^{z_\alpha}\mathbf{R}^{\text{cx}}_{(\alpha,k);(\alpha,0)}, \qquad \mathbf{R}^{\text{cx}}_{(\alpha,0);(\alpha,i)} \stackrel{\text{def}}{=} \sum_{k=1}^{z_\alpha}\mathbf{R}^{\text{cx}}_{(\alpha,0);(\alpha,k)}. \tag{192}$$

[4] To be consistent with the assumption (182), the third term on the right of (189) can be assumed to be small, and may be neglected in cases where the electron and ion velocities are of a comparable magnitude.

Energy. Summing (4c) with $s = (\alpha, k)$ for $k = 1, \ldots, z_\alpha$, applying the relations (178b) and (180), and transforming the system into a reference frame moving with the mean ion velocity $\mathbf{u}_{(\alpha,i)}$ under the assumption that the individual ion diffusion velocities $\mathbf{w}_{(\alpha,k)}$ are small yields

$$\partial_t \mathcal{E}_{(\alpha,i)} + \nabla \cdot \left[\left(\mathcal{E}_{(\alpha,i)} + p_{(\alpha,i)} \right) \mathbf{u}_{(\alpha,i)} + \mathbf{u}_{(\alpha,i)} \cdot \underline{\mathbf{\Pi}}_{(\alpha,i)} + \mathbf{h}_{(\alpha,i)} \right] = q_{(\alpha,i)} n_{(\alpha,i)} \mathbf{u}_{(\alpha,i)} \cdot \mathbf{E} + \mathcal{C}^{[2]}_{(\alpha,i)} + \mathcal{S}^{[2]}_{(\alpha,i)}, \tag{193}$$

where

$$\mathcal{C}^{[2]}_{(\alpha,i)} \stackrel{\text{def}}{=} \sum_{k=1}^{z_\alpha} \mathcal{C}^{[2]}_{(\alpha,k)} \qquad \text{and} \qquad \mathcal{S}^{[2]}_{(\alpha,i)} \stackrel{\text{def}}{=} \sum_{k=1}^{z_\alpha} \mathcal{S}^{[2]}_{(\alpha,k)}. \tag{194}$$

Summing the contributions of the collision terms for each charge state, the collision source $\mathcal{C}^{[2]}_{(\alpha,i)}$ can be approximated by[5]

$$\begin{aligned} \mathcal{C}^{[2]}_{(\alpha,i)} = &\left(\frac{1}{2} m_\alpha \mathbf{u}^2_{(\alpha,0)} + m_\alpha e_{(\alpha,0)} \right) \Gamma^{\text{ion}}_{(\alpha,0)} - \left(\frac{1}{2} m_\alpha \mathbf{u}^2_{(\alpha,i)} + m_\alpha e_{(\alpha,1)} \right) \Gamma^{\text{rec}}_{(\alpha,1)} \\ &+ \left(\frac{1}{2} m_e \mathbf{u}^2_e + m_e e_e \right) \sum_{k=2}^{z_\alpha} \Gamma^{\text{rec}}_{(\alpha,k)} + \sum_{s \in \Lambda_{\text{NAI}} \smile (\alpha,i)} \left(\mathbf{u}_{(\alpha,i)} \cdot \mathbf{R}_{(\alpha,i);s} + Q_{(\alpha,i);s} \right) + \mathcal{C}^{\text{cx},[2]}_{(\alpha,i)}, \end{aligned} \tag{195}$$

where

$$Q_{(\alpha,i);e} \stackrel{\text{def}}{=} \sum_{k=1}^{z_\alpha} Q_{(\alpha,k);e}, \qquad Q_{(\alpha,i);(\beta,0)} \stackrel{\text{def}}{=} \sum_{k=1}^{z_\alpha} Q_{(\alpha,k);(\beta,0)}, \qquad Q_{(\alpha,i);(\beta,i)} \stackrel{\text{def}}{=} \sum_{k=1}^{z_\alpha} \sum_{\ell=1}^{z_\beta} Q_{(\alpha,k);(\beta,\ell)}, \tag{196}$$

and

$$\begin{aligned} \mathcal{C}^{\text{cx},[2]}_{(\alpha,i)} \stackrel{\text{def}}{=} &\frac{1}{2} m_\alpha \left(\mathbf{u}^2_{(\alpha,0)} - \mathbf{u}^2_{(\alpha,i)} \right) \Gamma^{\text{cx}}_{(\alpha,i)} + \mathbf{u}_{(\alpha,0)} \cdot \mathbf{R}^{\text{cx}}_{(\alpha,i);(\alpha,0)} - \mathbf{u}_{(\alpha,i)} \cdot \mathbf{R}^{\text{cx}}_{(\alpha,0);(\alpha,i)} \\ &+ Q^{\text{cx}}_{(\alpha,i);(\alpha,0)} - Q^{\text{cx}}_{(\alpha,0);(\alpha,i)}, \end{aligned} \tag{197}$$

with $\Gamma^{\text{cx}}_{(\alpha,i)}$, $\mathbf{R}^{\text{cx}}_{(\alpha,i);(\alpha,0)}$ and $\mathbf{R}^{\text{cx}}_{(\alpha,0);(\alpha,i)}$ given by (192), and

$$Q^{\text{cx}}_{(\alpha,i);(\alpha,0)} \stackrel{\text{def}}{=} \sum_{k=1}^{z_\alpha} Q^{\text{cx}}_{(\alpha,k);(\alpha,0)} \qquad \text{and} \qquad Q^{\text{cx}}_{(\alpha,0);(\alpha,i)} \stackrel{\text{def}}{=} \sum_{k=1}^{z_\alpha} Q^{\text{cx}}_{(\alpha,0);(\alpha,k)}. \tag{198}$$

B.2. Fully Averaged Model Description

We now consider a reduced multifluid model wherein the individual ion and neutral states for each atomic species are combined into a single fluid representing an averaged ion-neutral state. In the remainder of this section, the subscript α will be used to denote quantities associated with this average ion-neutral state for atomic species α.

Define the total number and mass densities for species α by

$$n_\alpha \stackrel{\text{def}}{=} \sum_{k=0}^{z_\alpha} n_{(\alpha,k)}, \tag{199a}$$

$$\rho_\alpha \stackrel{\text{def}}{=} \sum_{k=0}^{z_\alpha} \rho_{(\alpha,k)}, \tag{199b}$$

[5] As was the case for the momentum equation, the third term on the right of (195) may be neglected in most cases.

respectively, and define the mean species velocity $\mathbf{u}_\alpha$ and total species energy $\mathcal{E}_\alpha$ by average species charge state $\overline{Z}_\alpha$ by

$$\rho_\alpha \mathbf{u}_\alpha \stackrel{\text{def}}{=} \sum_{k=0}^{z_\alpha} \rho_{(\alpha,k)} \mathbf{u}_{(\alpha,k)}, \tag{200a}$$

$$\mathcal{E}_\alpha \stackrel{\text{def}}{=} \sum_{k=0}^{z_\alpha} \mathcal{E}_{(\alpha,k)}, \tag{200b}$$

respectively. Defining the average species charge state $\overline{Z}_\alpha$ by

$$n_\alpha \overline{Z}_\alpha \stackrel{\text{def}}{=} \sum_{k=0}^{z_\alpha} k n_{(\alpha,k)}, \tag{201}$$

the average species charge is then written as $q_\alpha = -\overline{Z}_\alpha q_e$ and satisfies

$$q_\alpha n_\alpha = \sum_{k=0}^{z_\alpha} q_{(\alpha,k)} n_{(\alpha,k)}. \tag{202}$$

Analogously to the neutral, averaged ion model described in the preceding section, the ionization fractions and mass fractions of the charge states are defined by

$$f_\alpha \stackrel{\text{def}}{=} \frac{n_{(\alpha,k)}}{n_\alpha}, \tag{203a}$$

$$f_\alpha^m \stackrel{\text{def}}{=} \frac{\rho_{(\alpha,k)}}{\rho_\alpha}, \tag{203b}$$

respectively. These values can be used to define quantities such as mass ($\rho_{(\alpha,k)}$), momentum ($\rho_{(\alpha,k)}\mathbf{u}_{(\alpha,k)}$), and energy densities ($\mathcal{E}_{(\alpha,k)}$) for the individual charge states in terms of the aggregated quantities (ie., ρ_α, $\rho_\alpha \mathbf{u}_\alpha$, $\mathcal{E}_\alpha$), as was done before in (183). The approximation (182) is again made for constructing this model.

Continuity. Summing (4a) with $s = (\alpha, k)$ for $k = 0, \ldots, z_\alpha$ and applying the relations (199b) and (200a) yields the following continuity equation for the total species density:

$$\partial_t \rho_\alpha + \nabla \cdot \left(\rho_\alpha \mathbf{u}_\alpha\right) = \mathcal{C}_\alpha^{[0]} + \mathcal{S}_\alpha^{[0]}, \tag{204}$$

where

$$\mathcal{C}_\alpha^{[0]} \stackrel{\text{def}}{=} \sum_{k=0}^{z_\alpha} \mathcal{C}_{(\alpha,k)}^{[0]} \qquad \text{and} \qquad \mathcal{S}_\alpha^{[0]} \stackrel{\text{def}}{=} \sum_{k=0}^{z_\alpha} \mathcal{S}_{(\alpha,k)}^{[0]}. \tag{205}$$

Summing the contributions due to ionization and recombination reactions, the averaged collision source reduces to $\mathcal{C}_\alpha^{[0]} = 0$. The electron collision source $\mathcal{C}_e^{[0]}$ remains as in (8a).

Momentum. As was the case for the average ionization model described in Appendix B.1, we will assume in the remainder of this section that the individual ion and neutral diffusion velocities relative to the mean species velocity $\mathbf{u}_\alpha$ are small, and neglect their contributions. Summing (4b) with $s = (\alpha, k)$ for $k = 0, \ldots, z_\alpha$, applying the relation (200a), and transforming the system into a reference frame moving with the mean species velocity $\mathbf{u}_\alpha$ yields

$$\partial_t \left(\rho_\alpha \mathbf{u}_\alpha\right) + \nabla \cdot \left(\rho_\alpha \mathbf{u}_\alpha \otimes \mathbf{u}_\alpha + p_\alpha \underline{\mathbf{I}} + \underline{\boldsymbol{\Pi}}_\alpha\right) = q_\alpha n_\alpha \left(\mathbf{E} + \mathbf{u}_\alpha \times \mathbf{B}\right) + \boldsymbol{\mathcal{C}}_\alpha^{[1]} + \boldsymbol{\mathcal{S}}_\alpha^{[1]}, \tag{206}$$

where

$$\boldsymbol{\mathcal{C}}_\alpha^{[1]} \stackrel{\text{def}}{=} \sum_{k=0}^{z_\alpha} \boldsymbol{\mathcal{C}}_{(\alpha,k)}^{[1]} \qquad \text{and} \qquad \boldsymbol{\mathcal{S}}_\alpha^{[1]} \stackrel{\text{def}}{=} \sum_{k=0}^{z_\alpha} \boldsymbol{\mathcal{S}}_{(\alpha,k)}^{[1]}. \tag{207}$$

Summing the contributions for each ionization state, whilst noting that the terms due to charge-exchange interactions cancel, the averaged collision source reduces to

$$\mathcal{C}_\alpha^{[1]} = m_e \mathbf{u}_e \Gamma_\alpha^{\mathrm{rec}} + \sum_{s \in \Lambda_{\mathrm{FA}} \backsim \alpha} \mathbf{R}_{\alpha;s}, \tag{208}$$

where

$$\Gamma_\alpha^{\mathrm{rec}} \stackrel{\mathrm{def}}{=} \sum_{k=1}^{z_\alpha} \Gamma_{(\alpha,k)}^{\mathrm{rec}}, \qquad \mathbf{R}_{\alpha;e} \stackrel{\mathrm{def}}{=} \sum_{k=0}^{z_\alpha} \mathbf{R}_{(\alpha,k);e}, \qquad \mathbf{R}_{\alpha;\beta} \stackrel{\mathrm{def}}{=} \sum_{k=0}^{z_\alpha} \sum_{\ell=0}^{z_\alpha} \mathbf{R}_{(\alpha,k);(\beta,\ell)}, \qquad (\beta \neq \alpha). \tag{209}$$

In this case, the collision source $\mathcal{C}_e^{[1]}$ for the electron species can be approximated as

$$\mathcal{C}_e^{[1]} \stackrel{\mathrm{def}}{=} \sum_{\alpha=1}^{N_A} \left(m_e \mathbf{u}_\alpha \Gamma_\alpha^{\mathrm{ion}} - m_e \mathbf{u}_e \Gamma_\alpha^{\mathrm{rec}} + \mathbf{R}_{e;\alpha} \right), \tag{210}$$

where $\Gamma_\alpha^{\mathrm{rec}}$ is given in (209) and

$$\Gamma_\alpha^{\mathrm{ion}} \stackrel{\mathrm{def}}{=} \sum_{k=0}^{z_\alpha - 1} \Gamma_{(\alpha,k)}^{\mathrm{ion}}, \qquad \mathbf{R}_{e;\alpha} \stackrel{\mathrm{def}}{=} \sum_{k=0}^{z_\alpha} \mathbf{R}_{e;(\alpha,k)}. \tag{211}$$

Energy. Summing (4c) with $s = (\alpha, k)$ for $k = 0, \ldots, z_\alpha$, applying the relations (200b) and (202), and transforming the system into a reference frame moving with the mean species velocity $\mathbf{u}_\alpha$ yields

$$\partial_t \mathcal{E}_\alpha + \nabla \cdot \left[\left(\mathcal{E}_\alpha + p_\alpha \right) \mathbf{u}_\alpha + \mathbf{u}_\alpha \cdot \underline{\Pi}_\alpha + \mathbf{h}_\alpha \right] = q_\alpha n_\alpha \mathbf{u}_\alpha \cdot \mathbf{E} + \mathcal{C}_\alpha^{[2]} + \mathcal{S}_\alpha^{[2]}, \tag{212}$$

where

$$\mathcal{C}_\alpha^{[2]} \stackrel{\mathrm{def}}{=} \sum_{k=0}^{z_\alpha} \mathcal{C}_{(\alpha,k)}^{[2]} \qquad \text{and} \qquad \mathcal{S}_\alpha^{[2]} \stackrel{\mathrm{def}}{=} \sum_{k=0}^{z_\alpha} \mathcal{S}_{(\alpha,k)}^{[2]}. \tag{213}$$

Summing the contributions for each ionization state, whilst noting that the terms due to charge-exchange interactions cancel, the averaged collision source reduces to

$$\mathcal{C}_\alpha^{[2]} = \frac{1}{2} m_e \mathbf{u}_e^2 \Gamma_\alpha^{\mathrm{rec}} + \sum_{s \in \Lambda_{\mathrm{FA}} \backsim \alpha} \left(\mathbf{u}_\alpha \cdot \mathbf{R}_{\alpha;s} + Q_{\alpha;s} \right), \tag{214}$$

where $\Gamma_\alpha^{\mathrm{rec}}$, $\mathbf{R}_{\alpha;e}$, and $\mathbf{R}_{\alpha;\beta}$ are given in (209), and $Q_{\alpha;e}$, $Q_{\alpha;\beta}$ are defined in a similar manner; ie.,

$$Q_{\alpha;e} \stackrel{\mathrm{def}}{=} \sum_{k=0}^{z_\alpha} Q_{(\alpha,k);e}, \qquad Q_{\alpha;\beta} \stackrel{\mathrm{def}}{=} \sum_{k=0}^{z_\alpha} \sum_{\ell=0}^{z_\beta} Q_{(\alpha,k);(\beta,\ell)}, \qquad (\beta \neq \alpha). \tag{215}$$

For the electron collision source, we employ the following approximation:

$$\begin{aligned} \mathcal{C}_e^{[2]} \stackrel{\mathrm{def}}{=} & \sum_{\alpha=1}^{N_A} \frac{m_e}{m_\alpha} \left(\frac{1}{2} m_\alpha \mathbf{u}_\alpha^2 + \rho_\alpha e_\alpha \right) \Gamma_\alpha^{\mathrm{ion}} - \sum_{\alpha=1}^{N_A} \sum_{k=0}^{z_\alpha - 1} \phi_{(\alpha,k)}^{\mathrm{eff}} \Gamma_{(\alpha,k)}^{\mathrm{ion}} - \frac{1}{2} m_e \mathbf{u}_e^2 \sum_{\alpha=1}^{N_A} \Gamma_\alpha^{\mathrm{rec}} \\ & + \sum_{\alpha=1}^{N_A} \left(\mathbf{u}_e \cdot \mathbf{R}_{e;\alpha} + Q_{e;\alpha} \right) + Q_e^{\mathrm{rad}}, \end{aligned} \tag{216}$$

where

$$Q_{e;\alpha} \stackrel{\mathrm{def}}{=} \sum_{k=0}^{z_\alpha} Q_{e;(\alpha,k)}, \tag{217}$$

and $\Gamma_\alpha^{\mathrm{ion}}$, $\Gamma_\alpha^{\mathrm{rec}}$, and $\mathbf{R}_{e;\alpha}$ are given in (209) and (211).

APPENDIX C. BRIEF DESCRIPTION OF BRAGINSKII MODEL

The theoretical development of anisotropic transport and transport coefficients for plasmas can be found in [24, 59]. Anisotropic transport is due to the effects of strong magnetic fields. For the case of heat flux, the heat flux vector is dependent on magnetic field direction. In ionized plasmas, the heat flux characterized by drift and thermal components

$$\begin{aligned}
\mathbf{h}_e &= \mathbf{h}_e^u + \mathbf{h}_e^T \\
\mathbf{h}_e &\approx \mathbf{h}_e^T \\
\mathbf{h}_e &= -\kappa_\parallel^e \nabla_\parallel T_e - \kappa_\perp^e \nabla_\perp T_e + \kappa_\wedge^e \hat{\mathbf{b}} \times \nabla_\perp T_e.
\end{aligned}$$

where $\mathbf{h}_e^u$ and $\mathbf{h}_e^T$ are drift and thermal components and the subscript/superscript (e,i) depict electrons or ions. Braginskii [24] derived thermal conductivity coefficients for fully ionized plasmas

$$\begin{aligned}
\kappa_\parallel^e &= 5.763 \times 10^{-21} \frac{T_e^{5/2}}{\lambda} \\
\kappa_\perp^e &= 1.4747 \frac{\kappa_\parallel^e}{(\omega_e \tau_e)^2} \sim \kappa_\parallel^e / ||\mathbf{B}||^2 \\
\kappa_\wedge^e &= 0.7911 \frac{\kappa_\parallel^e}{(\omega_e \tau_e)} \sim \kappa_\parallel^e / ||\mathbf{B}||.
\end{aligned}$$

We are mainly interested in the thermal components within the context of MHD modeling. From scaling arguments, it can be shown that the thermal conductivity coefficient for electrons dominates over ions

$$\kappa_\parallel^e / \kappa_\parallel^i \approx 49.$$

Note that the heat flux vector representing the thermal component $\mathbf{h}_e \approx \mathbf{h}_e^T$ is a kinematic relationship dependent the magnetic field vector

$$\begin{aligned}
\hat{\mathbf{b}} &= \mathbf{B}/||\mathbf{B}|| \\
\nabla_\parallel T &= \left(\nabla T \cdot \hat{\mathbf{b}}\right) \hat{\mathbf{b}} \\
\nabla_\perp T &= \nabla T - \nabla_\parallel T
\end{aligned}$$

therefore we arrive at a model for anisotropic heat transport appropriate for MHD,

$$\mathbf{h} = -\kappa_\parallel \nabla_\parallel T - \kappa_\perp \nabla_\perp T + \kappa_\wedge \hat{\mathbf{b}} \times \nabla_\perp T. \tag{218}$$

We tested the anisotropic formulation (218) on a relatively straightforward test problem. A square computational domain 4×4 was constructed using element counts: 64×64, 128×128, 256×256 and 512×512. A temperature "ring" was placed inside the square with a clipped Gaussian cross section which has a known integrated thermal energy (in this case $Cv < T >$ where <> represents the average). The integrated thermal energy for this Gaussian shaped ring was 19.97300199. The density was constant $\rho = 1$ and so was the specific heat $Cv = 2.0$. A constant background azimuthal magnetic field $||\mathbf{B}|| = 1$ that decays as $1/r$ was superimposed on the mesh. Parallel thermal conductivity $\kappa_\parallel = 1$, perpendicular $\kappa_\perp = 0$ and rotational $\kappa_\wedge = 0$ were held constant. The solution of this diffusion problem for temperature for all time is constant equal to the initial condition. Continuous Galerkin (CG) and algebraic flux correction (AFC) finite element formulations were run for a time $t = [0, 1]$.

The evolution of the temperature in time with mesh refinement for CG and AFC are shown in Figure C-1. The oscillatory nature of the CG solutions is evident in the overshoot of temperature. The AFC appears to be converging to the correct solution.

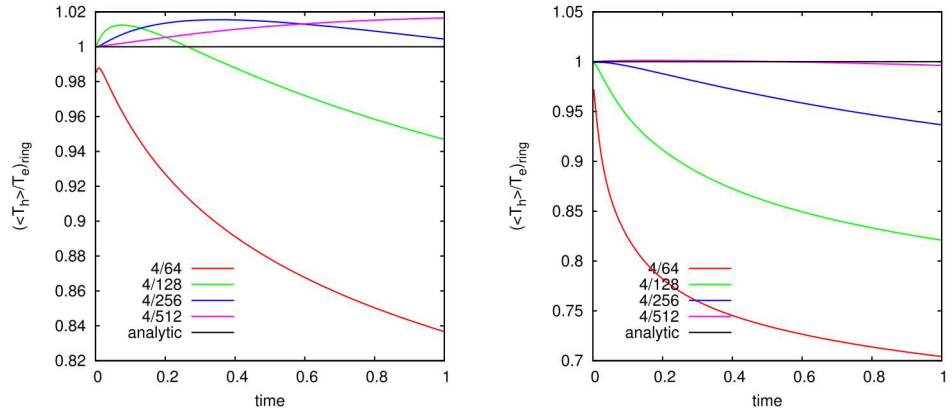

(a) CG **(b)** AFC

Figure C-1. Evolution of error of temperature ring profiles with anisotropic diffusion.

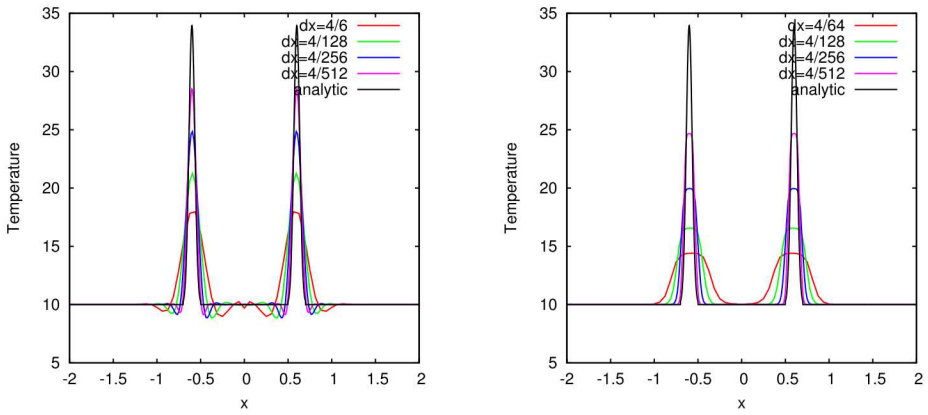

(a) CG **(b)** AFC

Figure C-2. Temperature Ring profiles with anisotropic diffusion.

Cross-cut profiles for grid refinement levels for CG and AFC at $t = 1$ are shown in Figure C-2. The CG solutions for temperature are oscillatory due to the lack of any stabilization while the AFC solutions are non-oscillatory though more diffused in the radial direction. The AFC does apply stabilization to diffusion fluxes.

Finally, the error is computed for each refinement level and plotted in Figure C-3. At these mesh levels, and due to the oscillatory behavior, the CG is not convering monotonically while the AFC is.

We expect the results of applying the AFC stabilization for the very strongly anisotropic conduction heat transfer for magnetized plasmas to improve with our current development of a smoothness indicator that will be used to turn off the LED stabilization at smooth local extrema. Additionally we have demonstrated the development of high-order methods based on Bernstein polynomial FE methods that will also improve the convergence of the AFC method for these challenging problems.

Braginskii [24] also formulated a model anisotropic viscous stress tensor which is summarized in [59]. Let η^i, η^e represent viscosity coefficients for ions and electrons repectively. Unlike thermal flux in the case of viscosity, the ion viscosity dominates,

$$\eta_0^i / \eta_0^e \approx 39.$$

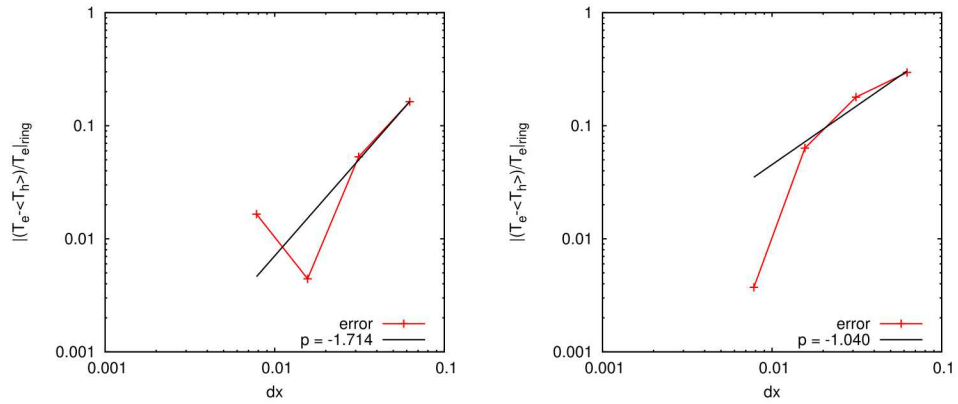

(a) CG **(b)** AFC

Figure C-3. Error in the temperature ring with anisotropic diffusion.

Branginskii derived ion viscosity coefficients for fully developed plasmas

$$\begin{aligned}
\eta_0^i &= 3.5\times 10^{-27}\frac{T_i^{5/2}\sqrt{\tilde{m}_i}}{\lambda} \quad \text{(parallel)}\\
\eta_1^i &= 0.3125\frac{\eta_0^i}{(\omega_i\tau_i)^2} \sim \eta_0^i/||\mathbf{B}||^2 \quad \text{(perpendicular)}\\
\eta_2^i &= 4\eta_1^i\\
\eta_3^i &= 0.5208\frac{\eta_0^i}{(\omega_i\tau_i)} \sim \eta_0^i/||\mathbf{B}|| \quad \text{(gyration,drift)}\\
\eta_4^i &= 2\eta_3^i.
\end{aligned}$$

The kinematic relationships taken from [59] are

$$W_{ij} = \frac{\partial u_i}{\partial x_j} + \frac{\partial u_j}{\partial x_i} - \frac{2}{3}\delta_{ij}\frac{\partial u_k}{\partial x_k}. \tag{219}$$

In the absence of a magnetic field, this is particularly simple,

$$\Pi_{ij} = -\eta_0 W_{ij}, \tag{220}$$

but in a strong magnetic field ($\omega_c\tau \gg 1$), the stress tensor becomes aligned with $\hat{\mathbf{b}}$. In the coordinate system with the third axis parallel to the magnetic field, the components of the stress tensor are:

$$\begin{aligned}
\Pi_{11} &= -\frac{1}{2}\eta_0(W_{11}+W_{22}) - \frac{1}{2}\eta_1(W_{11}-W_{22}) - \eta_3 W_{12},\\
\Pi_{12} &= -\eta_1 W_{12} + \frac{1}{2}\eta_3(W_{11}-W_{22}) = \Pi_{21},\\
\Pi_{13} &= -\eta_2 W_{13} - \eta_4 W_{23} = \Pi_{31},\\
\Pi_{22} &= -\frac{1}{2}\eta_0(W_{11}+W_{22}) - \frac{1}{2}\eta_1(W_{22}-W_{11}) + \eta_3 W_{12},\\
\Pi_{23} &= -\eta_2 W_{23} + \eta_4 W_{13} = \Pi_{32},\\
\Pi_{33} &= -\eta_0 W_{33}.
\end{aligned} \tag{221}$$

This model has been implemented in Drekar, however at present has not been fully tested.

APPENDIX D. STRONG STABILITY PRESERVING EMBEDDED RUNGE-KUTTA PAIRS

Any time integration method with a constant step size will perform poorly if the solution varies rapidly in some parts of the integration interval and slowly in other, large parts of the integration interval, and if it is to be resolved well everywhere by the numerical method [8]. A critical component of many integration packages utilizing Runge–Kutta methods, making them an initial value problem (IVP) "solver" rather than just a numerical integration subroutine, is its adaptive control of step-size based on local truncation error estimation.

The embedded methods are designed to produce an estimate of the local truncation error of a single Runge-Kutta step, and as result, allow to control the error with adaptive step-size. The key idea of embedded methods is that such a pair of methods will share stage computations. The two methods combines the stage solutions differently, i.e $b \neq \tilde{b}$ of varying order. Therefore, let us assume that the vectors b and $\tilde{b}$ correspond to order p and $\tilde{p}$, respectively. In general the assumption is $\tilde{p} \leq p$.

$$\tilde{y}_{n+1} = y_n + \Delta t \sum_{i=1}^{s} \tilde{b}_i F_i \tag{222}$$

where the F_i, the internal stage computations, are the same for the higher order method.

The Runge-Kutta formula of higher order p yields numerical approximation u_{n+1}, just as before, is used to advance in time. The solution $\tilde{y}_{n+1}$ is only used for error estimation and suggesting an optimal step-size. An Embedded Runge-Kutta (ERK) method is represented with an extended Butcher Tableau of $RK(A, b, \tilde{b})$:

Embedded Runge–Kutta methods are crucial for automatic step size control, i.e. the method automatically chooses the step size in each step. Let us consider the numerical solutions y_{n+1} and $\tilde{y}_{n+1}$ with order p and $\tilde{p} = p - 1$, respectively. Taking into account Runge–Kutta methods and their embedded pairs we have an approximation for the global error vector which is denoted by $\tilde{e}_{n+1}$. It can be calculated as

$$\tilde{e}_{n+1} = y_{n+1} - \tilde{y}_{n+1} = \Delta t \sum_{j=1}^{s} \left(b_j - \tilde{b}_j\right) F(y_j).$$

The above formula shows that the Butcher form is efficient from the programming point of view.

Since we strive to keep the entire integration process local in time (i.e., we march in time with all the information locally known) we attempt to control the local error or the local truncation error, rather than the global error. The global error also relates to the tolerance in case it can be obtained as a simple sum of local errors. Basically, by specifying an error tolerance ETOL a user can require a more accurate (and more expensive) approximate solution or a less accurate (and cheaper) one.

The global error of the order $p-1$ method can be approximated by the term $M(\Delta t)^p$, where M is an appropriate constant. On the other hand, from the local truncation errors we can conclude that $|\tilde{e}_{n+1}| \approx M(\Delta t)^p$. Therefore, if the relation $|\tilde{e}_{n+1}| < \varepsilon$ holds in case of a given tolerance $\varepsilon > 0$, then we accept the numerical solution y_{n+1}. Otherwise, we have to choose a new step size Δt_{new}. In this case we have the relation $\tilde{e}_{n+1} \approx M(\Delta t_{\text{new}})^p < \varepsilon$. Since $|\tilde{e}_{n+1}| \approx M(\Delta t)^p$, it implies that

$$\frac{M(\Delta t_{\text{new}})^p}{M(\Delta t)^p} < \frac{\varepsilon}{\tilde{e}_{n+1}}.$$

Hence, it requires the condition

$$\Delta t_{\text{new}} := \Delta t \left(\frac{\varepsilon}{\tilde{e}_{n+1}}\right)^{\frac{1}{p}}.$$

In [32] we constructed several non-defective methods with large region of absolute stability and optimal error measurement. The new family of embedded pairs offer the ability for strong stability preserving (SSP) methods to adapt by varying the step-size based on the local error estimation while maintaining their inherent nonlinear stability properties. In this work we are interested in embedded pairs for the optimal strong stability preserving (SSP) explicit Runge–Kutta methods. SSP explicit RK methods are extensively used in numerical computation of hyperbolic conservation with total variable diminishing (TVD) spatial discretization. In many hyperbolic PDE applications, the step-size is controlled by monitoring the CFL number, defined by

$$\nu = \frac{c_{\max}\Delta t}{\Delta x}$$

where $c_{\max}$ is the largest wave speed present. Since the Lipschitz constant of the spatial discretization is typically proportional to $c_{\max}/\Delta x$, most schemes are stable up to a particular value of ν. Inherent in this approach to step-size control, is the assumption that one can integrate or time-step at or near the largest (linearly- or nonlinearly-) stable step-size and still achieve an acceptable level of temporal error. This is reinforced by experience showing that spatial error usually dominates temporal error in such problems [99]. However making this assumption and relying on this experience is not enough; an approach that attempts to estimate and control error while adaptively selecting time-steps is important to achieve accurate and inexpensive solutions. Additionally when solving nonlinear PDEs in multiple dimensions, the error estimation provided by embedded RK pairs is essentially free compared to the expensive evaluation of the right-hand-side.

DISTRIBUTION

Hardcopy—Internal

Number of Copies	Name	Org.	Mailstop
1	D. Chavez, LDRD Office	1911	0359

Email—Internal

Name	Org.	Sandia Email Address
Technical Library	01177	libref@sandia.gov

Sandia National Laboratories is a multimission laboratory managed and operated by National Technology & Engineering Solutions of Sandia LLC, a wholly owned subsidiary of Honeywell International Inc., for the U.S. Department of Energy's National Nuclear Security Administration under contract DE-NA0003525.